

VALIDATION OF CFD FOR MODELING ATRIA

VALIDATION OF
COMPUTATIONAL FLUID DYNAMICS
FOR ATRIA GEOMETRIES

By

CHARLES RUNDLE, B.Eng.Society

A Thesis

Submitted to the School of Graduate Studies

In Partial Fulfillment of the Requirements

For the Degree

Masters of Applied Sciences

McMaster University

© Copyright by Charles Rundle, Sept 2009

MASTER OF APPLIED SCIENCES
(Mechanical Engineering)

McMaster University
Hamilton, Ontario

TITLE: Validation of Computational Fluid Dynamics for Atria Geometries

AUTHOR: Charles Rundle, B.Eng.Society. (McMaster University)

SUPERVISOR: Professor M.F. Lightstone

Number of Pages: xiii, 196

Abstract

A systematic validation of the computational fluid dynamics code ANSYS CFX for atria geometries is presented. Turbulent natural convection, radiation heat transfer and conjugate heat transfer are essential to the performance of an atrium and are all validated separately. In order to be thorough, the initial validations involve the fundamental simulations for each phenomenon. A simulation of a complete atrium is also presented using the conclusions reached in the previous validations.

The validation of each of the phenomena was successful. Turbulent natural convection simulations yielded two suitable turbulence models, with the preference for $k-\omega$ model being decided by a narrow margin. The radiation validations proved that the Discrete Transfer model was an accurate model and the best offered by ANSYS CFX. Conjugate heat transfer showed that ANSYS CFX was capable of capturing the qualitative aspects of the phenomenon. The final atrium simulations showed the expected over prediction of temperature in the atrium, and an under prediction of the stratification. The atrium simulation proved insensitive to façade emissivity. The magnitude of the solar radiation heat flux did change the temperature and velocity field. It was shown that ANSYS CFX was capable of modeling the important phenomena but more accurate boundary conditions are required to obtain the best results possible.

Acknowledgments

I would like to thank Dr. Lightstone for her assistance during the completion of this work. Her support and aid have been invaluable to me. I have learned a great deal from her and consider myself lucky to have had her as a supervisor.

In addition I thank Cathy Strutt, Deep Home, Salam Ali and everyone else in JHE 215. They were an excellent source of motivation and help.

Thanks are more than due to Dr. Athienitis, Dr. Karava and Eleni Mouriki from Concordia University for the use of the data they gathered from their atrium, which was essential for this research and generally allowing me to ask questions and answering them. Without their help this thesis would not have been possible.

I would also like to thank the Solar Buildings Research Network for their financial support.

I would also like to thank J. Rundle for her irreplaceable help in editing this thesis.

I would like to dedicate this work to my family and Erin.

Table of Contents

Abstract	iii
Acknowledgments	iv
List of Figures	vii
Nomenclature	xi
1 Introduction	1
1.1 Background.....	1
1.2 Objectives and Strategy.....	2
1.3 Thesis Outline.....	3
2 Literature Review	4
2.1 Impact of Atria.....	4
2.2 Physical Phenomena.....	5
2.3 Goals of Design	6
2.4 Simulation Tools	9
2.5 Previous Modeling Work	12
2.6 Summary	16
3 Natural Convection Validation	17
3.1 Background.....	17
3.1.1 Natural Convection in Atria.....	17
3.1.2 Definitions	18
3.1.3 Models & Theory	19
3.2 Simulations	28
3.2.1 Laminar Natural Convection in a Square Cavity	28
3.2.2 Turbulent Natural Convection in a Square Cavity	37
3.3 Conclusion.....	57
4 Radiation Heat Transfer Validation	58
4.1 Background	58
4.1.1 Radiation in Atria	58
4.1.2 Definitions	59
4.1.3 Models & Theory	59
4.2 Simulations	63
4.2.1 Specified Heat Flux Simulations	63
4.2.2 Specified Temperature Simulations	71
4.2.3 Solar Radiation Simulations	78
4.3 Conclusions	84

5	Conjugate Heat Transfer Validation	86
5.1	Background	86
5.1.1	Conjugate Heat Transfer in Atria	86
5.1.2	Definitions.....	87
5.1.3	Models & Theory	88
5.2	Simulations.....	90
5.2.1	Horizontal Channel with Aluminium Heated Section	90
5.2.2	End Condition Variation	102
5.2.3	Ambient Temperature Variations	105
5.3	Conclusion.....	107
6	Atrium Validation Simulations	108
6.1	Background	108
6.1.1	Interaction of Phenomena	108
6.1.2	Definitions	109
6.1.3	Models & Theory	110
6.2	Simulations	112
6.2.1	Concordia Atrium Simulation	112
6.2.2	Façade Emissivities Simulations	134
6.2.3	Solar Radiation Flux Simulations	138
6.3	Conclusion	144
7	Summary	146
7.1	Summary and Conclusion	146
7.2	Recommendation for Future Work	148
	References	150
A	Two Dimensional Domains in ANSYS CFX	154
B	Extrapolation Equations	156
C	Conservative and Hybrid Variables	159
D	Radiation Heat Flux Boundary Condition	161
E	Solar Opening Analytical Model	164
F	Logical Function Using CEL Code	173
G	Solar Position Angles	189
H	Opening Back Entrance (OBE)	193

Table of Figures

1.1	Common Atria Geometries	1
3.1	Sample Domain for the Laminar Natural Convection Simulations	30
3.2	Temperature Distributions in Cavity for Different Rayleigh Numbers	32
3.3	Average Nusselt Number for Square Cavity with Rayleigh Number 10^4 vs. the Number of Nodes in Each Direction	33
3.4	Average Nusselt Number for Square Cavity with Rayleigh Number 10^5 vs. the Number of Nodes in Each Direction	34
3.5	Average Nusselt Number for Square Cavity with Rayleigh Number 10^6 vs. the Number of Nodes in Each Direction	34
3.6	Layout of Cavity Used in Experimental Work	38
3.7	Turbulent Natural Convection Domain with Centerline Indicated	40
3.8	80x80 Expanding Mesh Used as Standard Mesh for Turbulent Natural Convection Simulations	41
3.9	Velocity v Component for A) k- ϵ Model, B) k- ω Model C) SST Model and Experimental Data	42
3.10	Temperature Profiles for A) k- ϵ Model, B) k- ω Model C) SST Model and Experimental Data	44
3.11	The Effect of the Relaxation Number on Otherwise Identical Simulations ...	46
3.12	Velocity Profile in Boundary Layer Used to Show Grid Independent Results	47
3.13	Temperature Profile in Boundary Layer Used to Show Grid Independent Results	48
3.14	Velocity Profile in Boundary Layer by Hot Wall for Standard Models	49
3.15	Velocity Profile in Boundary Layer for k- ϵ Model with Varying Levels of Buoyancy Turbulence Production	51
3.16	Velocity Profile in Boundary Layer for k- ω Model with Varying Levels of Buoyancy Turbulence Production	52
3.17	Velocity Profile in Boundary Layer for SST Model with Varying Levels of Buoyancy Turbulence Production	53
3.18	Isothermal Images of SST Models with Varying Levels of Buoyancy Turbulence Production	55
3.19	Eddy Viscosity in Domain of SST Simulations	56

4.1	Discrete Transfer Rays	61
4.2	Monte Carlo Photon Paths	63
4.3	Domain for Specified Heat Flux Simulations	65
4.4	Average Conservative Temperatures for Different Radiation Models with a Specified Heat Flux Boundary Condition	66
4.5	Average Hybrid Temperatures for Different Radiation Models with a Specified Heat Flux Boundary Condition	67
4.6	Temperature Distribution Comparison between Hybrid and Conservative Values	68
4.7	Temperature Distribution of Hot Wall Boundary for Different Mesh Refinements	69
4.8	Temperature Distribution along Hot Wall of Monte Carlo Model	70
4.9	Percentage Error Based on Nodes per Side of Mesh	75
4.10	Heat Flux along the Centerline for Discrete Transfer Radiation Model Simulation with 50 K Temperature Difference with Uniform Meshes	76
4.11	Domain for Solar Radiation Simulation	79
4.12	Temperature Difference along Wall after Sixty Two Iterations	83
5.1	Area to be Modelled Using Thermal Resistance	89
5.2	Horizontal Channel Domain	91
5.3	Domain and Boundry Conditions	92
5.4	Meshing Areas of the Horizontal Channel	93
5.5	Temperature Profiles for Standard Simulation at; A) $y/H=0$, B) $y/H=0.5$, C) $y/H=0.875$	96
5.6	Temperature Profiles for Grid Independent Simulation at; A) $y/H=0$, B) $y/H=0.5$, C) $y/H=0.875$	98
5.7	Recirculating Flow at Channel Exit	99
5.8	Temperature Difference between $y/H=0.5$ and $y/H=0$	100
5.9	Temperature Difference between $y/H=0.875$ and $y/H=0$	101
5.10	Temperature Profiles for Extended Simulation at; A) $y/H=0$, C) $y/H=0.5$, C) $y/H=0.875$	103
5.11	Extended and Standard Simulation for Entire Channel Length	104
5.12	Temperatures for Ambient Temperature Simulations at; A) $y/H=0$, B) $y/H=0.5$, C) $y/H=0.875$	106

6.1a	Concordia's Atrium	108
6.1	Control Volume for Solar Heat Flux Magnitude Calculations	110
6.2	Surfaces and Diagrams for Calculation of Solar Radiation Magnitude	111
6.3	Atrium Domain and Orientation	114
6.4	Atrium Dimension and Sub Domains	115
6.5	Façade Specified Temperature Boundary Condition	117
6.6	Isometric View of Mesh	119
6.7	Mesh in the y Direction	120
6.8	Temperatures along Three Planes in Atrium	122
6.9	Floor Temperature for Solar Simulation	123
6.10	Temperature at Thermocouple Strings; A) East String, B) Center String, C) West String	124
6.11	Comparison of Temperature Difference	125
6.12	Velocity Vector Plots for Solar Simulation	126
6.13	Heat Flow at Each Boundary of the Standard Solar Simulation	127
6.14	Temperature at Thermocouples for Varying Levels of Mesh Refinement ...	128
6.15	Temperature Profiles for Varying Mesh Refinement	129
6.16	Temperature Profile in Atrium; A) XY plane, B) XZ plane	131
6.17	Velocity and Temperature Field Comparison; A) Velocity, B) Temperature	132
6.18	Temperature at Thermocouple Strings for Varying Façade Emissivities; A) East String, B) Center String, C) West String	135
6.19	ΔT for Varying Façade Emissivities	136
6.20	Center String Temperature vs. Façade Emissivity	137
6.21	Temperature at Thermocouple Strings for Varying Solar Radiation Magnitude; A) East String, B) Center String, C) West String	139
6.22	ΔT along Each Thermocouple String for Varying Solar Radiation Magnitudes	140
6.23	Temperature along Central String vs. SI	141
6.24	Heat Flow at Each Boundary of Simulation with 25% SI.....	142
6.25	Results for Different Solar Radiation Magnitudes for; A) Heat Flux, B) Temperature and C) Velocity	143

A.1	Actual Three Dimensional Domain Used in Two Dimensional Simulations and Cross Section of Nodes in z Direction Mesh	154
C.1	Finite Difference and Finite Volume Difference Nodes	159
C.2	Interpolation for Conservative Value	160
D.1	Heat Fluxes at Boundary Wall	162
E.1	Labeling Conventions for the Cube's Walls	165
E.2	Heat Fluxes for Surface i	166
E.3	Deviation as a Function of Angle	172
F.1	Step Function	174
F.2	Area Bounded by Trig Function	182
F.3	Trigonometric Heat Flux in a Box	183
F.4	Heat Flux along Line $y=2$	184
F.5	Area Bounded by Four Lines	185
F.6	Simulated Square Heat Flux Area.	187
F.7	Heat Flux along $y=0.75$	188
G.1	Earth's Codeclination	189
G.2	Colatitude Angle	190
G.3	Zenith Angle	191
H.1	Velocity in Atrium with an Opening on the North End	195
H.2	Temperature and Velocity Field for Atrium with Opening	196

Nomenclature

A	area
BI	radiation source for blinds
D'	co-declination
F	view factor
FI	floor solar heat flux
g	acceleration due to gravity
H	height
h	coefficient of heat transfer
I	radiation intensity
k	thermal conductivity, turbulent kinetic energy
L'	co-latitude
L	length
Q	heat flow
P_k	turbulence production
P_{kb}	buoyancy turbulence production
q	heat flux
R	thermal resistance
SI	solar radiation heat flux
T	temperature
ΔT	temperature stratification
t	time
U	mean velocity
u_τ	friction velocity
V	velocity
v	velocity component in y direction
x	horizontal direction
Δx	grid spacing
y	vertical direction (opposite of gravity acceleration)

y^+	dimensionless distance from wall
Z	Zenith

Greek Symbols

α	thermal diffusivity
β	thermal expansivity
ε	emissivity, turbulent dissipation
κ	von Karman constant
ρ	density, reflectivity
σ	Stefan-Boltzman constant
μ	dynamic viscosity
μ_T	turbulent viscosity
τ	shear stress
θ_s	solar elevation
ω	turbulent frequency
ν	kinematic viscosity

Subscript

amb	ambient value
c	cold value
conv	convection value
cool	cool wall value
h	hot value
hot	hot wall value
façade	façade value
ND	dimensionless value

new	value from this iteration
old	value from previous iteration
t	turbulent value
rad	radiation value
ref	reference value
solar	solar value
wall	wall value
∞	infinitely extreme value

Dimensionless Numbers

Pr	Prandtl number $Pr = \frac{C_p \mu}{k}$
Nu	average Nusselt number $\overline{Nu} = \frac{QL}{Ak(T_h - T_c)}$
T_{ND}	Non-dimensional temperature
Ra	Rayleigh number $Ra = \frac{g\beta(T_h - T_c)L^3}{\nu\alpha}$
v_{ND}	Dimensionless velocity vector $v_{ND} = \frac{v}{\sqrt{g\beta L(T_h - T_c)}}$
θ	Theta non dimensional temperature $\theta = \frac{T - T_{Amb}}{T_{Ref}}$

Chapter 1: Introduction

1.1 Background

Atria are an important design feature of many modern buildings. They have become increasingly popular features of new buildings. They consist of a large open space where at least one of the surrounding walls is made of transparent material that is usually glazed. This space is usually several stories high and located so that the transparent area is also an external façade of the building. There are many different atrium designs in use, however, only a few are commonly used [Ted Kesik, Personal Communication, Feb 28, 2006]. Figure 1.1 below shows the most common forms of atria.

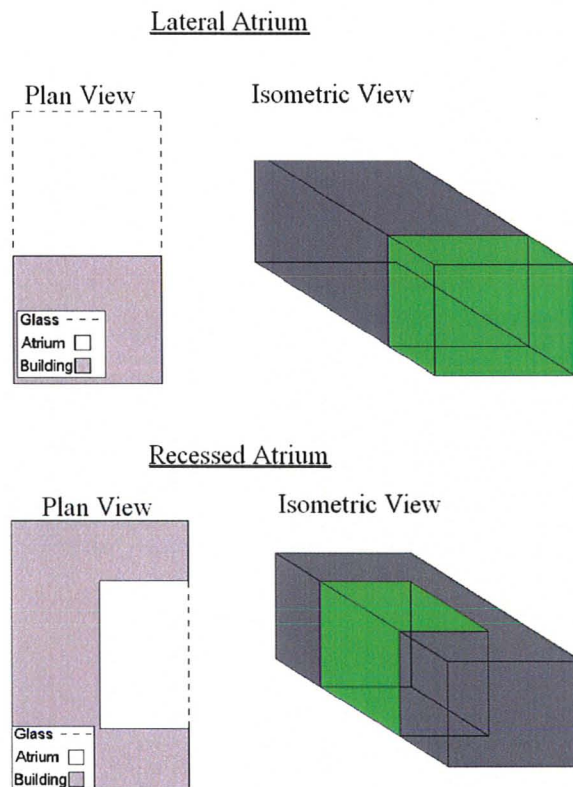


Figure 1.1 Common Atria Geometries

There are many reasons for including an atrium; the two most common are aesthetic value and environmental concerns. Atria offer the possibility of using passive solar energy to reduce the energy demands of a building and therefore, reduce its environmental impact. Buildings account for a significant amount of energy usage. For example, within the U.K. 43% of the total energy produced is used by non-industrial buildings, furthermore buildings are credited with being the source of one third of carbon dioxide on a global basis [Bowman et. al. 2000]. For these reasons, reducing the impact of buildings on the environment can have a significant effect. For an atrium to reduce energy usage it must be designed correctly. New tools are needed to improve the design process. An incorrectly designed atrium will increase the energy usage and due to the complex heat transfer and fluid flow that occurs in an atrium, traditional design software is ill suited to the task of modeling atria. Phenomena such as natural buoyancy induced ventilation, radiation heat transfer and conjugate heat transfer are some of the reasons for this. Computational fluid dynamics (CFD) offers great potential for modeling atria and allowing more accurate predictions of atria performance.

1.2 Objectives and Strategy

The objective of this thesis is to assess the suitability and accuracy of applying computational fluid dynamics to predict the fluid flow and heat transfer in atria geometries. This determination will be based on validation of the important phenomena in an atrium using fundamental simulations. The lessons learned from these essential validations will be use to run a full atrium simulation.

1.3 Thesis Outline

This thesis offers a systematic validation of ANSYS CFX for atria simulations. This includes turbulent natural convection, radiation heat transfer and conjugate heat transfer. These validation simulations will be used to determine the sensitivity of the models used by ANSYS CFX and develop recommendations for further use in modeling atria. In addition, validations will be performed using an actual atrium. This will be done to test the conclusions from the previous validations and determine sensitivities to input variables. This will provide a basis for suggesting further avenues of study and identifying which data must be considered in such a simulation.

Chapter 2: Literature Review

2.1 Impact of Atria

Atria are important to a building's function in three ways. They are often used as sources of natural ventilation, either acting as the sole source of ventilation or in tandem with a forced ventilation system. Because of their height, atria allow for temperature stratification of air and the formation of a pressure difference that makes the atrium act a natural chimney [Holford & Hunt, 2003]. If correctly used, natural ventilation can reduce the energy usage of a building. One common practice is to encourage natural ventilation at night to reduce the amount of energy stored in the building. This reduces and delays the temperature peak during the following day [Bressch, Dossaer & Janssens, 2005]. Pfafferott et. al. [2004] found that if only natural ventilation was used at night, a comfortable environment could still be maintained during the day, while significantly reducing the energy usage of the building. Breesch, Bossaer and Janssens [2005] found that using ventilation in the office building they studied allowed for peak temperatures to occur after business hours. However, if improperly designed, an atrium can prevent natural ventilation from occurring [Holford & Hunt, 2003].

Atria can act as a free source of natural daylight for a building. When the atrium's transparent wall acts as an external wall, sunlight can enter the atria and the connected building. The effect of this natural sunlight is twofold; the natural light can replace some electrical lights, reducing the energy consumption of the building and thus saving energy; and the presence of natural light can be more aesthetically pleasing [Galasiu and Atif, 2002].

Atria also have a significant impact on the thermal performance of the building [IEA, 1996]. The most common transparent external façade allows for significant amounts of heat transfer by radiation during a typical day [IEA, 1996]. The amount of heat loss or gain varies according to the external conditions; such as time of day and season.

These roles mean that the design of the atrium can have a significant effect on the usefulness of the building to which it is attached. The orientation, size, type of transparent façade and shape of the atrium all help determine how the atrium affects the building.

2.2 Physical Phenomena

There are a variety of physical phenomena that are critical to an atrium's performance that are not usually considered in building design. Each of these is the focus of validation studies to determine if ANSYS CFX has the capacity to accurately model them. These phenomena are natural convection, radiation heat transfer and conjugate heat transfer.

Natural Convection

Natural convection plays an important role in the heat and fluid flow in an atrium. Given the height of atria's facade, the buoyant air flow is usually turbulent. As an example, if an atrium was treated as a two dimensional square cavity the Rayleigh number would be calculated according to the following formula:

$$Ra = \frac{g\beta\Delta TH^3}{\nu\alpha} \quad (\text{Equation 1.1})$$

The typical values for the physical properties of air, a one degree temperature difference and a height and length of ten meters produces a Rayleigh number of order 10^{11} . This is well within the accepted values of turbulent Rayleigh numbers.

Radiation Heat Transfer

Radiation accounts for a larger amount of heat exchange in an atrium than in normal rooms. The large glazed façade allows for significant amounts of solar energy to enter the atrium. In addition, significant amounts of radiation can exit the atrium when the sun is not present. Wall [1997] found that traditional building models do not accurately account for radiation in a highly glazed area.

Conjugate Heat Transfer

Thermal mass, which allows for energy storage and release, is an important part of an atrium. Properly designed thermal mass will absorb excess energy during hot parts of the day and release the stored energy during the cooler parts of the day. Thus, the atrium will have a more even temperature over the day and minimal thermal extremes. Thermal mass often takes the form of solid objects and the heat transfer between the solid objects and the air must be modeled accurately.

2.3 Goals of Design

Several different criteria must be taken into consideration when designing an atrium. These typically include the aesthetic value of the atrium, energy usage and thermal comfort. As mentioned previously, there are several different possible reasons

for an atrium to be included in a building's design. The relative importance of these is dependent on the purpose of the atrium.

Aesthetic Appeal

Aesthetic appeal is the general appeal of the design. Atria have traditionally been included in buildings for this reason, however, since this goal is difficult to quantify it will not be given consideration in this thesis. It should be noted that there has been at least a single attempt to quantify the general attractiveness of an atrium's design. This was done with the Mass Rapid Transit (MRT) stations in Taiwan [Wang & Huang, 2004]. Survey techniques were used in conjunction with sketches of various proposed designs to determine which design should be used. One of the criteria considered was the appearance of the design.

Energy Usage

The energy usage of an atrium can vary significantly with the time of day and time of year. The HVAC system is one of the largest sources of energy use for an atrium [International Energy Agency, 1996]. Ideally the energy usage should be as low as possible. When properly designed, an atrium has the potential to lower the energy usage of a building [IEA, 1996]. Natural ventilation can supplement or replace mechanical ventilation and thermal mass can be used to store excess energy to reduce temperature swings and reduce the need for HVAC. Improperly designed atria can increase the energy usage of a building by overheating during the day and overcooling during the night. It has been shown that improperly designed atria can have the opposite effect of

natural ventilation and increase the requirements of the mechanical ventilation [Holford & Hunt, 2003].

Thermal Comfort

Thermal comfort is of importance when the atrium is meant to be occupied. Thermal comfort is determined by the temperature and velocity of the air and is related to the energy usage of an atrium. Ideally, the temperature of the atrium, without mechanical intervention, should be as close to the thermal comfort zone as possible. Federspiel (as cited in ASHRAE, 2005) found that 96.5% of complaints of discomfort occurred outside of the temperature range of 21-24°C. If the temperature leaves this range then the atrium may require increased energy usage to adjust the temperature of the air. The issue of thermal comfort is further complicated by stratification. The difference in temperature within the atrium can exceed the range of temperature in which a person will feel comfortable. This means that if the temperature along the bottom of the floor is comfortable the top floors connected to the atrium may be excessively hot. One solution to this is to extend the atrium past the top floors of the building or isolate it from the top floors. This allows the height required to drive the natural ventilation without the high temperatures affecting an occupied space. The velocity field also plays a role in making an atrium habitable. Berglund, and Fobelets (as cited in ASHRAE, 2005) found that a velocity less than 0.25 m/s is desired.

2.4 Simulation Tools

There are several different tools to model both atria and buildings; energy calculations, building energy simulations (BES) and computational fluid dynamics (CFD). Each tool offers its own advantages and drawbacks.

Integral Energy Calculations

Energy calculations are perhaps the simplest tool available. They use empirical correlations to predict energy usage and general temperature in a room [IEA, 1996]. This type of model uses gross characteristics of a room such as orientation, window size and window type to determine approximate values for temperature and energy usage. This offers a quick method to compare gross differences in design. The results are not necessarily accurate but provide a good comparison between different designs. Typically the empirical equations do not take into consideration some important features of atria. Stratification is one such aspect that is ignored by the general assumption of a uniform temperature. However, there has been some work to create empirical models that do take stratification into account. Work done in Sweden has shown promise using empirical models to predict stratification so that it is included in the results [IEA, 1996].

Building Energy Simulations (BES)

Building energy simulations are popular methods for building simulations. Three such programs are EnergyPlus, TRNSYS15 and ESP-r, which have been generally shown to be versatile and reliable [Ibanez et. al., 2005]. Typically they use zones which are

treated as well mixed. They may have multiple zones; the TRNSYS15 component Type 56 'Multi-Zone Building' allows for up to 25 zones, each with a single node [Ibanez et. al., 2005]. They differ from energy calculations in that they are more complex and allow interaction between different zones and more complicated interaction with other components such as HVAC systems. BES rarely solve for the fluid flow within a building directly. Typically, the flow is determined by either experimental measurement or by using an additional program to generate estimates of flow between zones. The additional program may be a CFD code [IEA, 1996] or a simpler program, such as COMIS that uses pressure difference to calculate flow rates [Breesch, Bossaer & Janssens, 2005]. The detailed fields are not solved within each zone. Each zone is assumed to be well mixed and have a uniform temperature, if radiation is being considered an additional temperature which accounts for wall temperature is also considered [Breesch, Bossaer & Janssens, 2005]. The use of the well mixed assumption has been associated with the inability to model stratification similar to the limitation of integral energy calculations. A recent approach has been to use multiple zones located above each other [IEA, 1996]. This allows for the temperature difference between each zone to model the stratification and has had some success [IEA, 1996]. BES also requires complex empirical models, which may have to be custom fitted to each surface. Coefficients of heat transfer for walls are one such type to be considered. Veoltzel et. al. [2001] found that a specialized process had to be used to determine the coefficient of heat transfer for the wall. In addition, Gao, Zhang and Zhao [2008] found that standard empirical models for coefficients of heat transfer were not accurate for surfaces adjacent

to stratified air. They showed that CFD had the capacity to produce much more accurate predictions of heat transfer coefficients than any empirical model they used.

Wall [1997] found that BES models were unsuccessful in dealing with solar radiation. They were often limited to black surfaces. In addition solar radiation input was treated as diffuse. These two factors lead to over predicting the energy gain from solar radiation. TRNSYS divides solar energy into three categories; lost, to air and to surface [IEA, 1996]. The lost portion is a percentage that is considered lost out the room's windows. The 'to air' portion is usually between 10% and 30% and is transferred directly to the air. The remaining portion of solar energy heats the surface. Therefore, TRNSYS is capable of modeling this phenomena but it requires user input to predict the correct portions [IEA, 1996]. The largest concern is the lack of detailed data within each zone, especially the velocity.

Computational Fluid Dynamics (CFD)

Computational fluid dynamics (CFD) solves the governing equation of heat and fluid over a discretized domain. CFD provides a much more detailed solution, including both temperature and velocity fields, however, it is much more computationally expensive. CFD has been used in several ways in modeling atrium. In common usage, CFD is used to calculate velocity fields, either to create input data for the zones in a BES or to calculate the velocity field in a specific area of concern. There is significant potential for CFD to expand its role [IEA, 1996]. A simulation which includes the entire domain offers a much more complete analysis of the atrium but at the cost of computational effort. Also there is a lack of data regarding CFD for full simulations.

Current Methods

The most complete method of modeling atria uses a variety of design tools [IEA, 1996]. As the design is refined from the general concept, different tools are used to allow for more accurate predictions. The general course of work starts with gross details such as orientation and façade type combined with energy calculations. BES models are used to fit additional systems, such as HVAC and multiple zones to create more detailed and accurate temperature estimates. At this stage CFD may be used to estimate the velocity field in the atrium to determine the fluid flow between zones. This is typically done with an isothermal model and no buoyancy since only general mass flow rates are required, not detailed information. Finally, if there is an area where the velocity may be too high for comfort then a detailed CFD simulation of that area is done to determine if minor changes, such as wind guards need to be added.

2.5 Previous Modeling Work

Building Energy Simulation Modeling

Laouadi & Atif [1999] and Voeltzel et. al. [2001] were very successful in predicting the temperature distribution. Their simulation using ESP-r was capable of predicting stratification in a real atrium and had good agreement in general with measured temperatures. However, as mentioned previously the BES program was incapable of modeling the airflow in the atrium. Each group of authors used a difference method to account of air flow. Laouadi & Atif [1999] used measured airflow from a previous experiment in the atrium. This is limiting because it requires an actual atrium to perform measurements in and is only accurate for the conditions under which the

measurements are taken. Voeltzel et. al. [2001] created a program named AIRGLAZE, which solves the mass equation, enthalpy equation and the perfect gas law equation but not the momentum equation. They also modified the method of calculating the heat transfer coefficients for each different atrium, meaning that the program would require specialised adaptation to each case [Voeltzel et. al., 2001]. To work, the programs required specific conditions such as isothermal walls which may not be practical in a real building [Voeltzel et al., 2001]. The improvement this program represents treats the air in the atria as separate zones rather than a homogenous mixture and accommodates long wave radiation between objects [Voeltzel et. al. 2001]. Breesch, Bossaer and Janssens [2005] used TRNSYS coupled with COMIS, a program to predict airflow, to model night natural ventilation in a low energy office building. They produced good average results for the temperature peaks in the office building but did not predict the stratification that occurred.

Computational Fluid Dynamics Modeling

From a computational fluid dynamics perspective these issues can be handled in several ways. Gan & Riffat [2004] used FLUENT to model the effects of an opening's location on stratification and natural ventilation, however, there was no comparison to experimental data. Ozeki, Kato & Murakami [1996] modeled several atria using a low Re k - ϵ turbulence model. Their predictions were accurate with steady state simulations but no stratification was shown. This contradicts the findings by IEA [1996] that transient solutions improve accuracy and can result in significantly different results. IEA [1996]

showed that the use of transient simulations can change the average atrium temperature by four degrees.

Combination Modeling

An increasing popular method is to connect a CFD simulation with a BES simulation. The BES simulation is run to determine the boundary conditions of the CFD simulation and where the detail of CFD is not required. Then the CFD simulation provides important inputs to the BES simulation, such as air flow and heat transfer coefficients. Tan & Glicksman [2005] used a program called MMPN which combines a multi-zone BES and CFD model using with a RNG k-epsilon model. The atrium was divided into zones for the BES then CFD calculations were run within those zones of interest. Pappas and Zhai [2008] used a combination of BES and CFD to model a double skin façade. While this is not strictly an atrium, a double facade possesses many of the same characteristics. EnergyPlus, which was the BES, calculated the wall temperatures and the effects of shading devices. The CFD software then used this information to calculate the temperature stratification, air flow and coefficient of heat transfer. These were then used by EnergyPlus to solve for the previously mentioned variables. This allowed for more accurate boundary conditions for the CFD simulation.

Size of Validation Atrium

Many CFD simulations have been validated against data from scaled down atria. This was done in the case of Ozeki, Kato & Murakami [1996]. This is also common in BES work. The experimental data used for Voeltzel et. al. [2001] was collected from model atria only 5 meters in height. This was likely the reason that some of the atria did

not show stratification [Voeltzel et. al., 2001]. This practice poses several problems because the scale of the atria may not be sufficient for stratification to occur for sufficiently turbulent flow to develop. Work has been done on full size atria. For example, Breesch, Bossaer and Janssens [2005] used a full scale building to compare with their BES simulations.

Expanding the Role of Computational Fluid Dynamics

As mentioned CFD already plays a role in building simulations. However, by modeling the entire atrium with all features such as buoyancy and radiation included much more complete simulations are possible. There has been some work done on this expanded use of CFD, however, important phenomena have been usually neglected. The final results are typically presented with very little in the way of systematic analysis. So far none have used ANSYS CFX. Comparison of models is not common. If CFD is to expand its role in atria simulations more detailed analysis and validation is necessary. To this author's knowledge there has yet to be a published example of a validated program that is practical for design purposes.

2.6 Summary

Atria are becoming more common and accurately modeling their performance is an important task. CFD has the potential to improve this modeling but requires a solid analysis of its models and capacity. There is a lack of published work that systematically validates CFD code. The current BES models can be adapted to account for the phenomena discussed, however, to do so requires extension empirical data of questionable accuracy. Methodological validations are an important step which must still be taken for CFD to fulfill its potential.

Chapter 3: Natural Convection Validation

3.1 Background

3.1.1 Natural Convection in Atria

The ability to successfully model natural convection and buoyant flow is essential for accurately predicting the environment in an atrium. Natural convection facilitates the interaction between the air and the surfaces and serves as a connection between the radiation that enters an atrium and the air in the atrium. Since air is a non-participating medium for radiation and optically thin, the radiation heats the air by heating the solid surfaces, which then transfer the heat to the air through natural convection. Furthermore, the buoyant flow and the high ceilings of an atrium allow for the stratification of air, and this stratification allows for natural ventilation of an atrium [Holford & Hunt, 2003]. It has been shown that natural convection can be used to significantly reduce the energy usage while providing a comfortable environment [Pfafferott, Herkel & Wambsganss, 2004]. However, an incorrectly designed atrium can prevent natural ventilation from occurring [Holford & Hunt, 2003]. Hence, natural ventilation is a desirable feature of atria but it requires careful atria design. In order to predict a design's natural ventilation performance it is necessary to be able to accurately model the underlying physical phenomena that are responsible for it. Therefore, it is essential that natural convection be able to be accurately modeled.

3.1.2 Definitions

For the purposes of this chapter and all related discussion the variables and parameters are defined in Tables 3.1 and 3.2. The properties listed below are for air at 25°C and standard pressure.

Sym	Definition	Value	Unit
A	Area of cavity wall		m^2
g	Gravity acceleration	-9.81	m/s^2
k	Thermal conductivity	2.61e-2	W/mK
L	Cavity side length		m
Q	Total heat flow		W
T	Temperature		K
T_c	Cold wall temperature		K
T_h	Hot wall temperature		K
v	Vertical velocity		m/s
α	Thermal diffusivity	2.19e-5	m^2/s
β	Thermal expansivity	3.36e-3	1/K
ν	Kinematic viscosity	1.54e-5	m^2/s

Table 3.1. Variable definitions, units and values

Variable	Equation
Dimensionless Temperature	$T_{ND} = \frac{T - T_c}{T_h - T_c}$
Dimensionless Velocity	$v_{ND} = \frac{v}{\sqrt{g\beta L(T_h - T_c)}}$
Average Nusselt Number	$\overline{Nu} = \frac{QL}{Ak(T_h - T_c)}$
Rayleigh Number	$Ra = \frac{g\beta(T_h - T_c)L^3}{\nu\alpha}$

Table 3.2. Dimensionless variable definitions

3.1.3 Models & Theory

k-ε Turbulence Model:

The k-ε turbulence model is a commonly applied two equation eddy viscosity turbulence model. The eddy viscosity is modeled as a function of the turbulent kinetic energy and the turbulent kinetic energy dissipation as shown by Launder & Spalding in 1973:

$$\mu_t = C_\mu \rho \frac{k^2}{\varepsilon} \quad (\text{Equation 3.1})$$

Transport equations for the turbulent kinetic energy (k) and the turbulent kinetic energy dissipation (ε), shown in equations 3.2 and 3.3, are used to close the Reynolds Averaged Navier-Stokes (RANS) equations [ANSYS CFX, ‘Two Equation Turbulence Modeling, 2006].

$$\frac{\partial(\rho k)}{\partial t} + \nabla \cdot (\rho U k) = \nabla \cdot \left[\left(\mu + \frac{\mu_t}{\sigma_k} \right) \nabla k \right] + P_k - \rho \varepsilon \quad (\text{Equation 3.2})$$

$$\frac{\partial(\rho \varepsilon)}{\partial t} + \nabla \cdot (\rho U \varepsilon) = \nabla \cdot \left[\left(\mu + \frac{\mu_t}{\sigma_\varepsilon} \right) \nabla \varepsilon \right] + \frac{\varepsilon}{k} (C_{\varepsilon 1} P_k - C_{\varepsilon 2} \rho \varepsilon) \quad (\text{Equation 3.3})$$

One of the advantages of the k-ε turbulence model is the value of the constants may be adapted to different flow problems [Launder & Spalding, 1973] The constants used in these simulations were provided by ANSYS CFX as [‘Lists of Symbols’, 2006]:

$$C_{\mu} = 0.09$$

$$C_{\varepsilon 1} = 1.44$$

$$C_{\varepsilon 2} = 1.92$$

$$\sigma_k = 1$$

$$\sigma_{\varepsilon} = 1.3$$

The production term is defined differently from the one shown by Launder & Spalding [1973]. It includes two additional terms, which are a term to model production near shocks and a term to model production from buoyant flows (P_{kb}). ANSYS CFX's ['Two Equation Turbulence Models', 2006] production equation is shown below.

$$P_k = \mu_t \nabla U \cdot (\nabla U + \nabla U^T) - \frac{2}{3} \nabla \cdot U (3\mu_t \nabla \cdot U + \rho k) + P_{kb} \quad (\text{Equation 3.4})$$

Near Wall Treatment

Launder & Spalding [1973] suggested two methods to adapt the k- ε turbulence model for flows near a wall; wall functions and low Reynolds number modeling. This was necessary to account for the boundary layer [Launder & Spalding, 1973]. ANSYS CFX ['Near Wall Treatment', 2006] only offers a wall function model for near wall k- ε modeling. This wall function, unlike the wall function provided by Launder & Spalding [1973], is scalable. The advantage of which is that the mesh can be arbitrary fine near the wall [ANSYS CFX, 'Mathematical Formulation, 2006]. The wall function uses the following velocity scale:

$$u^* = C_{\mu}^{1/4} k^{1/2} \quad (\text{Equation 3.5})$$

The scalable wall function acts so that the minimum value of y^* that can be used by the solver is 11.08, which is based on the value where the log law and viscous

sublayer should meet [ANSYS CFX, ‘Mathematical Formulation’, 2006]. Therefore the y^* value is defined as flows:

$$y^* = \max\left(\frac{\rho u^* \Delta y}{\mu}, 11.06\right) \quad (\text{Equation 3.6})$$

These values are then used to solve for the wall stress and friction velocity as shown in equations 3.7 and 3.8 [ANSYS CFX, ‘Mathematical Formulation, 2006].

$$u_\tau = \frac{U_t}{\frac{1}{\kappa} \ln(y^*) + C} \quad (\text{Equation 3.7})$$

$$\tau_\omega = \rho u^* u_\tau \quad (\text{Equation 3.8})$$

ANSYS CFX [‘Guidelines for Mesh Generation’, 2006] suggests that this wall treatment works best when the y^+ value of the first node is between $20 < y^+ < 100$.

Model Issues

The k- ϵ model has the advantage of being adaptable and computationally inexpensive; however, this model also suffers from several disadvantages. It assumes isotropic turbulent viscosity. In flows where is not true, such as in the flow along a twisting tape as done by Launder & Spalding [1973], agreement with experimental results are inadequate. Furthermore, the k- ϵ model does not model flow separation or flow along curved surfaces well [ANSYS CFX, ‘The k- ϵ Model’, 2006]. Over prediction of turbulence in stagnant areas can also be an issue [ANSYS CFX, ‘Model Selection and Application’, 2006].

Wilcox k- ω Turbulence Model:

The Wilcox k- ω model is a two equation eddy viscosity turbulence model. The eddy viscosity is modeled as a function of the turbulent kinetic energy (k) and turbulent frequency (ω) [ANSYS CFX, ‘Two Equation Turbulence Models’, 2006].

$$\mu_t = \rho \frac{k}{\omega} \quad (\text{Equation 3.9})$$

This turbulence model uses transport equations of the turbulent kinetic energy (k) and the turbulent frequency (ω) to close the RANS equations. Equations 3.10 and 3.11 show these two transport equations [ANSYS CFX, ‘Two Equation Turbulence Models’, 2006].

$$\frac{\partial(\rho k)}{\partial t} + \nabla \cdot (\rho U k) = \nabla \cdot \left[\left(\mu + \frac{\mu_t}{\sigma_k} \right) \nabla k \right] + P_k - \beta' \rho k \omega \quad (\text{Equation 3.10})$$

$$\frac{\partial(\rho \omega)}{\partial t} + \nabla \cdot (\rho U \omega) = \nabla \cdot \left[\left(\mu + \frac{\mu_t}{\sigma_\omega} \right) \nabla \omega \right] + \alpha \frac{\omega}{k} (P_k) - \beta \rho \omega^2 \quad (\text{Equation 3.11})$$

The Wilcox k- ω turbulence model uses the same equation for the P_k term as the k- ϵ model. The constants used in these simulations were provided by ANSYS CFX [‘Two Equation Turbulence Models’, 2006] are consistent with those provided by Wilcox [1993]:

$$\beta' = 0.09$$

$$\alpha = 5/9$$

$$\beta = 0.075$$

$$\sigma_k = 2$$

$$\sigma_\omega = 2$$

Near Wall Treatment

In ANSYS CFX the near wall treatment of the k- ω turbulence model is an automatic wall treatment. This is a combination of a low Reynolds number model and a wall function. ANSYS CFX [‘Mathematical Formulation’, 2006] uses the following equations for the wall function.

$$u_{\tau} = \sqrt{\nu \left| \frac{\Delta U}{\Delta y} \right|} \quad (\text{Equation 3.12})$$

$$\omega_l = \frac{1}{a_1 \kappa} \frac{u^*{}^2}{y^+} \quad (\text{Equation 3.13})$$

$$\omega_s = \frac{6\nu}{\beta(\Delta y)^2} \quad (\text{Equation 3.14})$$

$$\omega_{\omega} = \omega_s \sqrt{1 + \frac{\omega_l}{\omega_s}} \quad (\text{Equation 3.15})$$

Model Issues

The Wilcox k- ω turbulence model shows strong dependency on the free stream conditions and is dependent on user input [ANSYS CFX, ‘Model Selection and Application’, 2006]. The model also is insensitive to streamline curvature and rotating flows [ANSYS CFX, Model Selection and Application, 2006].

Shear Stress Transport (SST) Turbulence Model:

The shear stress transport model is a two equation eddy viscosity model that blends the k- ϵ and the Wilcox k- ω model. The k- ω model remains unchanged and the k- ϵ model is modified as below.

$$\frac{\partial(\rho k)}{\partial t} + \nabla \cdot (\rho U k) = \nabla \cdot \left[\left(\mu + \frac{\mu_t}{\sigma_k} \right) \nabla k \right] + P_k - \beta' \rho k \omega \quad (\text{Equation 3.16})$$

$$\frac{\partial(\rho \omega)}{\partial t} + \nabla \cdot (\rho U \omega) = \nabla \cdot \left[\left(\mu + \frac{\mu_t}{\sigma_{\omega 2}} \right) \nabla \omega \right] + \frac{2\rho \nabla k \nabla \omega}{\sigma_{\omega 2} \omega} + \alpha_2 \frac{\omega}{k} (P_k) - \beta_2 \rho \omega^2$$

(Equation 3.17)

The constants used in these simulations were provided by ANSYS CFX as [‘Two Equation Turbulence Models’, 2006]:

$$\begin{aligned} \beta' &= 0.09 \\ \alpha_1 &= 5/9 \\ \beta_1 &= 0.075 \\ \sigma_{k1} &= 2 \\ \sigma_{\omega 1} &= 2 \\ \alpha_2 &= 0.44 \\ \beta_2 &= 0.0828 \\ \sigma_{k2} &= 1 \\ \sigma_{\omega 2} &= 1/0.0856 \end{aligned}$$

A blending function is used to combine the two turbulence models. The k- ω model equations were multiplied by F_1 and the modified k- ϵ model equations were multiplied by $(1-F_1)$, then the two k equations and two ω equations were combined. Therefore, the coefficients for each term are a combination of the coefficients for each model. This is shown in equation 3.18, where Φ represents a coefficient.

$$\Phi_3 = F_1 \Phi_1 + (1 - F_1) \Phi_2 \quad (\text{Equation 3.18})$$

This yields two equations as shown by ANSYS CFX [‘Two Equation Turbulence Models’, 2006]

$$\frac{\partial(\rho k)}{\partial t} + \nabla \cdot (\rho U k) = \nabla \cdot \left[\left(\mu + \frac{\mu_t}{1} \right) \nabla k \right] + P_k - \beta' \rho k \omega \quad (\text{Equation 3.19})$$

$$\frac{\partial(\rho \omega)}{\partial t} + \nabla \cdot (\rho U \omega) = \nabla \cdot \left[\left(\mu + \frac{\mu_t}{\sigma_{\omega 3}} \right) \nabla \omega \right] + (1 - F_1) \frac{2\rho \nabla k \nabla \omega}{\sigma_{\omega 2} \omega} + \alpha_3 \frac{\omega}{k} (P_k) - \beta_3 \rho \omega^2 \quad (\text{Equation 3.20})$$

F_1 is the blending function and is defined by equations 3.21 to 3.23.

$$F_1 = \tanh(\arg_1^4) \quad (\text{Equation 3.21})$$

$$\arg_1 = \min \left(\max \left(\frac{\sqrt{k}}{0.09 \omega y}, \frac{500 \nu}{y^2 \omega} \right), \frac{4 \rho k}{CD_{kw} \sigma_{\omega 2} y^2} \right) \quad (\text{Equation 3.22})$$

$$CD_{kw} = \max \left(2\rho \frac{1}{\sigma_{\omega 2}} \nabla k \nabla \omega, 1.0 \times 10^{-10} \right) \quad (\text{Equation 3.23})$$

The SST model uses a blending function to limit the eddy viscosity in the boundary layer. The equation for the eddy viscosity is modified to produce the smallest eddy viscosity. Equation 3.24 shows the original definition of the eddy viscosity and equation 3.25 shows the modified definition.

$$v_t = \frac{\mu_t}{\rho} \quad (\text{Equation 3.24})$$

$$v_t = \frac{a_1 k}{\max(a_1 \omega, SF_2)} \quad (\text{Equation 3.25})$$

The quantity S is an invariant measure of the strain rate equal to $\left| \frac{\partial u}{\partial y} \right|$ and a_1 is the Bradshaw constant [Menter, 1996]. The blending function limits the reduction of the eddy viscosity to the boundary layer and is defined in equations 3.26 to 3.27.

$$F_2 = \tanh(\arg_2^2) \quad (\text{Equation 3.26})$$

$$\arg_2 = \max\left(\frac{2\sqrt{k}}{0.09\omega y}, \frac{500\nu}{y^2\omega}\right) \quad (\text{Equation 3.27})$$

This makes the SST model different from other blended models in that it uses the $k-\omega$ model in both the sub layer of and log-law region of the boundary layer [Menter, 1996]. It also limits the eddy viscosity in the boundary layer to more accurately model transport of shear stress [ANSYS CFX, ‘Two Equation Turbulence Models’,2006].

Near Wall Treatment

The near wall treatment is identical to that of the $k-\omega$ model mentioned previously.

Model Issues

The SST model is designed to increase the accuracy of the model in adverse pressure gradients and remove the $k-\omega$ model’s dependency on free stream quantities.

Buoyancy Turbulence Production Model:

ANSYS CFX offers an optional production term for buoyant flows. The production term model accounts for the additional production of turbulent kinetic energy arising from density gradients [ANSYS CFX, 2006]. This term can be included in either one or both of the additional transport equations of a two-equation turbulence model. Thus the term can be in only the turbulent kinetic equation or in both the turbulent kinetic energy equation and either the dissipation or the frequency equation, depending on the

turbulence model used. The actual term is defined, for the Boussinesq buoyancy model, in equation 3.28 [ANSYS CFX, 2006]

$$P_{kb} = -\frac{\mu_t \beta}{0.9 \rho} g \cdot \nabla T = -\frac{k \beta}{0.9 \omega} g \cdot \nabla T = -\frac{C_\mu \beta k^2}{0.9 \varepsilon} g \cdot \nabla T \quad (\text{Equation 3.28})$$

When this term is applied to either the ε or the ω equation, the definition is changed according to equation 3.29 [ANSYS CFX, 2006].

$$P_{kb} = C_3 \max\left(-\frac{\mu_t}{0.9 \rho} \beta g \cdot \nabla T, 0\right) \quad (\text{Equation 3.29})$$

In the cases dealt with in this thesis it can be assumed that gravity acts solely in the negative y direction. This allows for the production term to be further simplified to equation 3.30.

$$P_{kb} = -\frac{\mu_t \beta}{\rho} 10.9 \frac{\partial T}{\partial y} \quad (\text{Equation 3.30})$$

Relaxation:

Relaxation is used in an iterative process to adjust how much the solution changes with each iteration. The relaxation factor is multiplied by the change calculated by the iterative process to derive what change is actually applied. Equation 3.31 shows this principle where R is the relaxation factor.

$$T^{New}_{Actual} = T^{Old} + R(T^{New}_{Calculated} - T^{Old}) \quad (\text{Equation 3.31})$$

If the relaxation factor is unity then the new value of the variable is the value calculated by the equations of the iterative process. If R is a value other than unity the

new value of the variable will be different than the one calculated by the equations of the iterative process. This effectively either reduces or increases the change in the variable between iterations. It has been found necessary to use values of R less than one, known as under relaxation, in order for turbulent natural convection simulations to converge. This was highlighted in the work by Henkes and Hoogendoorn [1995], which compared several different attempts to model turbulent natural convection, all of which required under-relaxation.

3.2 Simulations

3.2.1 Laminar Natural Convection in a Square Cavity

Description:

A square cavity filled with air, which has a temperature difference between the vertical walls of $10.65\text{ }^{\circ}\text{C}$ was simulated. This temperature difference drives a laminar natural convection regime, which creates a circulating flow within the cavity. Fluid properties used are listed in Table 3.1. By adjusting the length of the cavity's side the Rayleigh number can be adjusted for each simulation, the definition of which is included in Table 3.2.

Measurement:

The average Nusselt number was used as a measurement of accuracy. Table 3.2 contains the definition of the average Nusselt number.

Validation:

The paper by Hortmann et. al. [1990] was used to supply the appropriate average Nusselt numbers for the three Rayleigh numbers. The simulations were run using a series of increasingly fine meshes and the extrapolation technique detailed in Appendix B was used to extrapolate the solution for an infinitely fine mesh.

Variations:

Each test case dealt with a different laminar Rayleigh number. As stated in the description the change in the Rayleigh number is created by a change in the side length of the cavity. Table 3.3 outlines the parameters for each Rayleigh number.

Case Number	Rayleigh Number	Side Length	Benchmark Nusselt Number
1A	10^4	0.02126 m	2.245
1B	10^5	0.09867 m	4.522
1C	10^6	0.21260 m	8.825

Table 3.3 List of Laminar Simulations Run and Related Parameters

Domain:

The domain consisted of a two-dimensional square filled by air, with properties consistent with a temperature of 25°C and a standard pressure. The value of these properties can be found in Table 3.1. Figure 3.1 is an illustration of the domain and its relevant features.

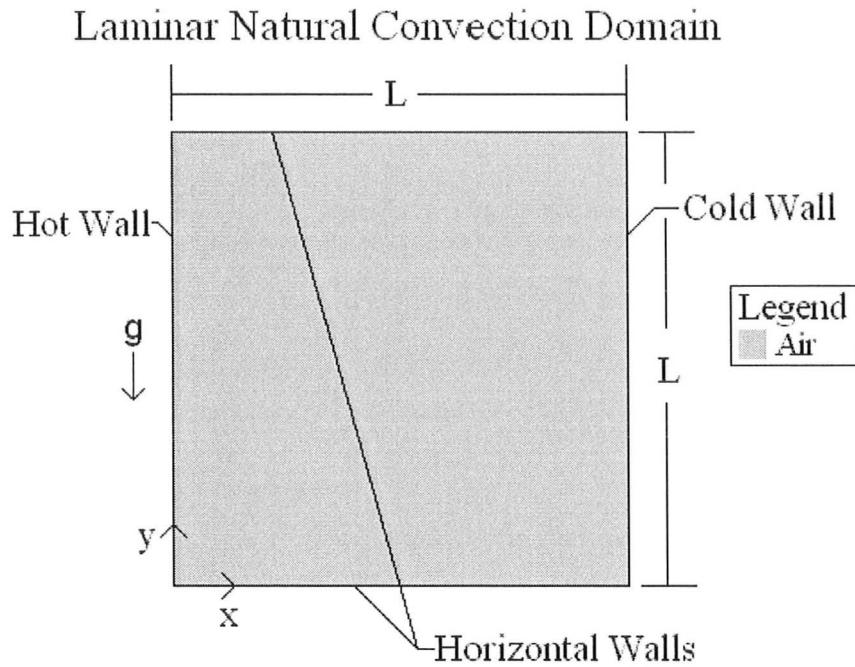


Figure 3.1 Sample domain for the laminar natural convection simulations

Boundary Conditions:

Hot Wall: The hot wall was a no slip wall with a specified uniform temperature of 285.8 K.

Cold Wall: The cold wall was a no slip wall with a specified uniform temperature of 275.15 K.

Horizontal Walls: The horizontal walls were treated as no slip adiabatic walls.

Meshes:

Two-dimensional uniform meshes were used with the number of nodes per side of the square starting at twenty and doubling with each level of refinement. The finest mesh had three hundred and twenty nodes per side.

Results:

Table 3.4 shows the calculated average Nusselt numbers for all of the laminar natural convection simulations, along with the appropriate percentage error.

Nodes Per Side	Ra 10 ⁴		Ra 10 ⁵		Ra 10 ⁶	
	Average Nusselt Number	% Error	Average Nusselt Number	% Error	Average Nusselt Number	% Error
20	2.432	8.33%	5.362	18.58%	8.968	1.62%
40	2.290	2.00%	4.815	6.48%	10.206	15.65%
80	2.254	0.40%	4.595	1.61%	9.284	5.20%
160	2.245	0.00%	4.538	0.35%	8.937	1.27%
320			4.518	0.09%	8.822	0.03%
Extrapolated	2.242	0.13%	4.507	0.33%	8.765	0.68%
Hortmann et. al	2.245		4.522		8.825	

Table 3.4 Average Nusselt Numbers for All Laminar Simulations with Percentage Errors

Table 3.4 also shows the extrapolated Nusselt number for an infinitely fine grid and its percentage error. The extrapolation used is based on the assumption that the error in the average Nusselt number is proportional to the grid spacing raised to an exponent, as shown in equation 3.32.

$$Error = (Nu - Nu_{\infty}) = A(\Delta x)^B \quad \text{(Equation 3.32)}$$

Appendix B explores this extrapolation further. It should be noted that even without the extrapolation the error was less than one percent at the finest mesh for each simulation. Figure 3.2 shows the progression of the temperature distribution in the cavity as the Rayleigh number of the simulation increases.

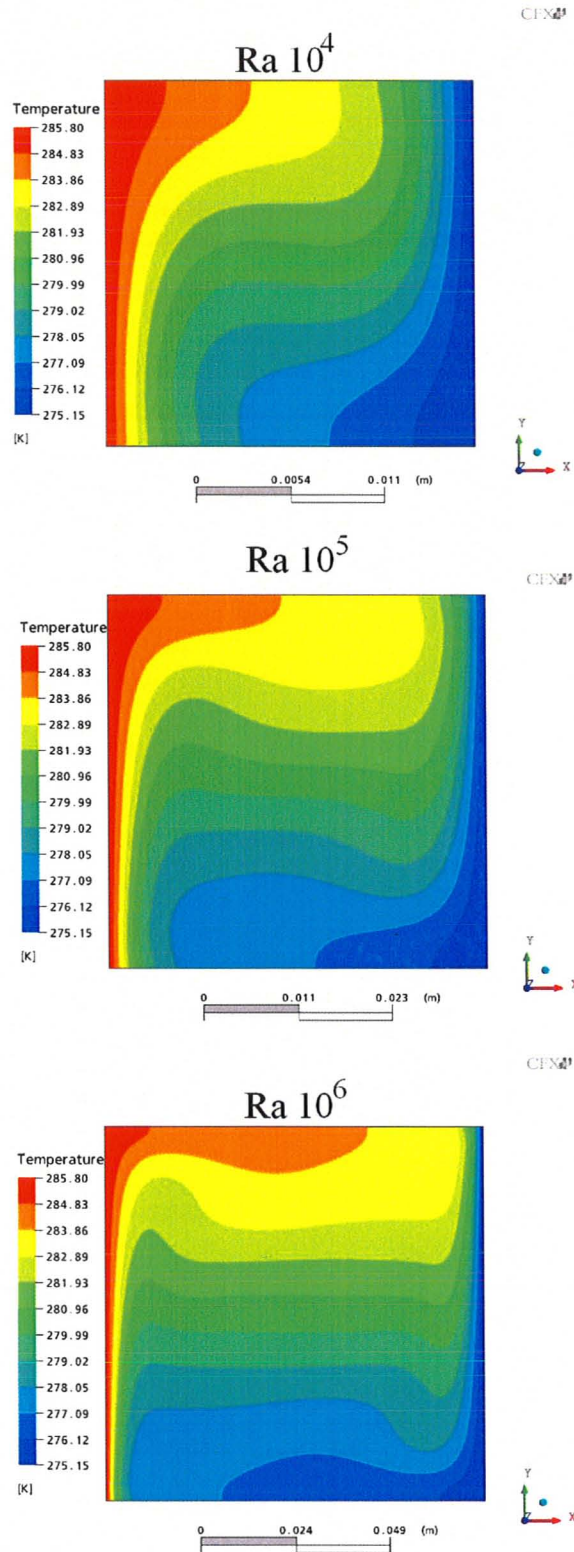


Figure 3.2. Temperature Distributions in Cavity for Different Rayleigh Numbers

This trend matches that shown in the results of Hortmann et al [1990].

Discussion:

Extrapolated Values

Figures 3.3, 3.4 and 3.5 show the average Nusselt number plotted against the number of nodes per side of the mesh, for the Rayleigh numbers 10^4 , 10^5 and 10^6 respectively.

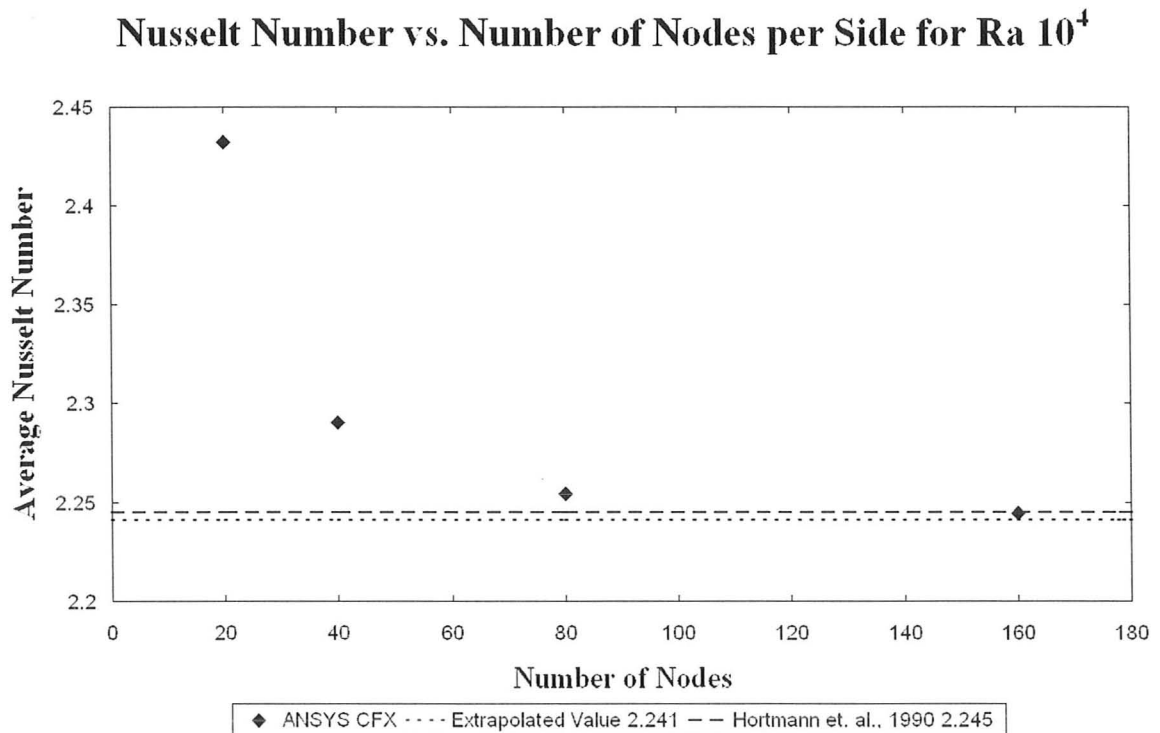


Figure 3.3 Average Nusselt Number for Square Cavity with Rayleigh Number 10^4 vs. the Number of Nodes in Each Direction

Nusselt Number vs. Number of Nodes per Side for Ra 10^5

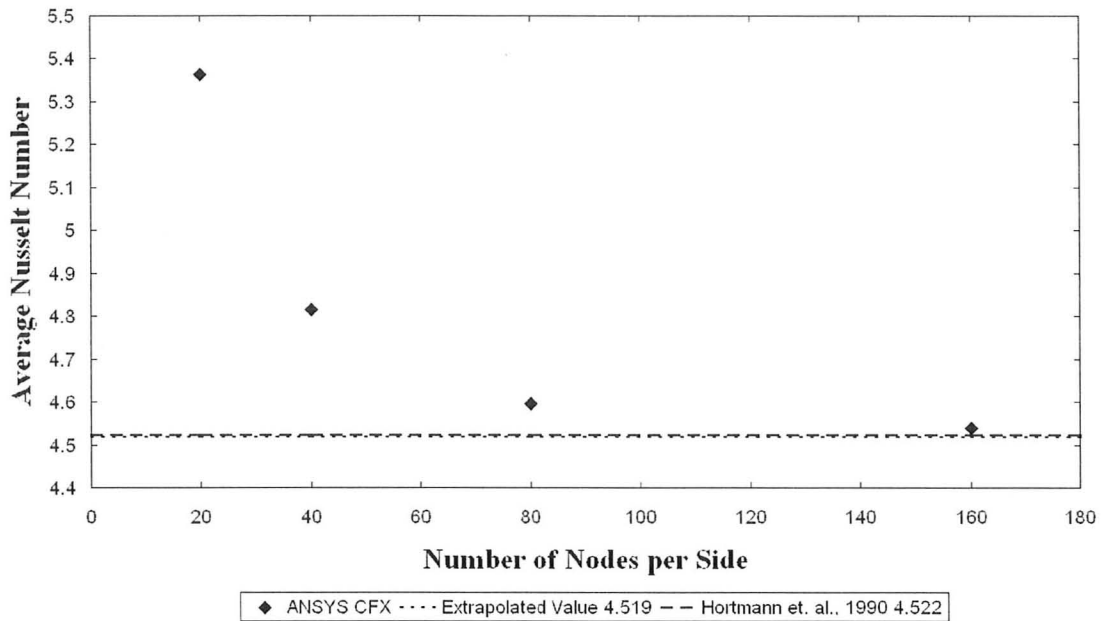


Figure 3.4 Average Nusselt Number for a Square Cavity with Rayleigh Number of 10^5 vs. the Number of Nodes in Each Direction

Nusselt Number vs. Number of Nodes per Side for Ra 10^6

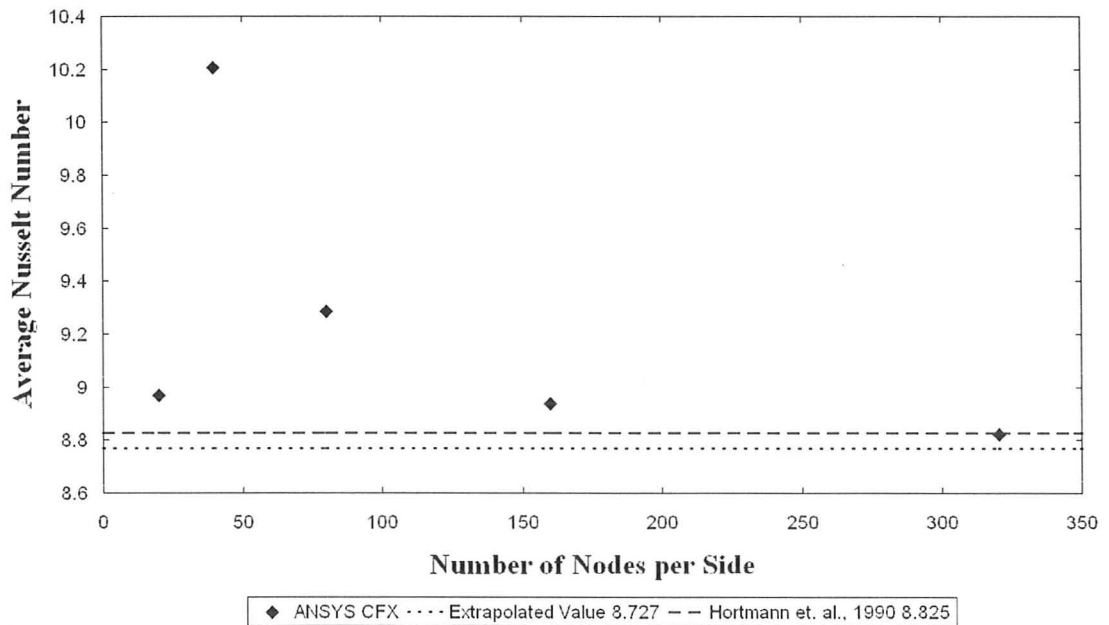


Figure 3.5 Average Nusselt Number for Square Cavity with Rayleigh Number 10^6 vs. the Number of Nodes in Each Direction

These three figures all show that as the mesh is refined the accuracy of the predictions increases. An exception is seen in Figure 3.5, the first data point does not follow the standard trend in data. This is likely because the mesh is too coarse for the assumptions of the extrapolation model to be valid. This would suggest that higher Rayleigh numbers require a finer grid for the same level of accuracy. This is supported by the fact that percentage error in the extrapolation is directly linked to the Rayleigh number, as shown by Table 3.4 which has the percentage error increasing with the Rayleigh number. This is also consistent with the physics since the boundary layer becomes thinner as the Rayleigh number increases.

Sensitivity of Extrapolations

If the extrapolation were correct then the extrapolated value should be the same whether it used the three coarsest meshes or the three finest meshes of a set of four meshes that are sufficiently fine. In order to test, this the simulations for each Rayleigh number included at least four meshes that showed the expected behaviour. The extrapolated values in Table 3.4 used only the three finest of the meshes. However, Table 3.5 below contrasts the extrapolated values using the three coarsest meshes and the three finest meshes.

	Ra 10^4			Ra 10^5			Ra 10^6		
	Nu	Order	% Error	Nu	Order	% Error	Nu	Order	% Error
Coarse Extrapolation	2.242	1.98	0.14%	4.518	1.95	0.08%	8.728	1.41	1.11%
Fine Extrapolation	2.242	2.00	0.13%	4.507	1.51	0.32%	8.765	1.59	0.68%
Absolute Change	0.000	0.020		0.011	0.438		0.037	0.183	
Percentage Change	0.01%	1.02%		0.24%	22.45%		0.43%	13.01%	

Table 3.5 Change in Extrapolation with Addition of Finer Meshes

The change in average Nusselt number was less than half of a percent in each simulation. In the simulation with the lowest Rayleigh number the change was less than a one thousandth decimal place. It should be noted that the percentage change increased with the Rayleigh number, suggesting that the extrapolation require finer grids at higher Rayleigh numbers. In addition, the order of the solution becomes lower as the Rayleigh number increases. At a Rayleigh number of 10^4 the extrapolation is second order but drops to approximately 1.5 by the Rayleigh number of 10^6 .

Conclusions:

Using the extrapolation CFX was able to predict average Nusselt numbers within one percent or less compared to the published benchmark solutions. Even without the extrapolation, CFX managed to predict the average Nusselt number for all three cases by less than one percent. It is also seen that higher Rayleigh numbers require finer meshes, as expected.

3.2.2 Turbulent Natural Convection in a Square Cavity

Description:

This case considers a two dimensional air filled square cavity with a temperature difference between the vertical walls. The simulation is very similar to the laminar cases, however, the temperature difference and magnitude of the cavity's sides are sufficient for the natural convection to be turbulent with a Rayleigh number of 1.58×10^9 [Ampofo & Karayiannis, 2003]. The goal of this section is to assess the capability of various turbulence models to predict the measured data.

Measurement:

There are three variables that are used to judge the accuracy of a simulation; the average Nusselt number, the temperature along the center of the cavity and the velocity component v along the center of the cavity. The experimental error in the measurements reported by Ampofo & Karayiannis [2003] for the air temperature is 0.1 K, 0.07% for the air velocity and 0.25%-1.13% for the Nusselt numbers.

Validation:

The simulation results were validated against the experimental results of a three-dimensional rectangular cavity of the same Rayleigh number published by Ampofo and Karayiannis in 2003. The experimental set up was a long three dimensional rectangular cavity filled with air. Two of the sides were 0.75 meters long with the third side measuring twice the length at 1.5 meters. The measurements were taken at the mid point of the longest side in order to eliminate three dimensional effects and produce two

dimensional data in a square area. The measurements included the air velocity and temperature along the horizontal centerline of the square cavity. The top, bottom and end walls were insulated, although there was still some heat loss through the top and bottom walls. The remaining vertical walls were held at different constant temperatures. Figure 3.6 shows the layout of the experimental cavity.

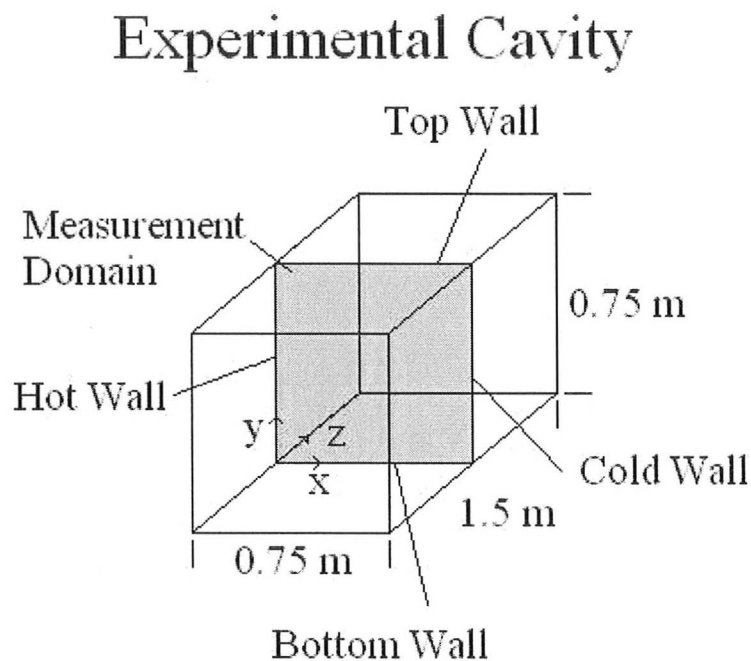


Figure 3.6 Layout of Cavity Used in Experimental Work

Variations:

A series of simulations were performed which considered a range of turbulence models and buoyancy models. These simulations were classified into two groups. The first group compared the results of available turbulence models. This group is referred to as the standard simulations. The second compared the effect of an optional buoyancy

turbulence production model, which is described in the Models & Theory section. Table 3.6 below outlines each simulation and its respective parameters.

Case Number	Turbulence Model	Buoyancy Turbulence Production Term
1A	k- ϵ Turbulence Model	None
1B	k- ω Turbulence Model	None
1C	SST Turbulence Model	None
2A	k- ϵ Turbulence Model	Production
2B	k- ϵ Turbulence Model	Production & Dissipation
2C	k- ω Turbulence Model	Production
2D	k- ω Turbulence Model	Production & Dissipation
2E	SST Turbulence Model	Production
2F	SST Turbulence Model	Production & Dissipation

Table 3.6 Variations of Turbulent Natural Convection Simulation

Domain:

The domain consisted of a two dimensional square cavity with sides 0.75 meters long. The cavity is filled with air, with physical properties consistent with a temperature of 25°C and standard pressure. The fluid is buoyant with acceleration due to gravity in the same direction as the negative y-axis. The temperature difference between the vertical walls yield a turbulent domain with a Rayleigh number of 1.58×10^9 [Ampofo & Karayiannis, 2003]. Figure 3.7 below shows the domain and the centerline that the measurements of the temperature and velocity were taken along.

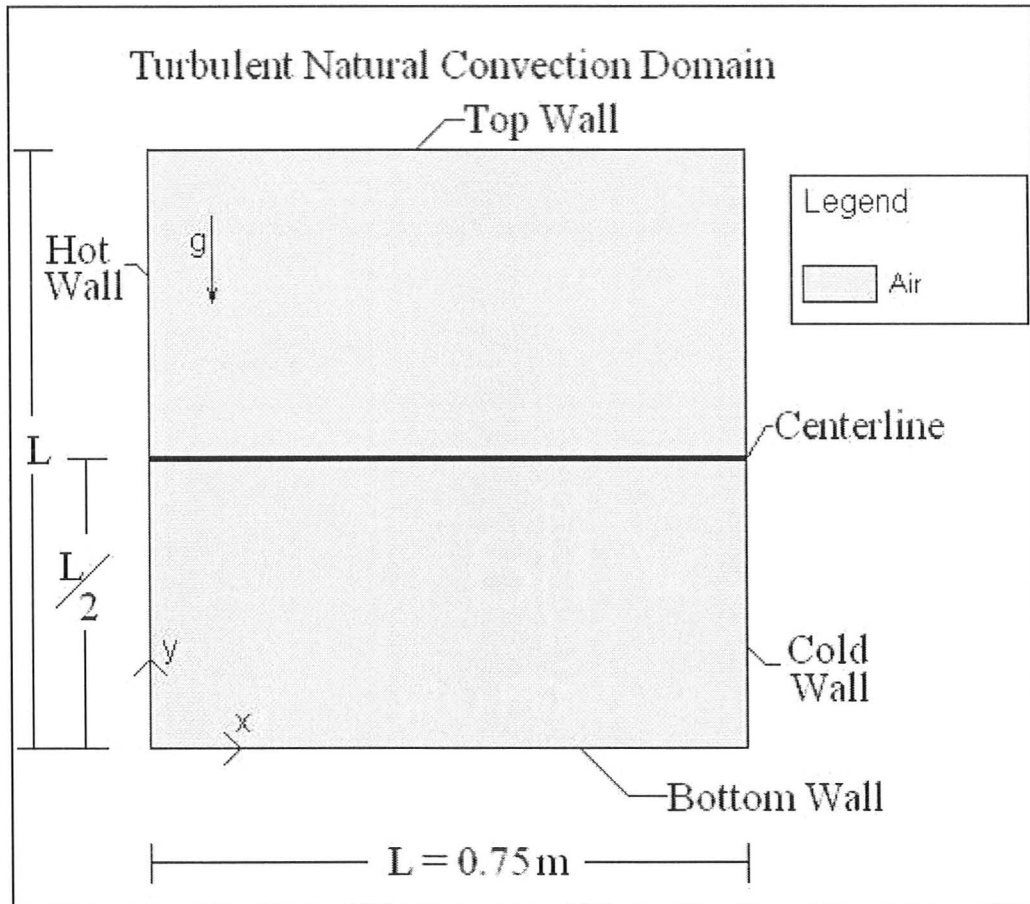


Figure 3.7 Turbulent Natural Convection Domain with Centerline Indicated

Boundary Conditions:

Hot Wall: The hot wall was a no slip wall with a specified uniform temperature of 321.56 °K.

Cold Wall: The cold wall was a no slip wall with a specified uniform temperature of 283.15 °K.

Horizontal Walls: The horizontal walls were treated as no slip walls. The energy boundary conditions were a polynomial specified temperature which was designed to match the experimental data.

Meshes:

The mesh shown in Figure 3.8 is the mesh used in these validations.

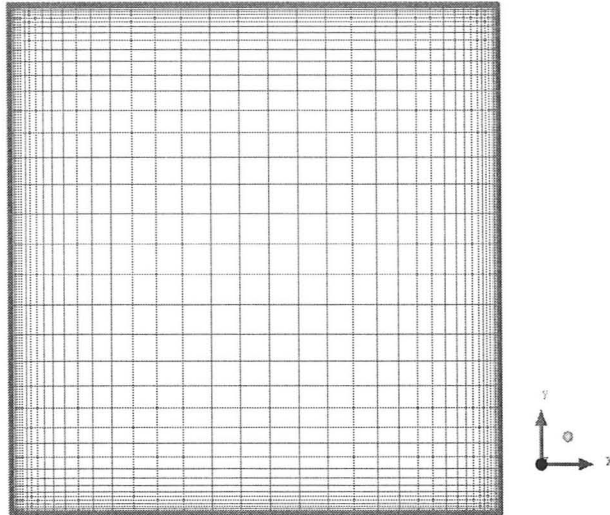


Figure 3.8 80x80 expanding mesh used as standard mesh for turbulent natural convection simulations

The mesh was based on a similar grid used by Davidson in the paper presented by Henkes and Hoogendoorn in 1995. It was an expanding mesh with eighty nodes per side of the cavity and an expansion factor of 1.27. An expanding 160x160 grid was also used for confirming grid independence.

Results:

Velocity

The velocity component v , which is in the positive y direction, was used to measure the accuracy of the simulations with respect to velocity. The velocity component was measured across the entire width of the cavity at a height equal to half of its total height. Figure 3.9 below shows the comparison of the simulations and the benchmark data.

Velocity Component v Profiles at $Y/L=0.5$

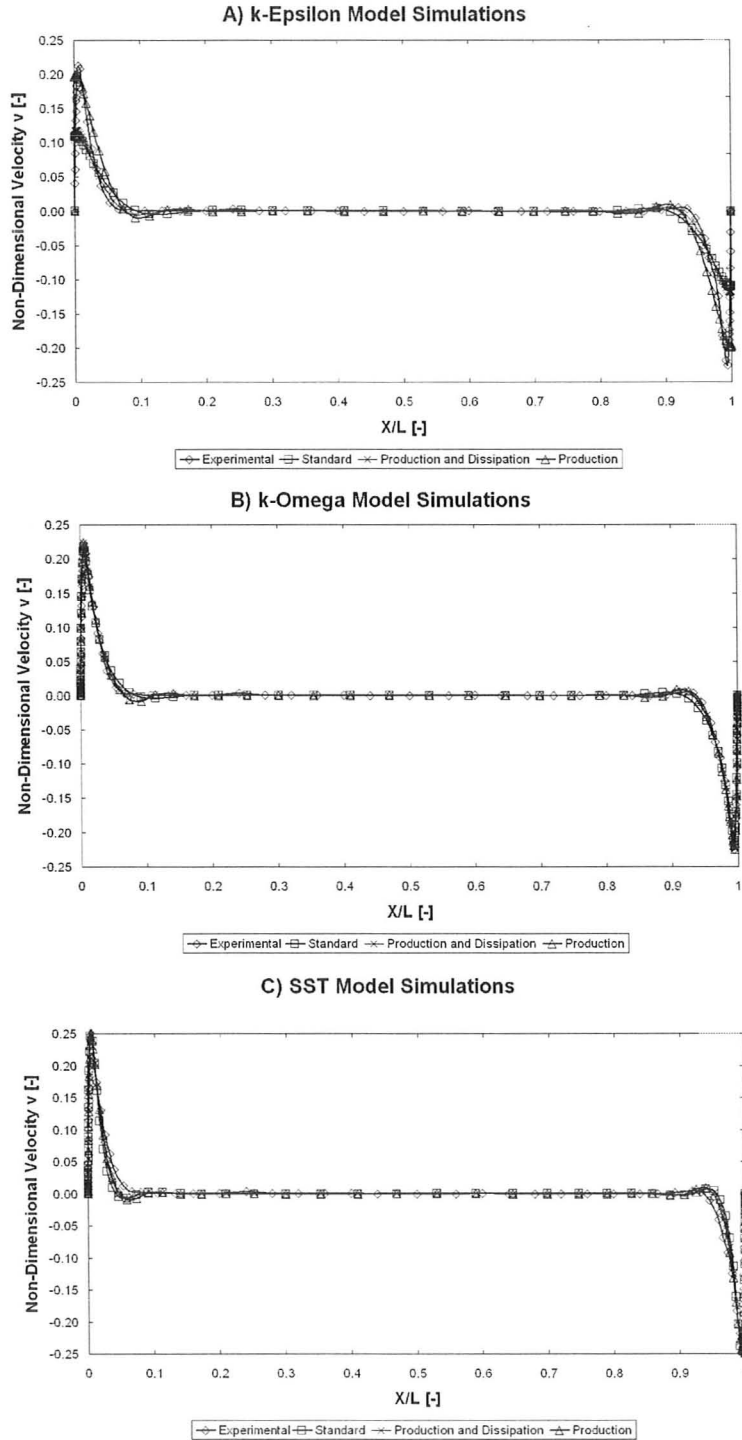


Figure 3.9 Velocity v Component for A) $k-\epsilon$ Model, B) $k-\omega$ Model C) SST Model and Experimental Data

Enlarged images of the velocity profiles in the boundary layer are located in the discussion section. Even in this level of detail it is clear that the k- ϵ model does not match the experimental velocity profile as well as the k- ω and SST model.

In addition, the magnitude of the velocity peaks in the boundary layers were measured and compared with those of the experimental data. Table 3.7 shows the values of the velocity peaks and percentage errors for all of the simulations.

k- ϵ Turbulence Model							
Experimental		Standard		Production		Production & Dissipation	
Wall	V [m/s]	V [m/s]	% Error	V [m/s]	% Error	V [m/s]	% Error
Hot Wall	0.213	0.110	48.4%	0.119	44.1%	0.119	44.1%
Cold Wall	-0.226	-0.111	-50.9%	-0.120	-46.9%	-0.119	-47.3%
k- ω Turbulence Model							
Experimental		Standard		Production		Production & Dissipation	
Wall	V [m/s]	V [m/s]	% Error	V [m/s]	% Error	V [m/s]	% Error
Hot Wall	0.213	0.219	2.8%	0.224	5.2%	0.224	5.2%
Cold Wall	-0.226	-0.219	-3.2%	-0.224	-0.88%	-0.224	-0.88%
Shear Stress Transport Turbulence Model							
Experimental		Standard		Production		Production & Dissipation	
Wall	V [m/s]	V [m/s]	% Error	V [m/s]	% Error	V [m/s]	% Error
Hot Wall	0.213	0.259	21.6%	0.244	14.6%	0.249	16.9%
Cold Wall	-0.226	-0.259	-14.6%	-0.245	-8.4%	-0.250	-10.6%

Table 3.7 Velocity Peak Magnitudes in Boundary Layers for Simulations

As the above table shows, there is an asymmetry to the velocity profile for the experimental data that was not obvious from the previous figures. Although the difference is approximately one hundredth of a meter per second, if considered as a percentage the difference is approximately six percent.

Temperature

The temperature along the centerline was also compared to the benchmark data. Figure 3.10 shows the temperature profile for the simulations and the experimental data.

Temperature Profiles at $Y/L=0.5$

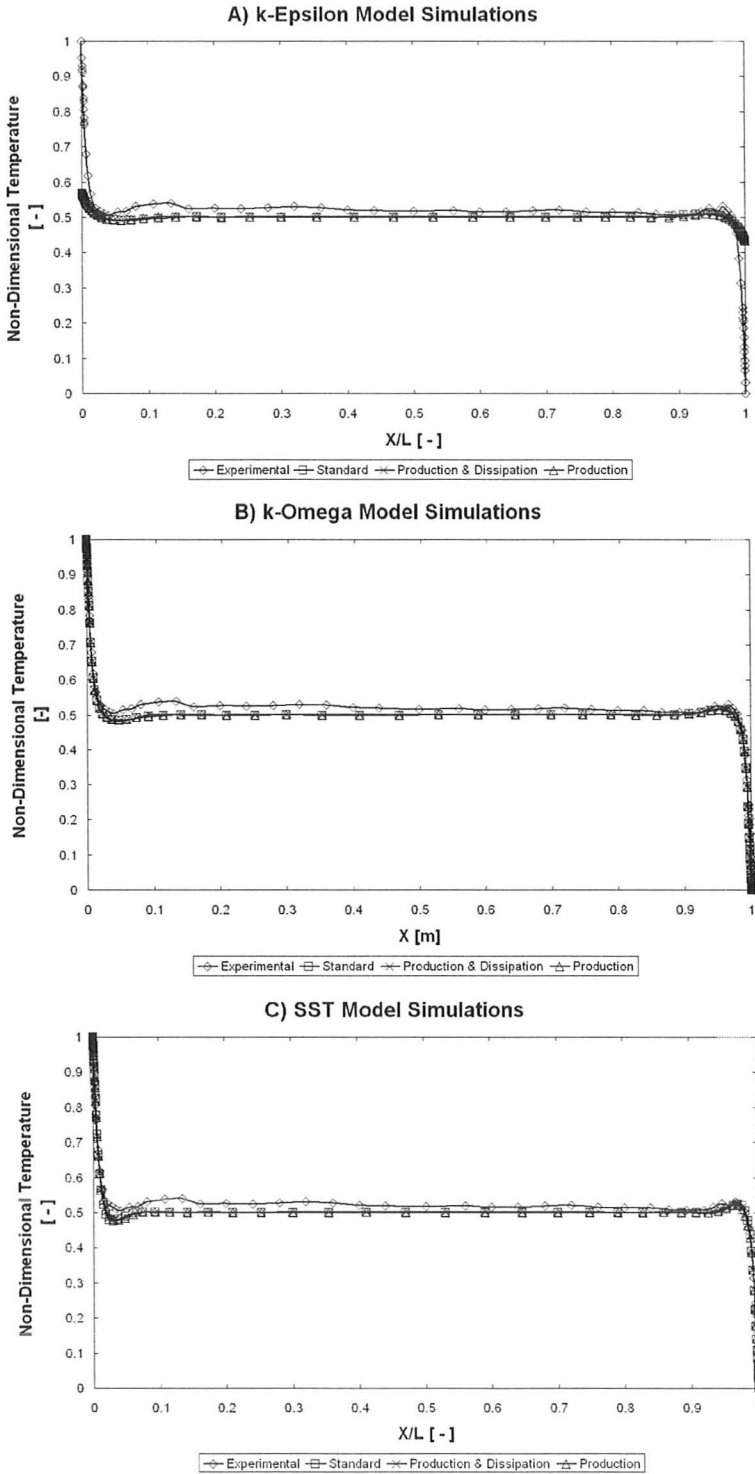


Figure 3.10 Temperature Profiles for A) k- ϵ Model, B) k- ω Model C) SST Model and Experimental Data

It should be noted that all of the simulations under-predicted the temperature in the middle portion of the centerline.

Average Nusselt Number

The average Nusselt number for each simulation was calculated using the definition in Table 3.2. The percentage error is based on the experimental values provided by Ampofo and Karayiannis [2003]. Table 3.8 shows the experimental average Nusselt numbers for the each surface and each of the simulation’s corresponding average Nusselt numbers and associated percentage errors.

k-ε Turbulence Model							
Experimental		Standard		Production		Prod. & Dis.	
Surface	Nu	Nu	% Error	Nu	% Error	Nu	% Error
Hot Wall	62.9	24.8	60.57%	24.1	61.69%	23.6	62.48%
Cold Wall	62.6	24.8	60.38%	24.1	61.50%	23.6	62.30%
Bottom	13.9	6.1	56.12%	4.9	64.75%	5.3	61.87%
Top	14.4	5.3	63.19%	4.7	67.36%	5.0	65.28%
Average			60.07%		63.82%		62.98%
k-ω Turbulence Model							
Experimental		Standard		Production		Prod.& Dis.	
Surface	Nu	Nu	% Error	Nu	% Error	Nu	% Error
Hot Wall	62.9	56.94	9.48%	57.19	9.08%	58.33	7.27%
Cold Wall	62.6	57.07	8.83%	59.36	5.18%	58.43	6.66%
Bottom	13.9	8.69	37.48%	11.25	19.06%	10.04	27.77%
Top	14.4	8.62	40.14%	9.07	37.01%	9.94	30.97%
Average			23.98%		17.58%		18.17%
SST Turbulence Model							
Experimental		Standard		Production		Prod. & Dis.	
Surface	Nu	Nu	% Error	Nu	% Error	Nu	% Error
Hot Wall	62.9	55.2	12.24%	57.54	8.52%	56.83	9.65%
Cold Wall	62.6	55.26	11.73%	57.68	7.86%	56.87	9.15%
Bottom	13.9	10.93	21.37%	11.5	17.27%	11.36	18.27%
Top	14.4	10.87	24.51%	11.35	21.18%	11.33	21.32%
Average			17.46%		13.71%		14.60%

Table 3.8 Average Nusselt Numbers for all of the Surfaces in the k-ω Simulations

Discussion:

Under-Relaxation

In order to converge, the momentum and mass equations had to be under-relaxed. The exact value used varied with each simulation, however, the value was typically in the range between 0.65 and 0.9. There was no predictable pattern to the correct relaxation number. Figure 3.11 shows the effect that the relaxation factor can have by contrasting the residual history of simulations that are identical except for the relaxation factors of 0.9 and 0.8, respectively.

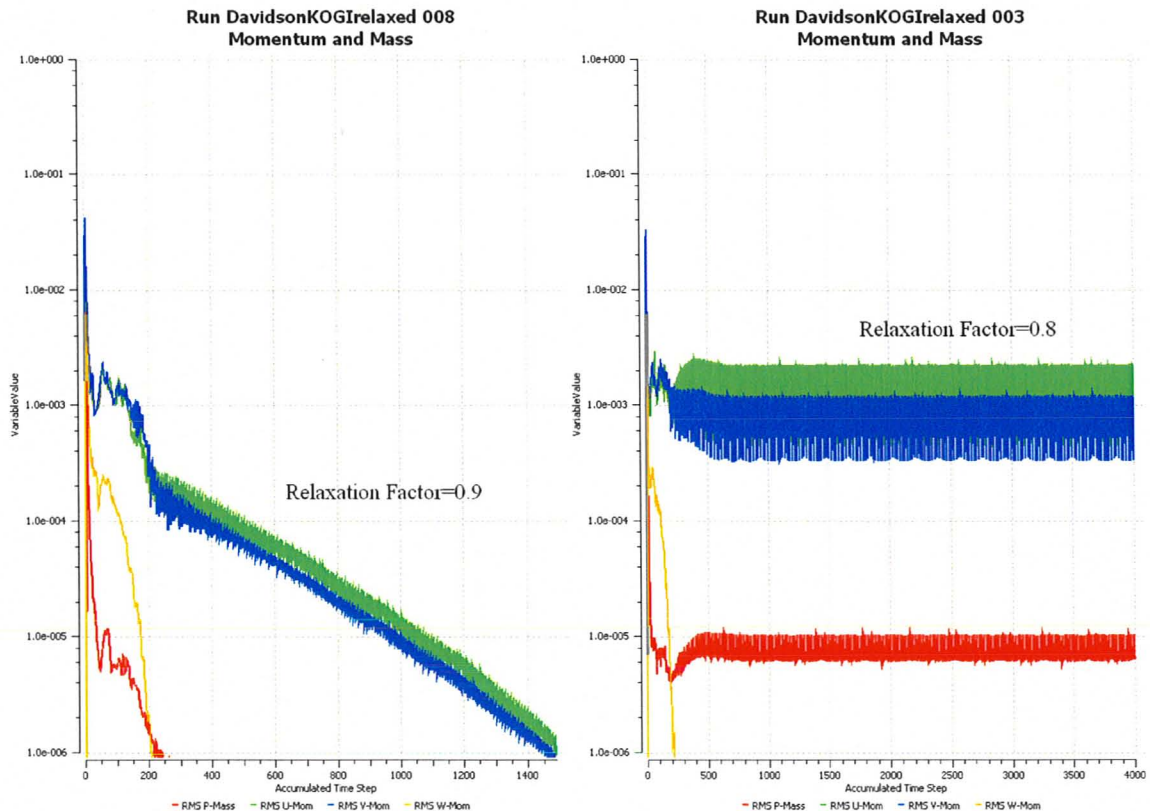


Figure 3.11 The Effect of the Relaxation Number on Otherwise Identical Simulations

Clearly the relaxation factor plays a significant role in the convergence of simulations.

Grid Independence

The simulations produced grid independent results. This can be seen in the average Nusselt numbers, the temperature profiles and the velocity profiles. As discussed in the mesh section, the mesh which was used for grid independence had twice the number of nodes and the same expansion factor. Figure 3.12 contrasts the velocity profile within the boundary layer of the two meshes run with the standard $k-\omega$ model.

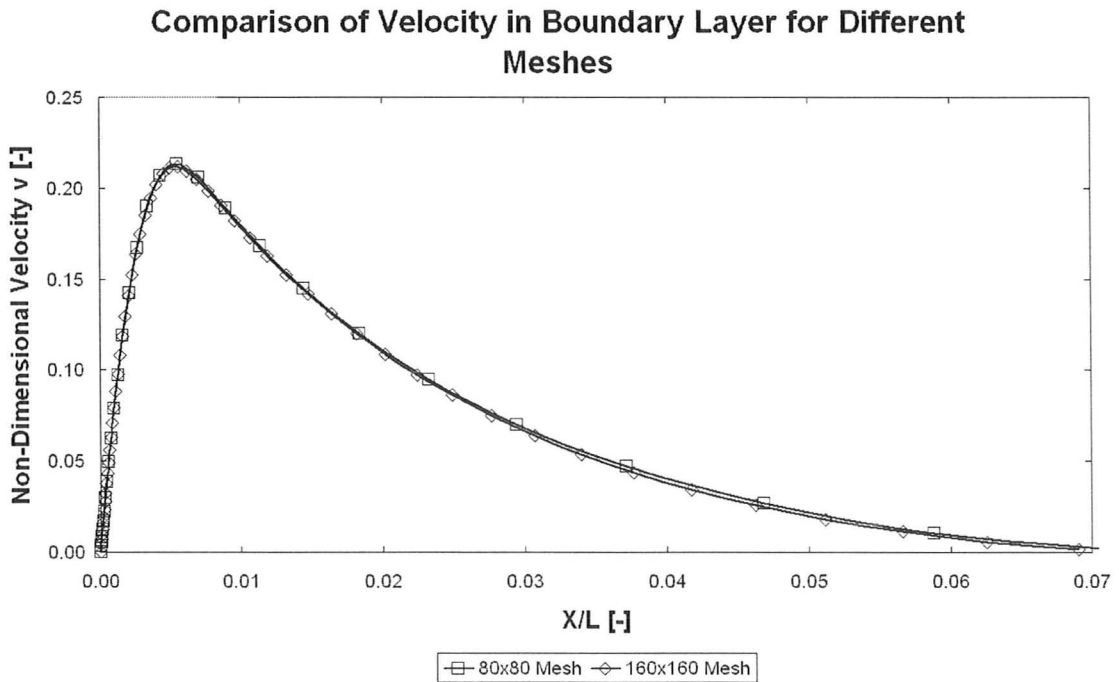


Figure 3.12 Velocity Profile in Boundary Layer Used to Show Grid Independent Results

Figure 3.12 shows nearly identical profiles. Figure 3.13 contrasts the temperature profile within the boundary layer for the two meshes.

Comparison of Temperature in Boundary Layer for Different Meshes

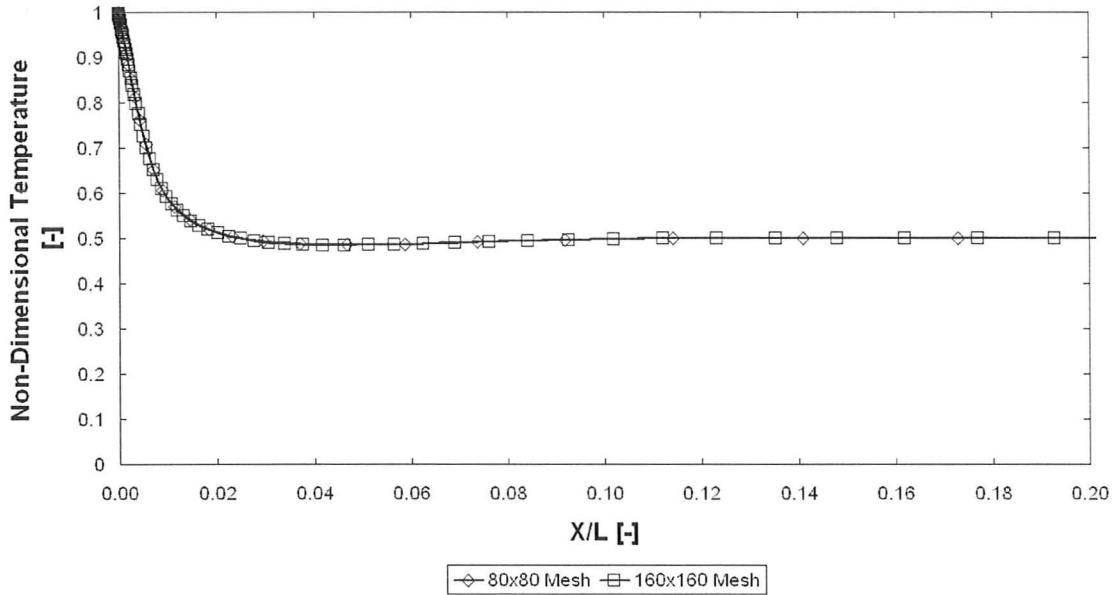


Figure 3.13 Temperature Profile in Boundary Layer Used to Show Grid Independent Results

Figures 3.12 & 3.13 show no significant change in results when the number of nodes in the mesh was quadrupled. Also, the average Nusselt number showed a change of 0.8%, which is smaller than the percentage error when compared to the experimental data.

Comparison of Turbulence Models

The $k-\omega$ model produced the best results for the velocity profile. Figure 3.14 shows an enlarged section near the hot wall for each of the standard models, showing the boundary layer of the velocity profile in greater detail.

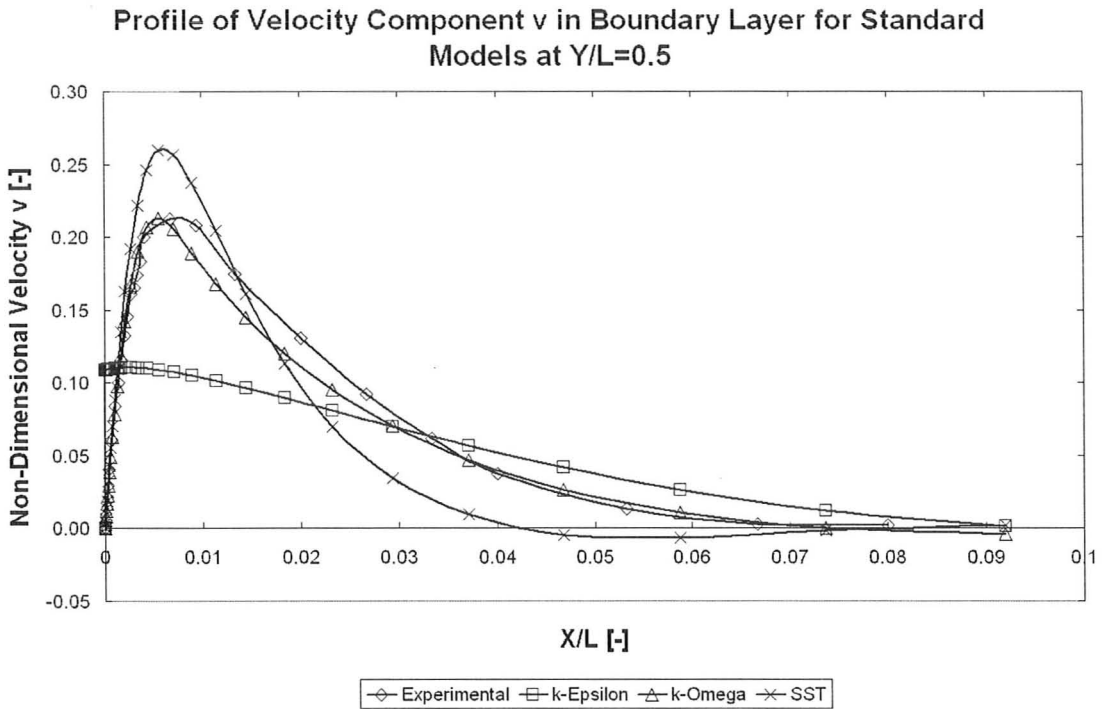


Figure 3.14 Velocity Profile in Boundary Layer by Hot Wall for Standard Models

The magnitude of the velocity peak for the $k-\omega$ model was closest to the experimental results. The boundary layer next to the hot wall over predicts the velocity peak magnitude with an error of 2.8 %, based on the experimental peak velocity. The SST model over predicted the magnitude of the velocity peak next to the hot wall, with an error of 21.6%. The $k-\omega$ model also predicted the peak location closest to its experimental location. The SST model also produces a much thinner boundary layer than either the benchmark data or the $k-\omega$ model. As discussed previously the experimental results are not symmetric. When compared to the boundary layer next to the cold wall the error for the $k-\omega$ model is similar but under predicts the peak velocity magnitude by 3.2%. This is still smaller than any other error for velocity peak magnitude. The error in the SST model prediction decreases from 21.6% to 14.6%. Therefore, while the $k-$

ω model averages the velocity peaks of the two walls and the SST model does better adjacent to the cold wall than the hot wall, the $k-\omega$ model still provides more accurate results in both locations. The $k-\varepsilon$ model prediction of the boundary layer is the worst of the three models. It fails to predict a well-defined peak and the magnitude of the velocity in the boundary layer is significantly less than the experimental data. The error in the peak velocity ranges from 48.4% to 50.9%. The SST model has the lowest average error in predicting the average Nusselt number with a value of 17.5%. The $k-\omega$ model has a slightly higher average error at 24.0%. However, most of the error in the $k-\omega$ model comes from the horizontal surfaces. The predictions for the hot and cold walls is more accurate than the SST model. This trend also is shown in the simulations, which used buoyancy turbulence production models, suggesting that it may be a general feature of the model. The $k-\varepsilon$ model is the worst predictor of average Nusselt number with an average error of 60.1%. The reason for $k-\varepsilon$ poor performance has to do with the wall treatment. Unlike the $k-\omega$ and SST model the $k-\varepsilon$ model uses a wall function rather than a low Re model near the wall.

Effect of Buoyancy Turbulence Production Model

As mentioned in the Models & Theory section, ANSYS CFX offers the option of an additional production term for two equation models. Cases 2A to 2F apply these production terms with each of the two equation turbulence models used in the standard simulations. Figure 3.15 shows the comparison of the boundary layers for the $k-\varepsilon$ model with the buoyancy turbulence production term.

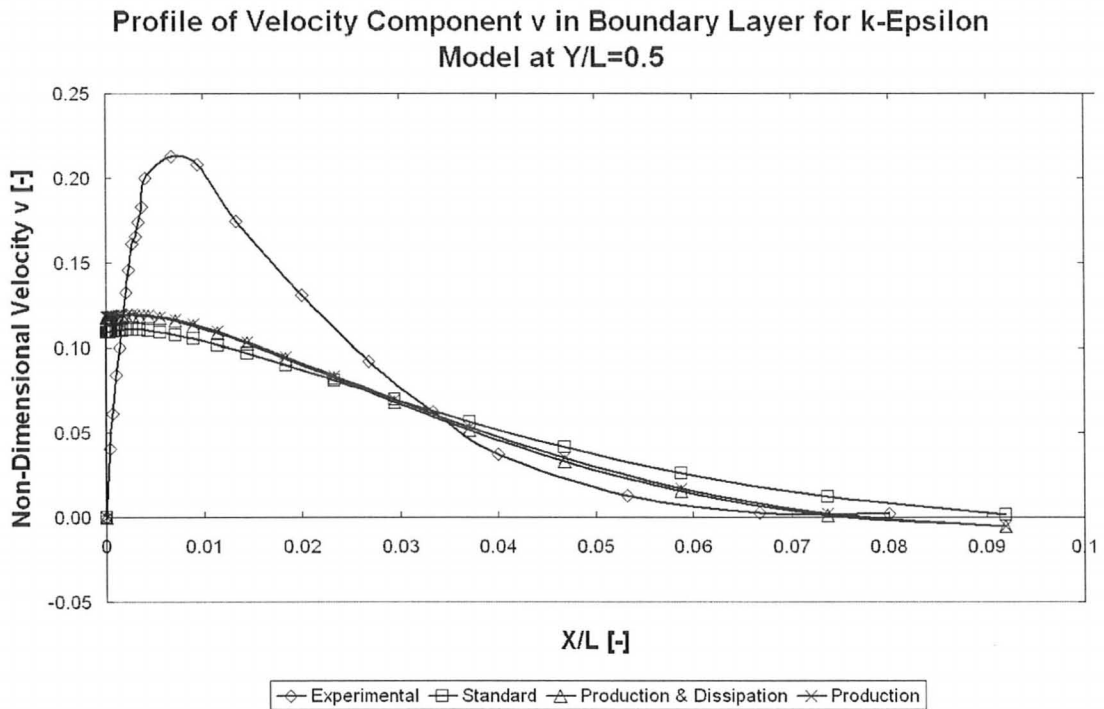


Figure 3.15 Velocity Profile in Boundary Layer for k- ϵ Model with Varying Levels of Buoyancy Turbulence Production.

For the k- ϵ model the inclusion of the buoyancy turbulence production model does not make a significant improvement in the results. The error in peak velocity magnitude does decrease by approximately 4%, however, the error is still significantly larger than the other simulations. The average error in the average Nusselt number increases with the use of the buoyancy turbulence production model, rising from 60.1% to 63.8% for the production simulation and 63.0% for the production and dissipation simulation. Therefore, the k- ϵ model only gains a minor benefit from the buoyancy turbulence production model and suffers a modest reduction in thermal accuracy. Furthermore, the k- ϵ model has negligible differences in results between the production and production and dissipation simulations. Figure 3.16 shows an enlarged comparison

of the velocity profile within the boundary layer adjacent to the hot wall for the $k-\omega$ model.

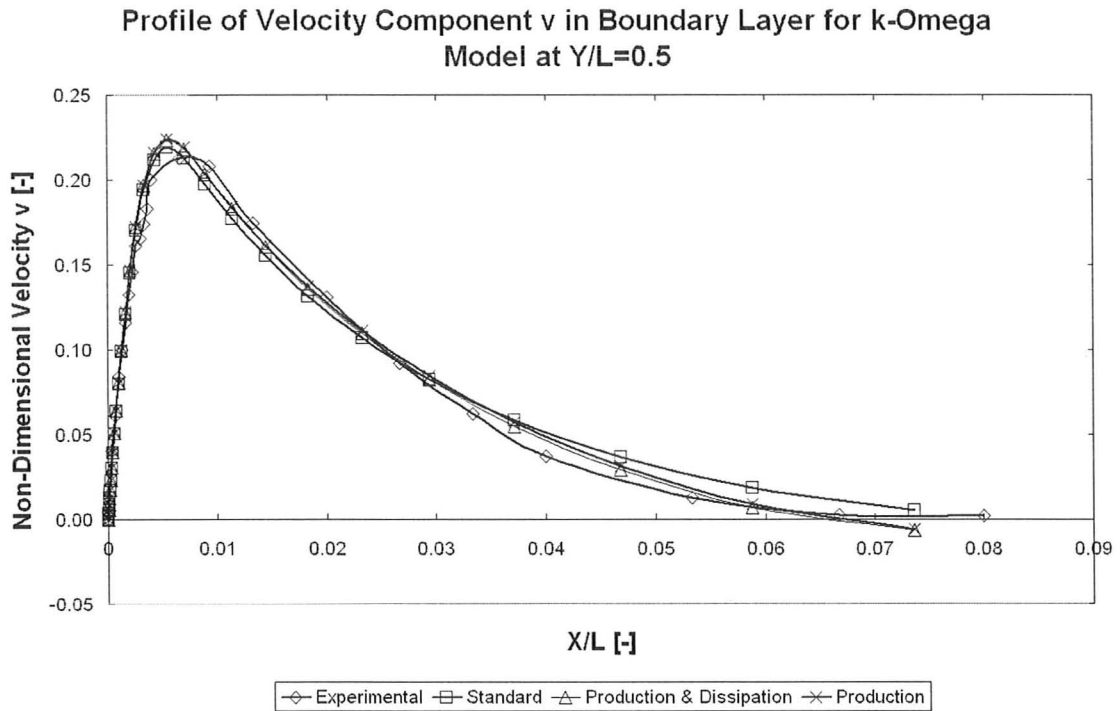


Figure 3.16 Velocity Profile in Boundary Layer for $k-\omega$ Model with Varying Levels of Buoyancy Turbulence Production.

The figure clearly shows that the simulations using the buoyancy turbulence production term have a minimal difference in peak velocity and boundary layer thickness with the standard $k-\omega$ simulation or the experimental data. Adjacent to the hot wall the error in velocity peak magnitude increased to 5.2% from 2.8%, however, adjacent to the cold wall the error decreased to 0.8% from 3.2%. The velocity profile for the production and dissipation simulation is identical to that of the production simulation. There is an improvement in the prediction of the average Nusselt numbers of the simulations with the buoyancy turbulence production terms. The average error was reduced from 24.0% to

17.6% for the production simulation and 18.2% for the production and dissipation simulation. Nonetheless both of the simulations which used the buoyancy turbulence production term produced similar results.

The results are opposite for the SST model. Figure 3.17 shows the same information when the same comparison is made for the SST turbulence model.

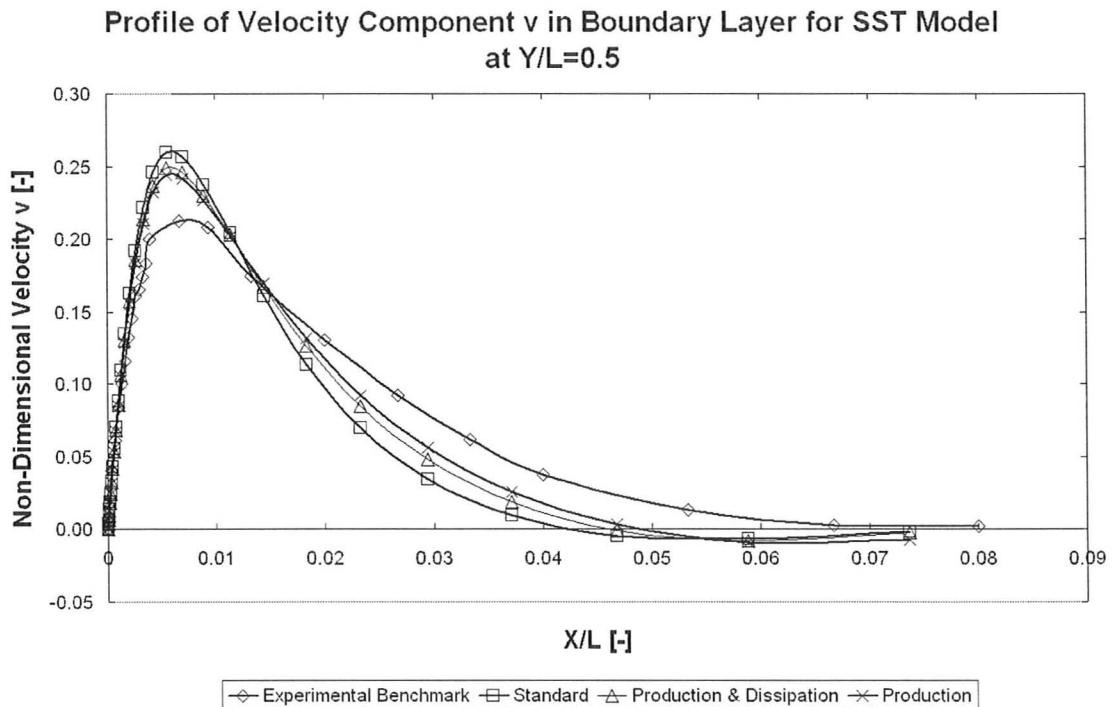


Figure 3.17 Velocity Profile in Boundary Layer for SST Model with Varying Levels of Buoyancy Turbulence Production.

Figure 3.17 shows less difference between the standard simulations and the buoyancy turbulence production simulations, however, the buoyancy turbulence production simulations have a higher peak velocity. The velocity peak magnitude error decreases to 14.6% for the production simulation and to 17.0% for the production and dissipation simulation from 22.0% adjacent to the hot wall. Adjacent to the cold wall the error was reduced to 8.4% for the production simulation and to 10.6% for the production

and dissipation simulation from 14.6.0%. There is a slight improvement in the average Nusselt number, the average error decreasing to 13.7% for the production simulation and 14.6% for the production and dissipation simulation from 17.5%.

All the results demonstrated that the addition of the buoyancy turbulence production term in the second equation of the relevant model, as done in the production and dissipation simulations, had no significant effect on the results of the simulation. The reason for this is in how the production term is included in the second equation. The exact production term is the maximum value of either the equation or zero. Therefore, if the equation returns a negative value then there is no difference in the equations despite including the additional production term. It can be shown for these simulations that the production term is almost always less than zero. Figure 3.18 shows the temperature pattern for both the standard SST simulation and the production and dissipation SST simulation.

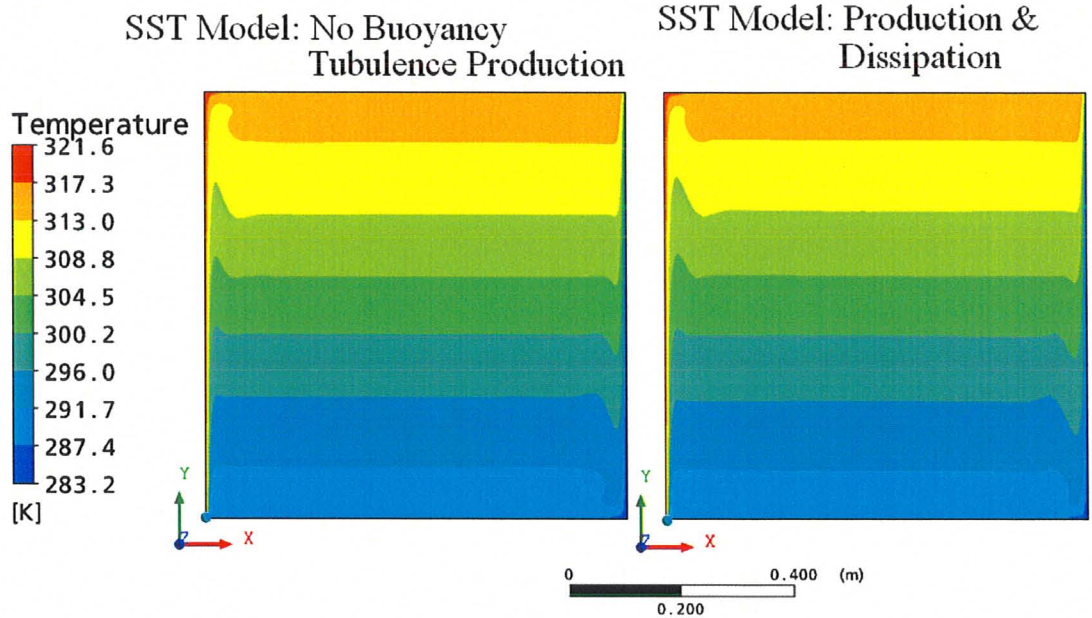


Figure 3.18 Isothermal Images of SST Models with Varying Levels of Buoyancy Turbulence Production.

It is clear that for most of the cavity the temperature rises with height which means that the partial derivative $\frac{\partial T}{\partial y} \geq 0$. The density will be positive as well. Figure 3.19, below shows that the value of the turbulence viscosity is also positive throughout the cavity for the standard SST simulation and the production and dissipation SST simulation.

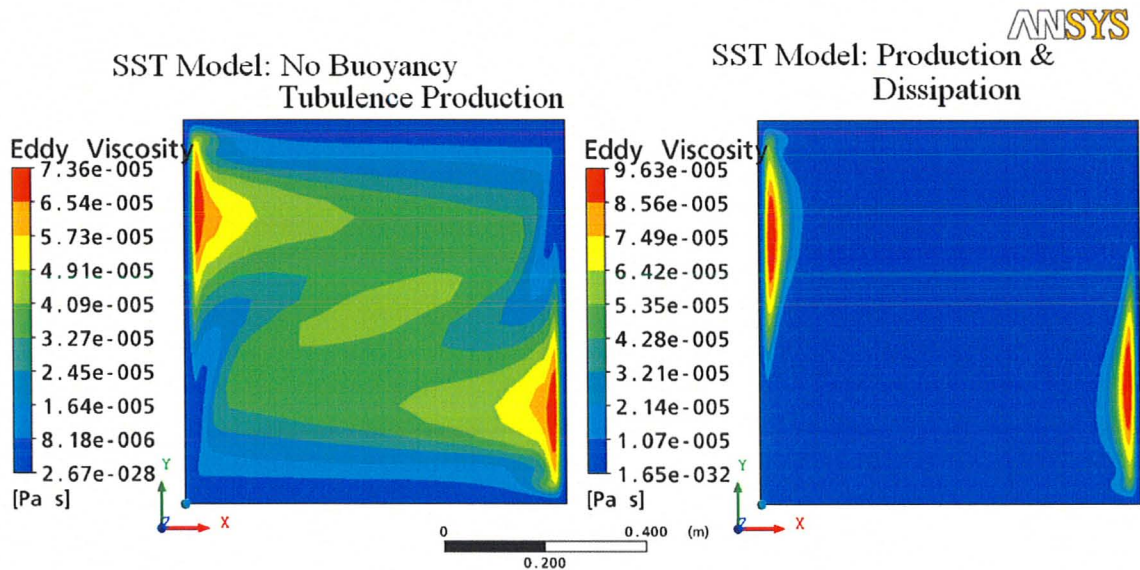


Figure 3.19 Eddy Viscosity in Domain of SST Simulations

If these terms are all positive values then the buoyancy turbulence production term will always be negative, as shown in equation 3.32.

$$-\frac{\mu_t \beta}{0.9 \rho} g \cdot \nabla T = -\frac{9.81 \beta \mu_t}{0.9 \rho} \frac{\partial T}{\partial y} \Rightarrow -\frac{9.81(+ve)(+ve)}{0.9(+ve)} (+ve) > 0 \quad (\text{Equation 3.32})$$

Therefore, the buoyancy turbulence production term in the second equation would always be zero and the production and dissipation simulation would be identical to the production simulation.

Conclusion:

The best model depends on the requirements of the simulation. The standard $k-\omega$ model generated the best velocity results; however, the SST model with buoyancy turbulence production generated the best average Nusselt numbers. The $k-\epsilon$ model performed the worst of all three models and did not significantly benefit from the use of the buoyancy turbulence production model. The $k-\omega$ showed an improvement in the

average Nusselt number but a loss of accuracy for velocity prediction with the use of buoyancy turbulence production. The use of the buoyancy turbulence production model improved the SST model but the velocity performance was still lower than the standard $k-\omega$ simulation. There was also no significant difference between the production simulations and the production and dissipation simulations with the values being within approximately 1% of each other.

3.3 Conclusion

ANSYS CFX was able to successfully model natural convection. For laminar flow the average Nusselt numbers were predicted with errors all less than one percent. The turbulent simulations produced larger errors; however, they are within an acceptable range. The turbulent results show a strong indication that the $k-\omega$ model was superior to the other models. It had the most accurate prediction of velocity profile in the boundary layer. At the level of turbulence considered, the buoyancy turbulence production models did not improve the results. The only exception to this was the prediction of average Nusselt, which favoured a production SST model. This may be a result of the low Rayleigh number of the cavity. It was also found that under-relaxation was necessary. There was no discernable pattern in the correct relaxation factor. It is concluded from the analysis that the best approach for simulating natural turbulent convection is with an under-relaxed $k-\omega$ model without the inclusion of a buoyancy turbulence production term.

Chapter 4: Radiation Heat Transfer Validation

4.1 Background

4.1.1 Radiation in Atria

Radiation heat transfer affects the temperature distribution in atria to a greater degree than in conventional buildings. The transparent nature of the outer surfaces means that radiation transfer through the glass becomes a significant aspect of both lighting conditions and heat exchange with the environment [Pfrommer et. al., 1995]. Wall [1997] found that that a highly glazed area can lose 10-70% of the solar radiation that enters, compared to conventional buildings which range from 0-5%. As such, it is important not only how much radiation enters the atrium but also how it interacts with the atrium interior to predict how much is reflected and emitted back to the environment. Complex geometry can result in light that has been reflected between façade elements several times before still entering or exiting the atria [Galasiu & Atif, 2002]. This means that simplifying the geometry can have significant effects on the final solution. Galasiu & Atif [2002] found that simplifying the roof geometry of an atria created errors of as much as 30% between their predicted and calculated results for light levels. Furthermore, accurate handling of the radiation is essential since the solar energy it provides is important in the stratification of the atrium and in providing the energy to create natural convection [Voeltzel et. al. 2001]. Therefore, errors in simulating radiation impact other aspects of the final solution.

4.1.2 Definitions

For the purposes of this section and all related discussion the variables and parameters are defined in Table 4.1

Symbol	Variable	Value/Units
A	Area	m ²
T	Temperature	K
Q	Heat Flow	W
q	Heat Flux	W/m
ε	Emissivity	[-]
θ_s	Solar Elevation	°
σ	Stephan Boltzman Constant	5.67e-8 W/m ² K ⁴

Table 4.1. Variable Definitions, Units and Values

4.1.3 Models & Theory

ANSYS CFX 11 has four radiation models; P1, Roseland, Discrete Transfer and Monte Carlo [ANSYS CFX, “Radiation Modeling”]. Of these the only two which are appropriate for use in an air filled cavity are the Discrete Transfer and Monte Carlo models. Both the P1 and Roseland radiation models were designed to be used in an optically thick environment [ANSYS CFX. “Comparison of the Radiation Models”]. For this reason only the Discrete Transfer and Monte Carlo Model were compared. The Monte Carlo model also is the only model that has the capability to use directional radiation boundary sources [ANSYS CFX, “Comparison of Radiation Models”, 2006]. These models are further explained in the following sections.

Radiation Model Boundary Conditions:

Both the Discrete Transfer radiation model and the Monte Carlo radiation model use the same boundary conditions. The boundary condition is shown as [ANSYS CFX, ‘Radiation Transport’, 2006]:

$$I_{\nu}(r_w, s) = \varepsilon_{\nu}(r_w)I_b(\nu, T) + \frac{\rho_w(r_w)}{\pi} \int I_{\nu}(r_w, s') |n \bullet s'| d\Omega' \quad (\text{Equation 4.1})$$

Where the radiation intensity at a given position (r_w), any given direction (s) and frequency (ν) is the intensity emitted by the boundary based on its temperature and emissivity ($\varepsilon_{\nu}(r_w)I_b(\nu, T)$) combined with the incident radiation on the surface multiplied by the boundary’s reflectivity ($\rho_w(r_w)$). The intensity emitted by the boundary is modeled as [Siegel & Howell, 1981]:

$$I_b = \frac{\sigma T^4}{\pi} \quad (\text{Equation 4.2})$$

Incident Radiation Calculations:

The primary difference between the Discrete Transfer radiation model and the Monte Carlo radiation model is in how they calculate the incident radiation. The Discrete Transfer model solves a simplified version of the radiation transport equation, which assumes that the radiation field is homogenous and that the scattering is isotropic, and is shown in equation 4.3 [ANSYS CFX, ‘Discrete Transfer Model’, 2006].

$$I_v(r, s) = I_{v0} \exp(-(K_{av} + K_{sv})s) + I_{bv}(1 - \exp(-K_a s)) + K_{sv} \bar{I}_v \quad (\text{Equation 4.3})$$

Where:

I_v = The radiation intensity felt by the boundary at the end of the ray.

I_{v0} = The radiation intensity leaving the boundary

K_{av} = Absorption Coefficient

K_{sv} = Scattering Coefficient

s = path length of ray

This equation is for a single frequency of radiation and must be integrated to find the total values. The Discrete Transfer model solves this equation for a discrete number of rays which connect to other surfaces and is therefore able to determine the incident radiation at the end of the rays. Figure 4.1 shows this concept.

Discrete Transfer Rays

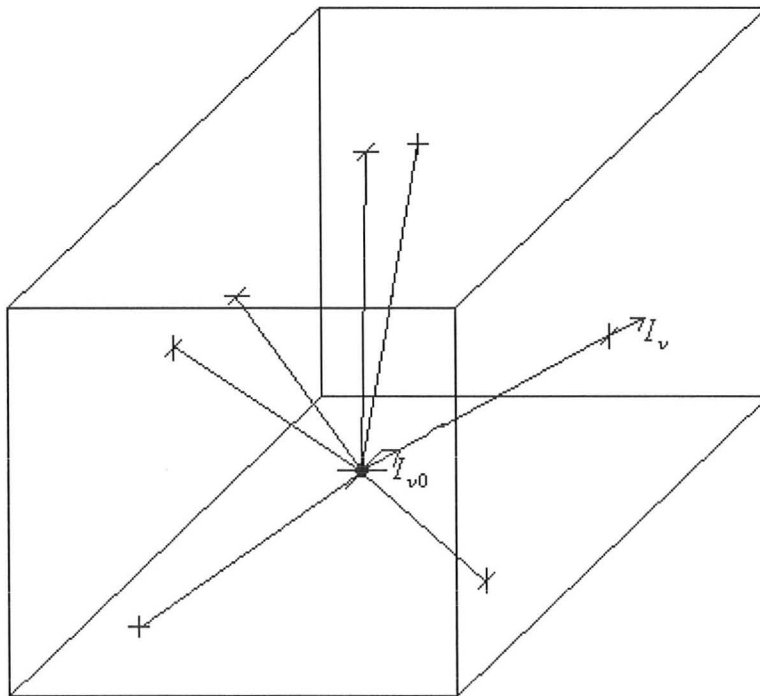


Figure 4.1 Discrete Transfer Rays

In transparent medium this equation becomes trivial because K_{av} and K_{sv} are zero and the equation can be simplified to equation 4.4.

$$I_v(r,s) = I_{v0} \quad (\text{Equation 4.4})$$

Iteration is used to reduce error from scattering and reflection. This process is dependent solely on the geometry of the simulation and is therefore only performed at the beginning of the simulation [ANSYS CFX, 'Comparison of the Radiation Models', 2006].

The Monte Carlo model works in a similar manner. The Monte Carlo model operates by following the paths of a large number of photons released from the boundary. The path of each photon is tracked, however, rather than each path ending when a boundary is reached the photon has a chance of either being absorbed by the boundary or reflected. Also, for each volume element that the ray passes through there is a chance that the photon will either be absorbed or scattered. The path of the particle continues until the photon become extinct [Siegal & Howell, 1981]. Unlike the Discrete Transfer model this process must be repeated throughout the simulation, this makes it more computationally expensive for gray radiation models [ANSYS CFX, 'Comparison of the Radiation Models', 2006]. Figure 4.2 shows some possible paths of photons.

Monte Carlo Photon Paths

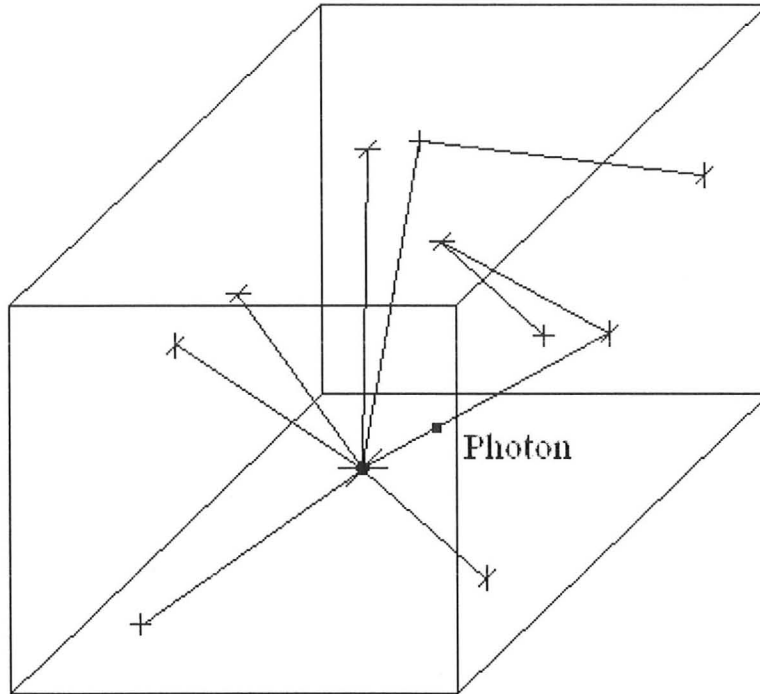


Figure 4.2 Monte Carlo Photon Paths

4.2 Simulations

4.2.1 Specified Heat Flux Simulations

Description:

A cubic cavity with one hot wall and five cool walls was simulated. The temperature of the cool walls and the average heat flux of the hot wall were specified in the simulation. The simulations were run in order to predict the temperature of the hot wall under those conditions. The geometry and boundary conditions are shown in Figure 4.3.

Measurement: Average temperature of the hot wall section: T_{Hot}

Validation:

For validation purposes the analytical solution for a two surface enclosure was used. The formula shown below assumes only two surfaces and that the hot surface can not see itself and therefore its view factor is one with respect to the other surface [Incorpera & DeWitt, 2002, eq.13.4].

$$q_{hot} = \frac{A_{hot} \epsilon_{hot} \sigma (T_{hot}^4 - T_{cool}^4)}{\frac{\epsilon_{hot} A_{hot}}{\epsilon_{cool} A_{cool}} (1 - \epsilon_{cool}) + 1} \quad (\text{Equation 4.5})$$

If both surfaces are black then both emissivities are equal to one, the denominator reduces to one and the equation simply becomes:

$$q_{hot} = A_{hot} \sigma (T_{hot}^4 - T_{cool}^4) \quad (\text{Equation 4.6})$$

Variations:

This simulation was run using both the Discrete Transfer model and the Monte Carlo model. Table 4.2 shows the parameters for each simulation presented here.

Simulation	T_{Cool}	Q_{Hot}	ϵ_{Cool}	ϵ_{Hot}	Analytical T_{Hot}	Radiation Model
1A	300K	1000 W	1	1	400.5K	Monte Carlo
1B	300K	1000W	1	1	400.5K	Discrete Transfer

Table 4.2 Parameters for Specified Heat Flux Simulations

Domain:

The domain was a cubic cavity with one-meter sides filled with a non-conductive fluid, which was transparent to the radiation. Figure 4.3 shows the division of the walls into the two sections as discussed in the description of the simulation.

Cube for Heat Flux Simulations

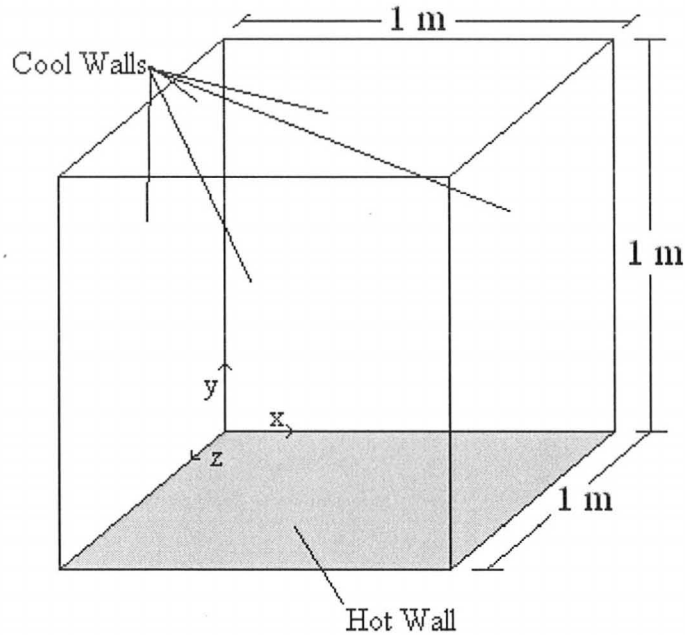


Figure 4.3 Domain for Specified Heat Flux Simulations

Boundary Conditions:

Hot Wall: The hot wall is a no slip wall with a specified heat flux of Q_{Hot} and an emissivity of ε_{Hot}

Cool Walls: The cool walls are no slip walls with a specified temperature of T_{Cool} and an emissivity of ε_{Cool}

Mesh:

Each simulation was run with a series of three-dimensional uniform meshes. The coarsest mesh had five nodes per side of the cube and the number of nodes per side of the cube was doubled for each level of refinement. The finest mesh had eighty nodes per side of the cube.

Results:

The results depend on whether the conservative or the hybrid temperature is used to calculate the temperature of the hot wall. Appendix C goes into further details of the difference between the two variables. The ANSYS documentation suggests that for calculation purposes that the conservative variables produce a more accurate reflection of reality [ANSYS CFX, “Hybrid and Conservative Variables” 2006]. The results of the simulations would suggest the same. Figure 4.4 plots the average conservative temperature of the hot wall predicted by the Discrete Transfer model, the Monte Carlo model and the analytical solution versus the number of nodes in the mesh per side of the cube.

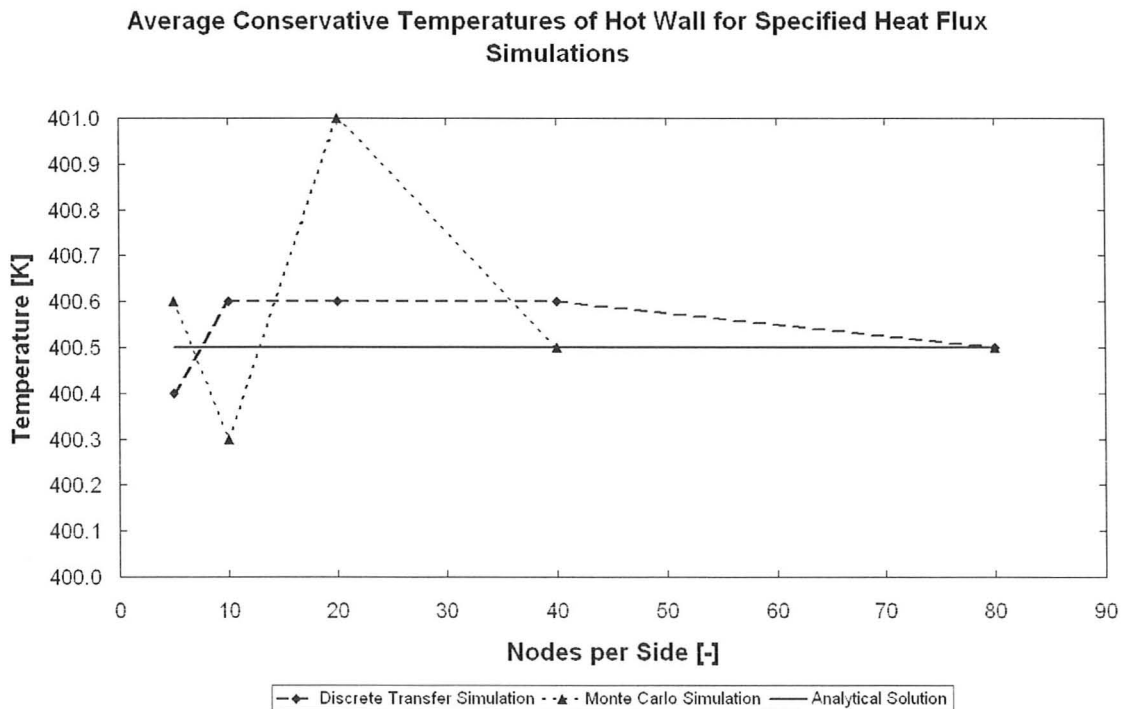


Figure 4.4 Average Conservative Temperatures for Different Radiation Models with a Specified Heat Flux Boundary Condition

Both models predict the hot wall temperature within half of a degree, even at the coarsest meshes. Figure 4.5 shows the average hybrid temperature of the hot wall, as predicted by the radiation models and the analytical solution versus the number of nodes in the mesh per side of the cube.

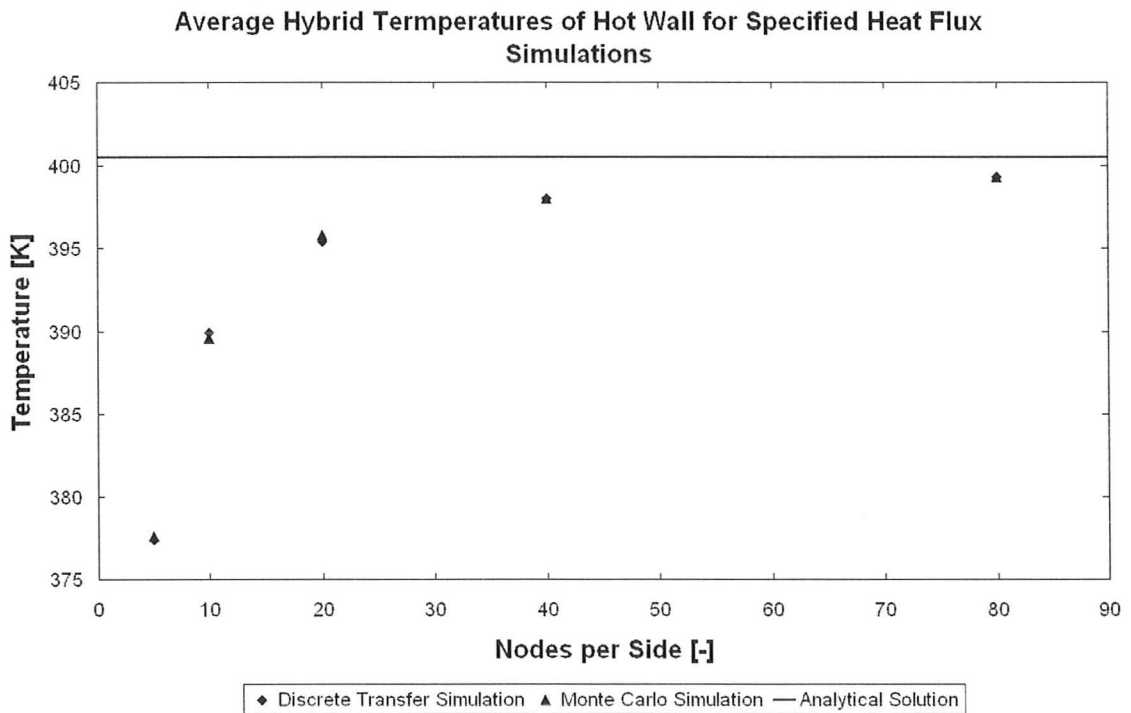


Figure 4.5 Average Hybrid Temperatures for Different Radiation Models with a Specified Heat Flux Boundary Condition

Both the Discrete Transfer and Monte Carlo models predict the temperature within 1.2 K of the analytical solution at the finest mesh.

Discussion:

Hybrid vs. Conservative Variables

The conservative temperatures are significantly more accurate than the hybrid temperatures. Using the coarsest mesh, the conservative values predict a temperature within 0.1 K of the analytical solution. With the finest mesh, the hybrid temperature does not reach grid independence and has an error of 1.2 K. Therefore, with a mesh four times as fine, the simulation's hybrid temperature has an error twelve times the magnitude of the conservative temperature.

The reason for the difference between the hybrid and conservative average temperatures is evident from a comparison of the temperature distribution between two temperatures. Figure 4.6 shows this comparison for simulations using the Discrete Transfer radiation model with a mesh with ten nodes per side of the cube. 

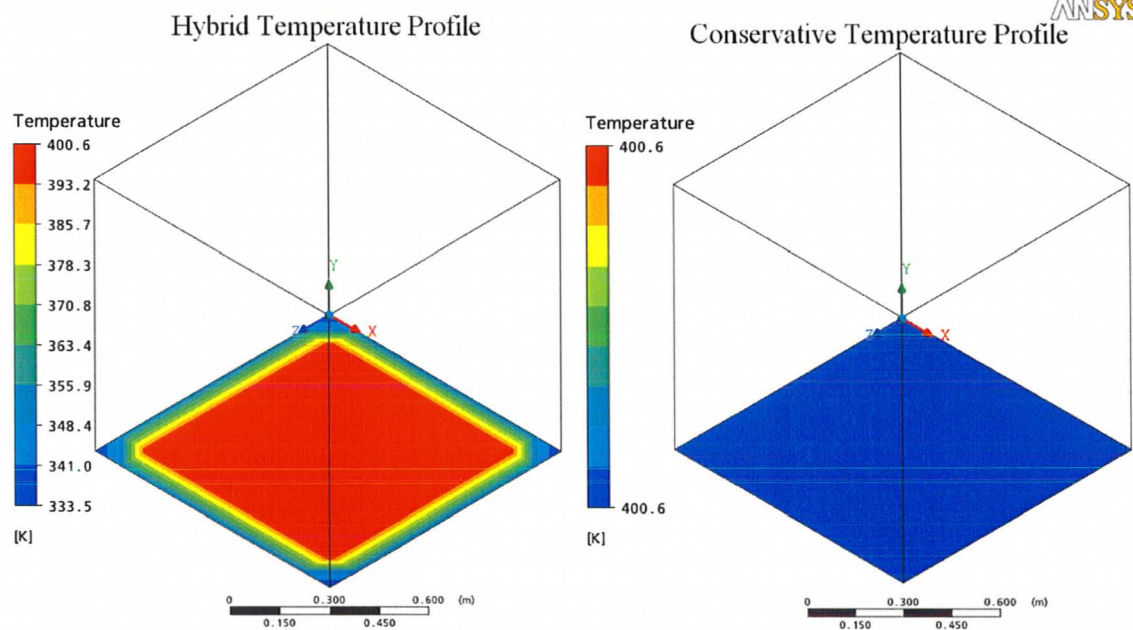


Figure 4.6 Temperature Distribution Comparison Between Hybrid and Conservative Values

The conservative temperature is uniform across the hot wall and within a tenth of a degree of the analytical solution. The hybrid temperature has the same distribution and magnitude as the conservative temperature until it reaches the edges of the hot wall. As the number of nodes increases, the error caused by the hybrid temperatures decreases. Figure 4.7, which plots the hybrid temperature along the hot wall for two different meshes for simulations using the Discrete Transfer model, shows the area affected is reduced as the number of nodes increases.

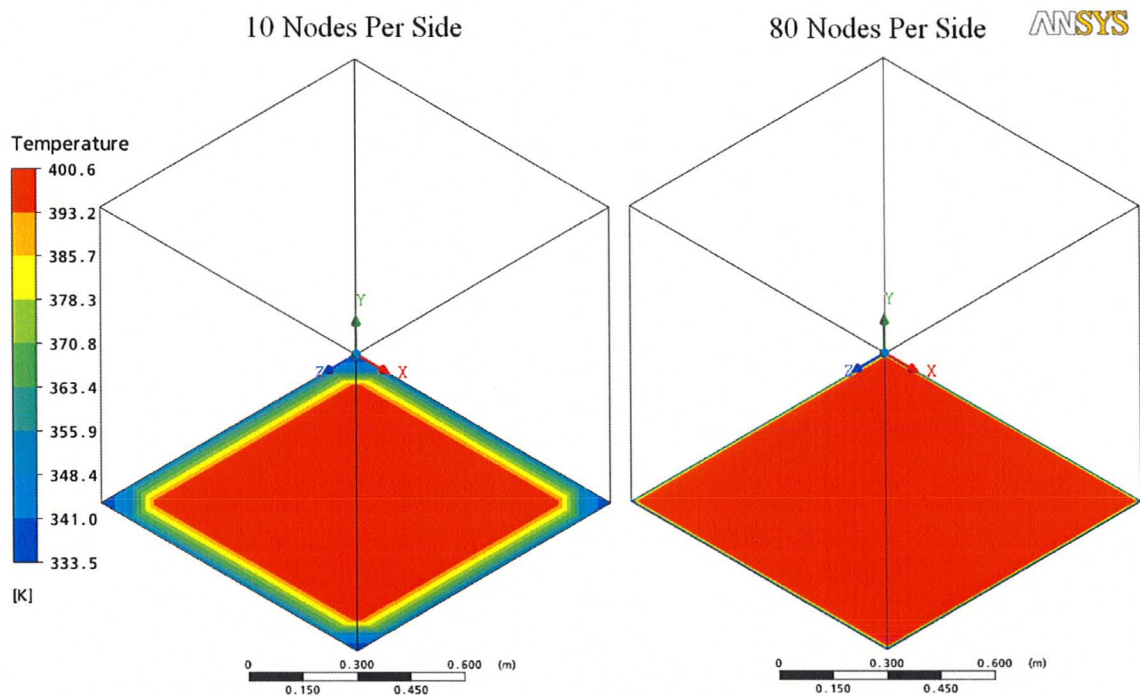


Figure 4.7. Temperature Distribution of Hot Wall Boundary for Different Mesh Refinements

Therefore, as the mesh is refined the area that is not at a constant temperature is much smaller and this is reflected in the increased accuracy of the eighty nodes per side mesh shown in Figure 4.5.

Comparison of Radiation Models

The Monte Carlo and Discrete Transfer radiation models produce similar average temperatures, however, the distribution is significantly different. Figure 4.8 shows the temperature distribution along the hot wall for a simulation using the Monte Carlo radiation model.

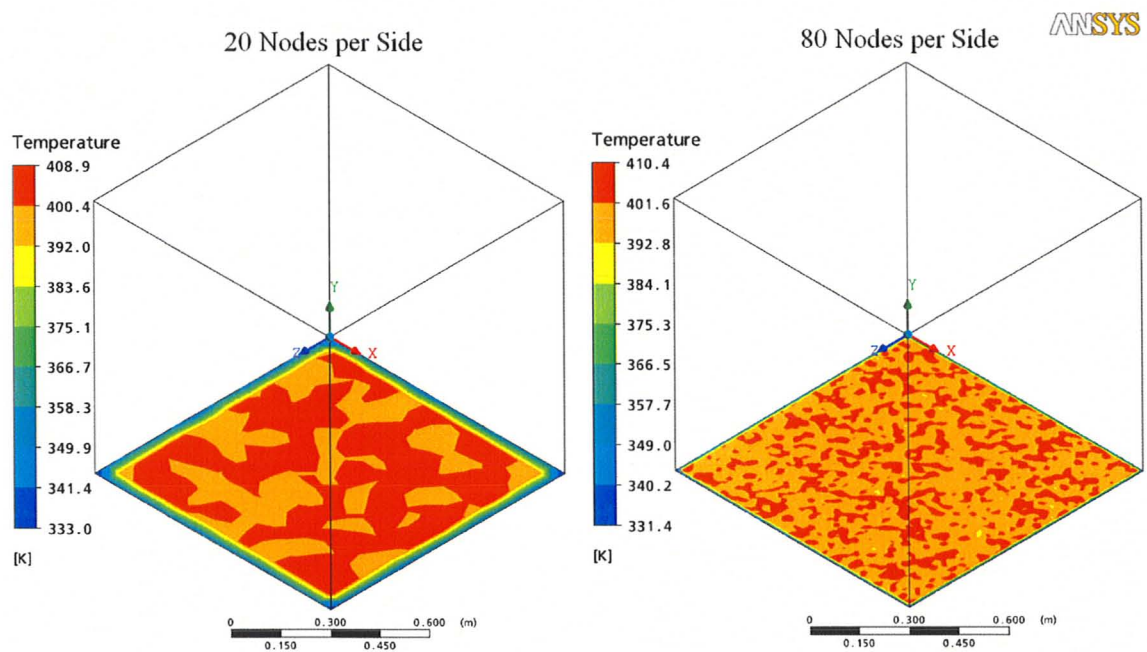


Figure. 4.8 Temperature Distribution Along Hot Wall of Monte Carlo Model

When compared to Figures 4.6 & 4.7, which used the Discrete Transfer model the temperature is not as uniform. The average temperature is comparable to the Discrete Transfer model, as is shown by Figures 4.4 & 4.5, however, the specific temperatures are less accurate. The temperature distribution is varied across the hot wall with a difference of at least eight degrees and up to seventeen degrees depending on the grid. The size of the areas of variations decreases as the number of nodes increases but the temperature

range of the variations increases. This means that across very small areas the simulation predicts dramatic variations in temperature.

Conclusions:

The conservative temperature produces better results than the hybrid temperature. The predicted conservative temperatures were within a tenth of a degree of the analytical solution, even at the coarsest mesh. The average hybrid temperatures shown in Figure 4.3 did not have the same level of accuracy, therefore, conservative values are a better measurement to use when evaluating the temperature of a boundary.

The Discrete Transfer model is preferable to the Monte Carlo model for these simulations. It produced a smoother temperature distribution that did not have sudden rises and falls in temperature over the surface.

4.2.2 Specified Temperature Simulations

Description:

A cubic cavity was used. The walls were divided into two sections: the hot wall and the cool walls. The temperature of each section was defined in the simulation and the convective heat transfer was disabled as in the previous section, and as discussed in Appendix D. This was done to determine if ANSYS CFX was capable of predicting the correct radiation heat flux.

Measurement: Total wall radiative heat flux from the hot wall: Q_{RW}

Validation:

The equations for a two surface enclosure were used from the previous specific heat flux simulation, rearranged so that the heat flux was solved for rather than the temperature of the hot wall.

Variations:

These simulations were run using different ranges between the hot and cool wall temperatures as well as different hot wall temperatures. They were also run using both the Discrete Transfer model and the Monte Carlo model. The walls were treated as a black body, therefore the sections' emissivities were as follows: $\epsilon_{Hot} = 1$ and $\epsilon_{Cool} = 1$.

Table 4.3 shows the parameters for each simulation presented here.

Simulation	Hot Wall Temp. (T_{Hot})	Cool Wall Temp. (T_{Cool})	Expected Heat Flow	Mesh	Radiation Model
2Ai	350 K	300 K	391.6W	Uniform	Discrete Transfer
2Aii	350 K	300 K	391.6W	Uniform	Monte Carlo
2Bi	350 K	325 K	218.3W	Uniform	Discrete Transfer
2Ci	300 K	250 K	237.8W	Uniform	Discrete Transfer
2Cii	300 K	250 K	237.8W	Expanding	Discrete Transfer

Table 4.3 Parameters for Specified Temperature Simulations

Domain:

The domain used was identical to the one used in the Specified Heat Flux simulations.

Boundary Conditions:

Hot Wall: The hot wall is a no slip wall with a specified temperature of T_{Hot} and an emissivity of ϵ_{Hot}

Cool Walls: The cool walls are no slip walls with a specified temperature of T_{Cool} and an emissivity of ϵ_{Cool}

Mesh:

Each simulation was run with a series of three-dimensional uniform meshes. The coarsest mesh had five nodes per side of the cube. The number of nodes per side of the cube was doubled at each level of refinement. The finest mesh had eighty nodes per side of the cube. In addition, a simulation was run with two expanding meshes. The expanding meshes were used in order to create meshes with the same initial grid spacing of 1 mm but with a different number of nodes. The reason for this is discussed further in the discussion section.

Results:

Table 4.4 shows the results for all of the simulations with uniform meshes, including the total wall radiative heat flow from the hot wall and the percentage error.

	Total Heat Flux & % Error for Discrete Transfer (DT) & Monte Carlo (MC)							
	DT (300K-350K)		DT (325K-350K)		DT (250K-300K)		MC (300K-350K)	
Nodes Per Side	Heat Flow	% Error	Heat Flow	% Error	Heat Flow	% Error	Heat Flow	% Error
5	266.9	31.85%	148.8	31.83%	162.1	31.83%	269.3	31.23%
10	333.5	14.84%	185.9	14.84%	202.5	14.85%	336.1	14.17%
20	362.8	7.36%	202.2	7.37%	220.3	7.36%	366.2	6.49%
40	376.8	3.78%	210.0	3.80%	228.8	3.79%	381.8	2.50%
80	384.3	1.87%	214.2	1.87%	233.4	1.85%	388.9	0.69%
Extrapolated	393.3	0.43%	219.1	0.37%	238.8	0.42%	394.8	0.82%

Table 4.4 Results for All Specified Temperature Simulations with Uniform Meshes

Included are the heat fluxes calculated using the extrapolation detailed in Appendix B. The percentage errors are calculated relative to the analytically calculated total heat flux. Table 4.5 shows the results for simulation 2C, and compares the percentage error of the two types of meshes.

Nodes Per Side	Uniform Mesh		Expanding Mesh	
	Heat Flux	% Error	Heat Flux	% Error
5	162.1	31.83%		
10	202.5	14.85%		
20	220.3	7.36%		
40	228.8	3.79%	237.7	0.04%
80	233.4	1.85%	237.5	0.13%
Extrapolated	238.8	0.42%		

Table 4.5 Results for Simulation 2C with a 50 K Temperature Difference with Different Meshes

Wall radiative heat flux does not have hybrid and conservative values since it only occurs along the surface of a domain.

Discussion:

Relationship between Error and Mesh

The error is nearly entirely due to the grid size of the mesh. In all three simulations using the Discrete Transfer model and uniform meshes the percentage error is strongly linked to the number of nodes per side. Figure 4.9 shows this trend clearly.

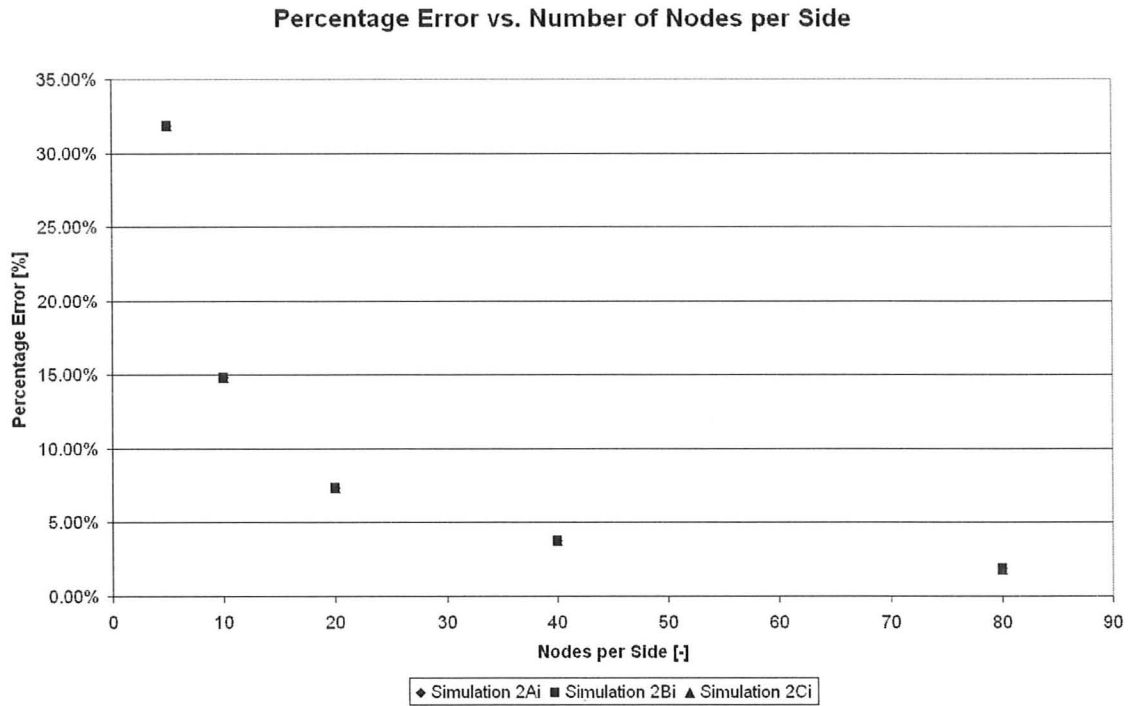


Figure 4.9 Percentage Error Based vs. Nodes per Side of Mesh

There is evidence that the most important grid spaces are those adjacent to the wall. Figure 4.10 shows the wall radiative heat flux for simulation 2Ci along half of the centerline for all of the uniform meshes.

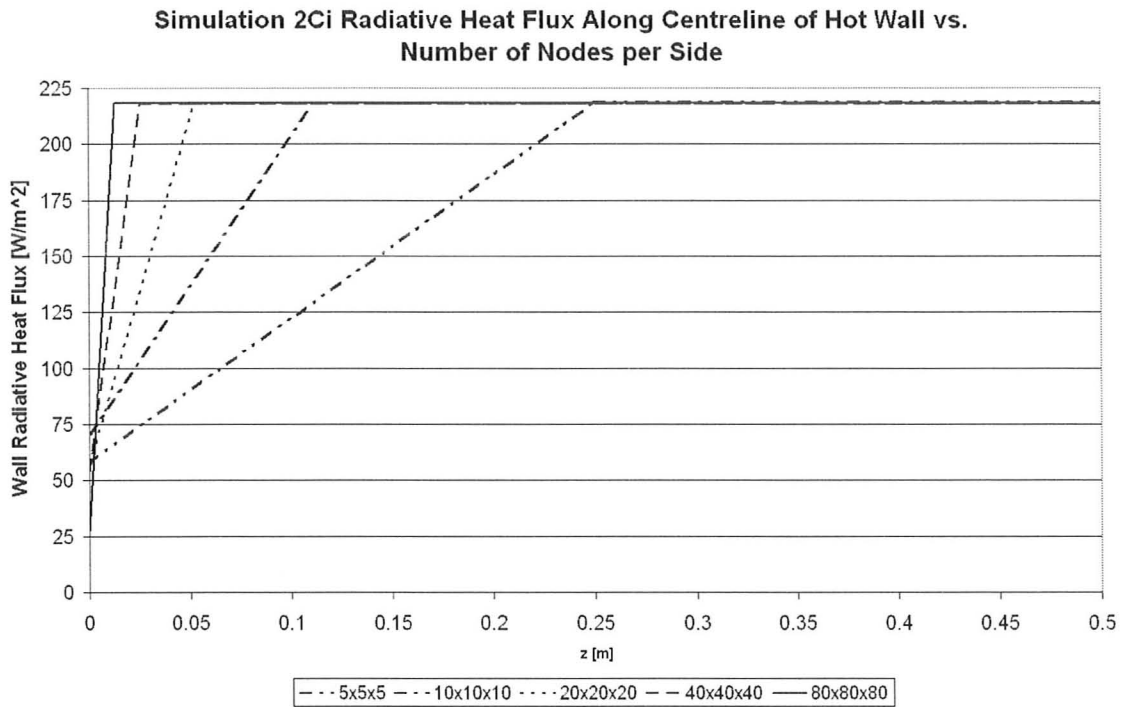


Figure 4.10 Heat Flux Along the Centerline for Discrete Transfer Radiation Model Simulation with a 50 K Temperature Difference and Uniform Meshes

For each mesh the heat flux remains constant until the node adjacent to the wall at $z=0$. Table 4.6 shows the magnitude of the flat areas of the curve and their relationship to the correct heat flux.

25K Temperature Difference Simulation 2Bi		
Nodes Per Side	Peak Heat Flux	% Error
5	218.8	0.23%
10	217.9	0.18%
20	217.9	0.18%
40	218.1	0.09%
80	218.3	0.01%

Table 4.6 Peak Heat Fluxes for Discrete Transfer Simulation

The peaks are all very accurate and show little variation, as the mesh becomes finer. The initial node along the wall however, has a lower value, which is between the heat flux along the cold wall and the heat flux along the hot wall. ANSYS CFX-Post joins this node with the node nearest the wall with a linear interpolation. Therefore, most of the error is produced when CFX-Post integrates over this area between the nodes and produces an incorrect solution. To explore this further simulation 2Cii was used to examine meshes with different number of nodes but the same initial grid spacing. Table 3.5 for simulation 2Cii showed that even when the number of nodes was doubled along a side that the heat flux was virtually identical with only a 0.08% change in predicted heat flux. This simulation had the smallest grid spacing from the wall to the initial node and provided a higher degree of accuracy than any of the uniform grid simulations or their extrapolated values.

Conclusions:

When predicting heat fluxes the more accurate conservation values are not available, therefore, the hybrid variables must be dealt with. Since the errors are mesh related then the simplest method is to reduce the initial grid spacing in the region where two walls meet so that the error is minimized. For the atrium simulation since the initial grid space must be small in order to satisfy the turbulence equations requirements the error should be minimized in heat flux predictions.

4.2.3 Solar Radiation Simulations

Description:

A cubic cavity was used with the walls divided into three sections: the floor, the walls and the opening. The cavity was filled with a non-conductive fluid that is transparent to radiation. The opening was included to allow sunlight to be modeled by admitting directed radiation into the cube.

Measurement:

The average floor temperatures, T_{1A} and T_{1B} , and the average wall temperature, T_3 . The average floor temperatures were calculated by averaging the temperatures along the centerline of each section of floor.

Validation:

The analytical solution for the wall and floor temperatures was used to solve for the temperatures. The floor was subdivided into two sections: section A, the sunlit portion of the floor and section B the unlit portion of the floor. The solution consisted of the three-equation system derived from the energy equation for each surface, which was solved by iteration. This process is explained in further detail in Appendix E.

Domain:

The domain is a cubic cavity with a side length of one meter. The cavity is filled with a non-conducting fluid, which is transparent to radiation. The boundary of the domain is divided into four sections; Floor Section A, Floor Section B, Walls and the

Opening. The opening admits solar radiation that strikes Floor Section A. Figure 4.11 below shows the domain and its measurements.

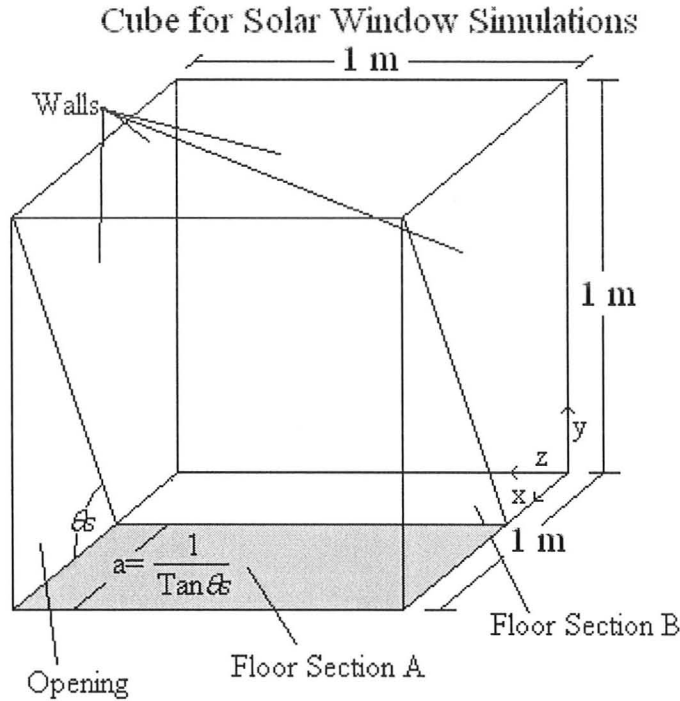


Figure 4.11 Domain for Solar Radiation Simulation

Boundary Conditions:

Opening: The opening was an opening boundary condition with the velocity set to zero and a specified uniform temperature of 303.15 K. The simulations that used the Monte Carlo model had a directional radiation boundary source. The angle of which was set to the appropriate θ_s for the simulation.

Floor: The floor was a stationary no slip wall. The boundary had a specified heat flux boundary condition. For the simulations using the Monte Carlo radiation model the heat flux was set to zero so the boundary was adiabatic. The simulations using the Discrete Transfer radiation model used a heat flux of 1000 W/m^2 confined to Floor Section A.

The method of using a specified heat flux in this manner is discussed in Appendix D and limiting it to Floor Section A was accomplished using CEL code as discussed in Appendix F.

Walls: The walls were stationary no slip walls. The walls were given a heat transfer coefficient of $20 \text{ W/m}^2\text{K}$ and an ambient temperature of 303.15K .

Variations:

A variety of radiation angles or solar elevations were used. Both the Discrete Transfer model and the Monte Carlo model were used. Only the results from the Discrete Transfer simulations are shown. The Monte Carlo model simulations failed to converge and this behaviour is discussed in the discussion section. The walls were treated as a black body, therefore the sections' emissivities were equal to one. Table 4.7 shows the parameters for each simulation presented here

Simulation	Solar Elevation
3A	$\theta_s = 55^\circ$
3B	$\theta_s = 65^\circ$
3C	$\theta_s = 75^\circ$

Table 4.7 Parameters for Solar Radiation Simulations

Meshes:

Each simulation was run with a series of three-dimensional uniform meshes. The coarsest mesh had ten nodes per side of the cube. The number of nodes per side of the cube doubled with each level of refinement. The finest mesh had eighty nodes per side of the cube.

Results:

Tables 4.8-10 show the prediction of each temperature by the simulations and the percentage error using the analytical solution's maximum temperature difference in the cavity as a scale. The simulations which used Monte Carlo model failed to converge and are not shown here.

Solar Elevation is 55 Degrees						
# of Nodes	T _{1A}	% Error	T _{1B}	% Error	T ₃	% Error
10	403.4	0.89%	307.3	0.79%	308.9	0.95%
20	403.5	0.79%	307.1	0.99%	309.1	0.83%
40	403.6	0.69%	307.5	0.59%	309.1	0.77%
80	403.6	0.69%	307.7	0.40%	309.1	0.74%
Analytical	404.3		308.1		309.9	

Table 4.8 Results for Simulation 3A

Solar Elevation is 65 Degrees						
# of Nodes	T _{1A}	% Error	T _{1B}	% Error	T ₃	% Error
10	402.8	0.80%	305.2	1.39%	306.7	1.08%
20	402.9	0.70%	305.4	1.19%	306.9	0.85%
40	402.9	0.70%	305.5	1.10%	306.8	0.96%
80	402.9	0.70%	305.6	1.00%	306.9	0.91%
Analytical	403.6		306.6		307.8	

Table 4.9 Results for Simulation 3B

Solar Elevation is 75 Degrees						
# of Nodes	T _{1A}	% Error	T _{1B}	% Error	T ₃	% Error
10	402.2	0.80%	303.9	1.40%	304.8	1.24%
20	402.3	0.70%	304.2	1.10%	305.0	0.96%
40	402.3	0.70%	304.3	1.00%	305.0	1.01%
80	402.3	0.70%	304.3	1.00%	305.1	0.93%
Analytical	403.0		305.3		306.0	

Table 4.10 Results for Simulation 3C

Discussion:

Grid Independence

Simulations 3A, 3B and 3C showed grid independence. As the mesh was refined from forty to eighty nodes per side the predicted temperatures changed by a tenth of a degree or less. Tables 4.8-10 show this clearly.

Monte Carlo Results

The Monte Carlo model failed to converge in the solar cube simulations. The root mean squared residuals never reached lower than 1E-3 and produced unstable results. Various methods were attempted to create convergence including various time steps and the use of double precision accuracy in the numbers. The issue became significant enough that the aid of the ANSYS CFX technical assistance was requested. With the simulation data provided to them they could not get convergence lower than 1E-3 either [Email, cfx-support-can, July 13, 2007]. They made three recommendations; It was suggested that additional histories would help convergence, that a coarser mesh would be easier to converge and that a CCL code could be added to change the radiation under relaxation factor [Email, cfx-support-can, August 30, 2007]. The first and third solutions were attempted with insignificant progress [Email, cfx-support-ca, August 30, 2007]. The second with a coarser mesh was attempted but produced no better results. It should also be noted that in a practical application in an atrium a fine mesh would be required for convergence of the fluid field. This was seen in early meshes with the full atrium simulation, a mesh at least as fine as the one used by the Monte Carlo simulation would be necessary for convergence. This result was not particularly surprising since the Monte

Carlo model is “somewhat notorious for not being able to get good residuals”, and it was suggested that high residual would have to be accepted if the Monte Carlo model was used [Email, cfx-support-can, July 13, 2007]. Figure 4.12 compares the temperature along a wall simulated using the Monte Carlo model at different iterations during one of the solar cube simulations.

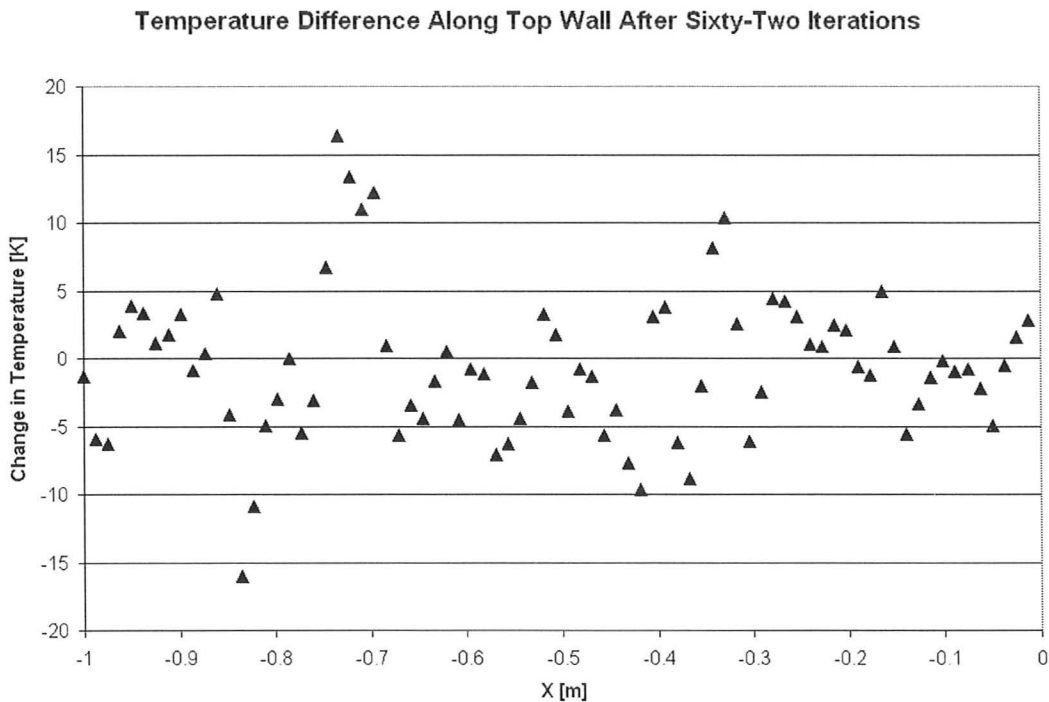


Figure 4.12 Temperature Difference Along Wall After Sixty Two Iterations

Clearly the simulation has not reached a steady solution since the temperatures at the nodes have fluctuated by as much as sixteen degrees, there is no discernible pattern to the change and it is not approaching a solution.

Conclusions:

The Monte Carlo model did not converge with the direct radiation boundary source and since the previous simulations have shown the Discrete Transfer model to be more suitable for a specified heat flux boundary condition, the Discrete Transfer model should be used where possible. Lastly, since the solution showed grid independence for all three temperatures and an error of less than one percent this method of modeling solar radiation can be successfully used in ANSYS CFX.

4.3 Conclusions

The Discrete Transfer radiation model was the superior model for these simulations. Conservative variables were shown to be significantly superior in predicting the correct boundary temperatures. Given that the boundary conditions for the atrium simulations will be a combination of heat fluxes and temperature boundary conditions, the conservative temperature would be the best type to use to judge temperature along the boundaries of the atrium. Although it should be mentioned that since the error in hybrid variables decreases with the initial grid spacing a sufficiently small initial grid space would reduce the errors below a magnitude of significance.

The directed solar radiation boundary conditions will have to be simulated using a heat flux located on the floor where the radiation would have struck. The Monte Carlo model does not converge with the directed radiation boundary source and the Discrete Transfer model does not possess the capability to add a directed radiation boundary

source. Therefore, the floor heat flux is the only method viable at this time for including the directed solar radiation.

Chapter 5: Conjugate Heat Transfer

5.1 Background

5.1.1 Importance of Conjugate Heat Transfer in Atria

Conjugate heat transfer is an important part of the thermal performance of atria. As discussed previously, one objective of good atria design is to limit the variation in temperature throughout the daily cycle. One way that this can be accomplished is through solar thermal storage. At its most basic, solar thermal storage uses mass to absorb the solar energy and store it as sensible heat. Then when the surrounding temperature decreases the energy is released from the mass to the surroundings. This mass could be a specific storage area, such as a tank of water or container of gravel, or built as part of the atrium, such as the floor or the walls [Bahador & Sayigh, 1979]. It essentially offers a double benefit of absorbing the excess energy during the day to keep internal temperatures lower and releasing it later, which keeps the internal temperature higher [Bahador & Sayigh, 1979]. These types of systems have been put into practice in numerous locations in a variety of countries. Canadian examples include The Ark, a greenhouse with 90 m³ of rock and 72,000 L of water for passive solar heating, and La Macaza House, located in Quebec with 32 m³ of rock for both active and passive heating [Lawand & Saulnier, 1979]. This type of system has been in use for centuries, including a 1300 A.D. structure; “Montezuma’s Castle that uses the thermal properties of the walls the keep the building warm during the winter [Bahador & Sayigh, 1979]. Passive thermal storage is therefore an established method and one that should be reasonable to consider for use in an atrium. Thus, it is essential that an atrium simulation be able to keep track

of the thermal interaction between the air and solids within the atrium so that system performance can be accurately predicted when they are included in the design.

5.1.2 Definitions

For the purposes of this chapter and all related discussion the variables and parameters are defined in Table 5.1

<i>Symbol</i>	Variable	Value	Units
A	Area		m ²
h	Coefficient of Heat Transfer		W/m ²
H	Height of Channel	0.0508 m	m
k	Thermal conductivity of heated section	47.9	W/mK
k_{ref}	Reference thermal conductivity	26.3	W/mK
$Pr = \frac{C_p \mu}{k}$	Prandtl Number	0.7	[-]
T	Temperature		°C
T_{amb}	Ambient Temperature	Unknown	K
q_{ref}	Heat Flux in Heated Section	12.7	W/m ²
x	Direction along length of channel		m
y	Direction along height of channel		m
$T_{ref} = \frac{q_{ref} H}{k_{ref}}$	Temperature across the channel is 1-D Stationary flow	25.3 K	K
$\theta = \frac{T - T_{Amb}}{T_{Ref}}$	Non Dimensional Temperature		[-]

Table 5.1 Variables and Non Dimensional Values

5.1.3 Models & Theory

Dimensionless Temperature Theta

The dimensionless temperature theta is defined as follows:

$$\theta = \frac{T - T_{Amb}}{T_{Ref}} \quad (\text{Equation 5.1})$$

T_{Ref} is the value of the temperature difference across the channel if it was purely conductive heat flow, i.e. the fluid was stationary.

Thermal Resistance Model

The convection heat transfer coefficients for the bottom and top of the channel were calculated using the thermal resistance model that replaces layers of material with an equivalent convection heat transfer coefficient and external temperature. It was used in this case to reduce the number of nodes in the mesh and therefore the computational requirements. What material was replaced will be discussed in greater detail in the relevant boundary condition sections. This section will limit itself to the theory and general application. The heat flux is treated as a current with the temperature difference being analogous to the voltage and the various substances and convective surfaces being analogous to resistances in an electrical circuit. Further information can be found in section 3.1.2 of Incropera & DeWitt's Fundamentals of Heat and Mass Transfer. The two types of resistances that apply to this section are a solid barrier of thickness L , an area A and a conductivity of k , and the convective heat loss of a surface with a coefficient of heat transfer h and an area of A . The following equations 5.2 and 5.3 show the equations for the types of resistances [Incropera & DeWitt, 2002].

$$R = \frac{L}{kA} \quad (\text{Equation 5.2})$$

$$R = \frac{1}{hA} \quad (\text{Equation 5.3})$$

Therefore, heat flux can be expressed as in equation 5.4, where T_1 and T_2 are the temperatures at either end of the section to be modeled as a resistance [Incropera & DeWitt, 2002].

$$Q = \frac{T_1 - T_2}{\sum R} \quad (\text{Equation 5.4})$$

For the simulations in this section this model will be used to replace several layers of insulation so that the boundary condition can use a coefficient of heat transfer. Figure 5.1 shows the configuration considered.

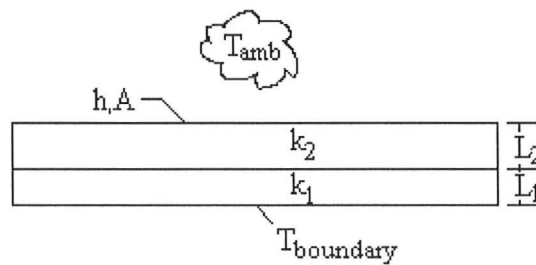


Figure 5.1 Area to be Modeled Using Thermal Resistance

Equations 5.5 and 5.6 show the process of manipulating the previous equations in order to develop an effective heat transfer coefficient for the layers of insulation.

$$Q = \frac{T_{amb} - T_{boundary}}{\sum R} = \frac{T_{amb} - T_{boundary}}{\frac{L_1}{k_1 A} + \frac{L_2}{k_2 A} + \frac{1}{hA}} = A \frac{T_{amb} - T_{boundary}}{\frac{L_1}{k_1} + \frac{L_2}{k_2} + \frac{1}{h}} \quad (\text{Equation 5.5})$$

$$\frac{Q}{A} = h(T_{amb} - T_{boundary}) = \frac{T_{amb} - T_{boundary}}{\frac{L_1}{k_1} + \frac{L_2}{k_2} + \frac{1}{h}} \Rightarrow h = \frac{1}{\frac{L_1}{k_1} + \frac{L_2}{k_2} + \frac{1}{h}} \quad (\text{Equation 5.6})$$

5.2 Simulations

5.2.1 Horizontal Channel with Aluminium Heated Section

Description:

This simulation is modeled as a two dimensional flow in a horizontal channel, which was heated from below. The heating was supplied to the bottom of an aluminium section by electric heaters. The air passed through the channel and over the heated aluminium section allowing for conjugate heat transfer. The top and bottom of the channel, that was not part of the aluminium plate, were moderately insulated.

Measurement:

The temperature was recorded by thermocouples in the heated section and in the air above the heated section. The temperature profiles at different heights are used to validate the accuracy of the simulations. The bottom temperatures are recorded at the surface of the bottom of the channel, or $y/H=0$. The middle temperatures are recorded at $y/H=0.5$ and the top temperatures are recorded at a height of $y/H=0.875$. Chiu, Richards and Jaluria [2001] reported an error in their thermocouples of 0.2 K and a repeatability error of 0.15 K, For this reason the experimental data has been given at error range of ± 0.35 K.

Validation:

The experimental data used for validation purposes was drawn from the work of Chiu, Richards and Jaluria published in the 2001 Journal of Heat Transfer. The experiment consisted of an air filled channel with an aluminium section on the bottom. The bottom of the aluminium section had a surface heat source provided by an electrical heating pad. The bottom of the aluminium section had a surface heat source provided by an electrical heating pad. The experiment was designed to produce a laminar flow regime with a Reynolds Number of 9.48 [Chiu, Richards and Jaluria, 2001]. The paper provided temperature profiles for various heights in the channel, which were compared to the solutions generated by the simulations described below.

Domain:

The standard domain is two-dimensional and filled with air with the physical properties for 25°C and standard pressure. The domain includes the aluminum plate and the insulation adjacent to the plate. Temperatures in the solid regions are solved for directly as a conjugate heat transfer problem. Figure 5.2 shows the overall domain of the simulation and the relevant measurements.

Domain and Dimensions

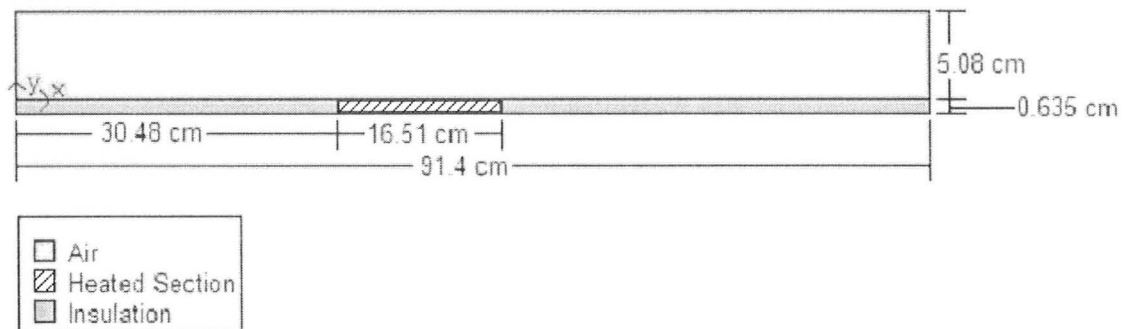


Figure 5.2 Horizontal Channel Domain

Boundary Conditions:

The boundary conditions are shown schematically in Figure 5.3.

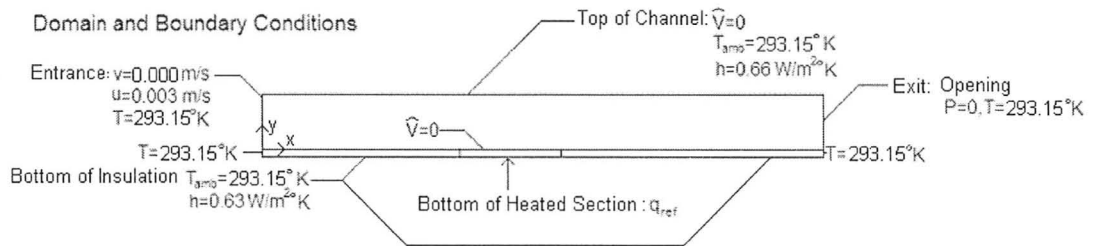


Figure 5.3 Domain and Boundary Conditions

The boundary conditions are further elaborated below:

Bottom of Heated Section: A solid boundary layer with a specified heat flux of $q_{ref}=12.7$ W/m^2 . This assumes that all of the heat generated passes through the aluminium section.

Top of Channel: A no slip wall with a coefficient of heat transfer of 0.66 W/m^2K to simulate two layers of insulation and an ambient temperature of $T_{amb}=293.15$ K.

Bottom of Insulation: A solid boundary with a coefficient of heat transfer of 0.63 W/m^2K to simulate layers of insulation and an ambient temperature of $T_{amb}=293.15$ K.

Entrance: An inlet with a uniform velocity profile of 0.003 m/s in the x direction only and a temperature of 293.15 K.

Exit: An opening with a pressure boundary condition of zero and a temperature of 293.15 K. An opening was used because the simulation produced recirculating flow, which made the outlet boundary condition unusable.

Meshing:

For meshing purposes the channel and bottom plate were divided into three sections, with each section having a solid and a fluid region. Figure 5.4 below shows the three sections and their regions.

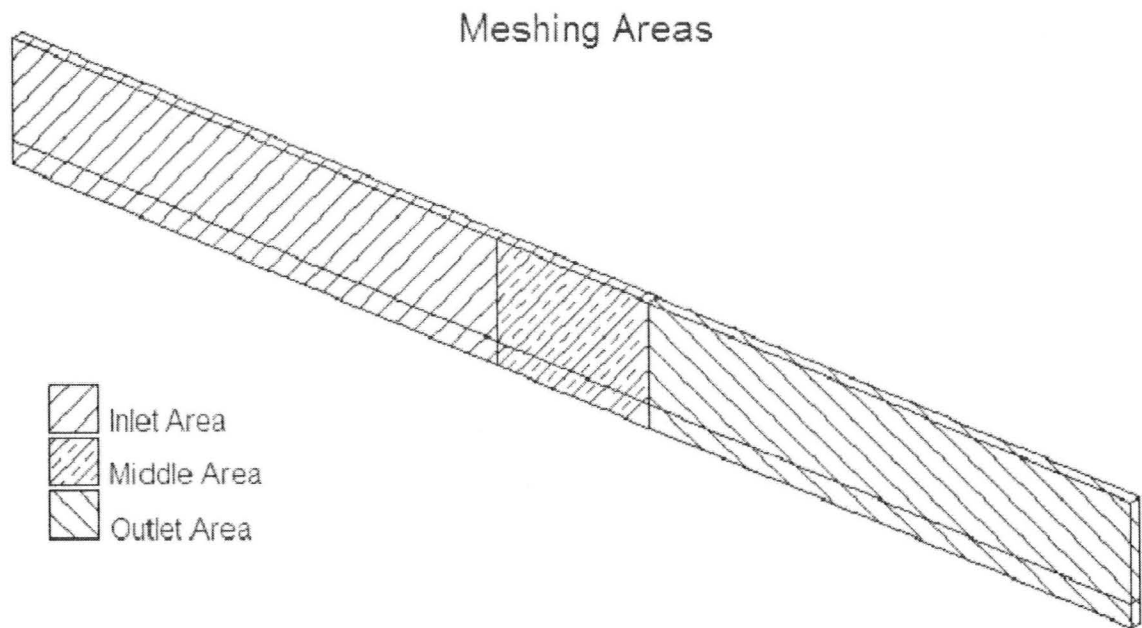


Figure 5.4 Meshing Areas of the Horizontal Channel

The inlet area consisted of the air channel and underlying Plexiglas from the air inlet to the beginning of the heated region. This area was meshed in the x direction using an expanding grid with the smallest grid size located at the end by the middle section and expanding downstream towards the inlet by a factor of 1.05, while the mesh in the y direction was uniform. The purpose of this region was to allow sufficient development length so that the assumed inlet velocity profile does not influence the flow over the heated section.

The middle area consisted of the heated section and the air directly above it. The mesh was created in a uniform pattern in both the x and y directions. The grid spacing in the x-direction was chosen to match the grid spacing at the inlet and outlet areas adjacent to the middle area.

The outlet area consists of the air channel and underlying Plexiglas from the end of the heated section to the outlet of the channel. The mesh was also uniform in the y direction with an expanding grid in the x direction. The smallest grid size was located adjacent to the end of the heated section and it expanded toward the outlet with a factor of 1.05.

Variations:

In addition to the standard simulation, simulations were run that varied the length of the channel and the ambient temperature. Table 5.2 shows all of the simulations presented here.

Simulation	Channel Length	Ambient Temperature	Prandtl Number
1	Standard	20	Standard
2	Extended	20	Standard
3	Standard	25	Standard
4	Standard	30	Standard

Table 5.2 Horizontal Channel with Heated Aluminum Section Simulations

Results:

Temperature

An important measurement of success was the temperature profiles recorded at varying heights of the channel. They were provided in non-dimensional form and have been converted to absolute terms for ease of presentation. As mentioned in the measurement section, the error associated with experimental data is 0.35 K. Figure 5.5 below compares the temperature of the simulations with the experimental data at the bottom, middle and top of the channel over the heated section.

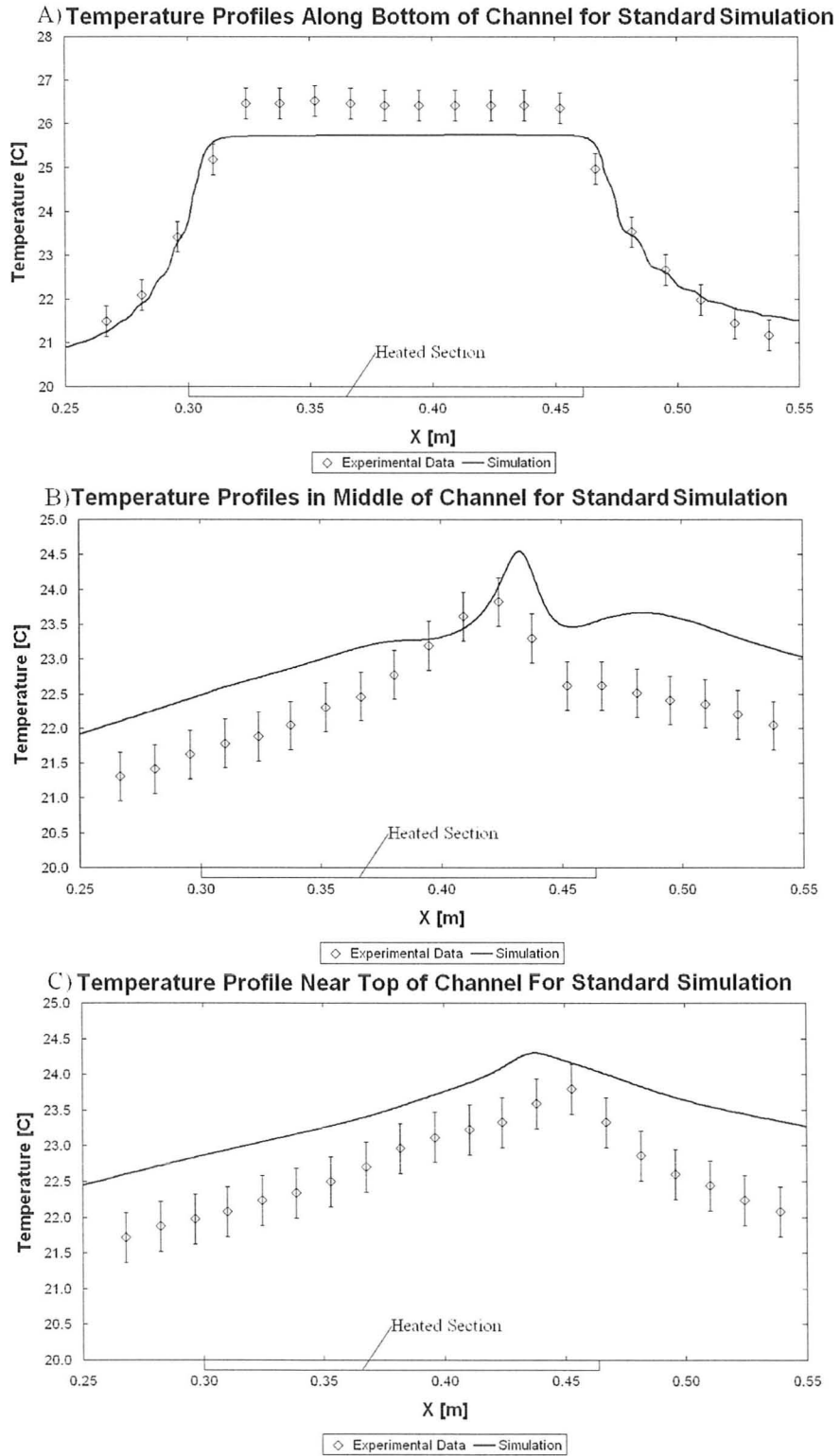


Figure 5.5 Temperature Profiles for the Standard Simulation at; A) $y/H=0$, B) $y/H=0.5$, C) $y/H=0.875$

Discussion:

Double Precision

The ANSYS CFX solver was required to run in double precision to double the number of significant digits used from eight to sixteen [ANSYS CFX, “Numerical Errors”, 2006]. Prior to the use of double precision variables the grid size was limited due to the temperature gradient. Given the thickness of the heated section and the heat flux of 12.7 W/m^2 , the temperature difference across the section, in a one-dimensional simulation would be 0.00045 K. This difference divided between ten nodes in the section would have been insignificant enough that it would only barely appear in the final result and not at all during the initial iterations.

Grid Independence

It was important to see that the results were independent of the mesh, therefore, the space between adjacent nodes in the middle area was halved and a new mesh created in the same way as described in the meshing section. Figure 5.6 below compares the results of the standard mesh and the refined mesh for three heights over the heated section. As seen in the figure, the results are independent of the grid.

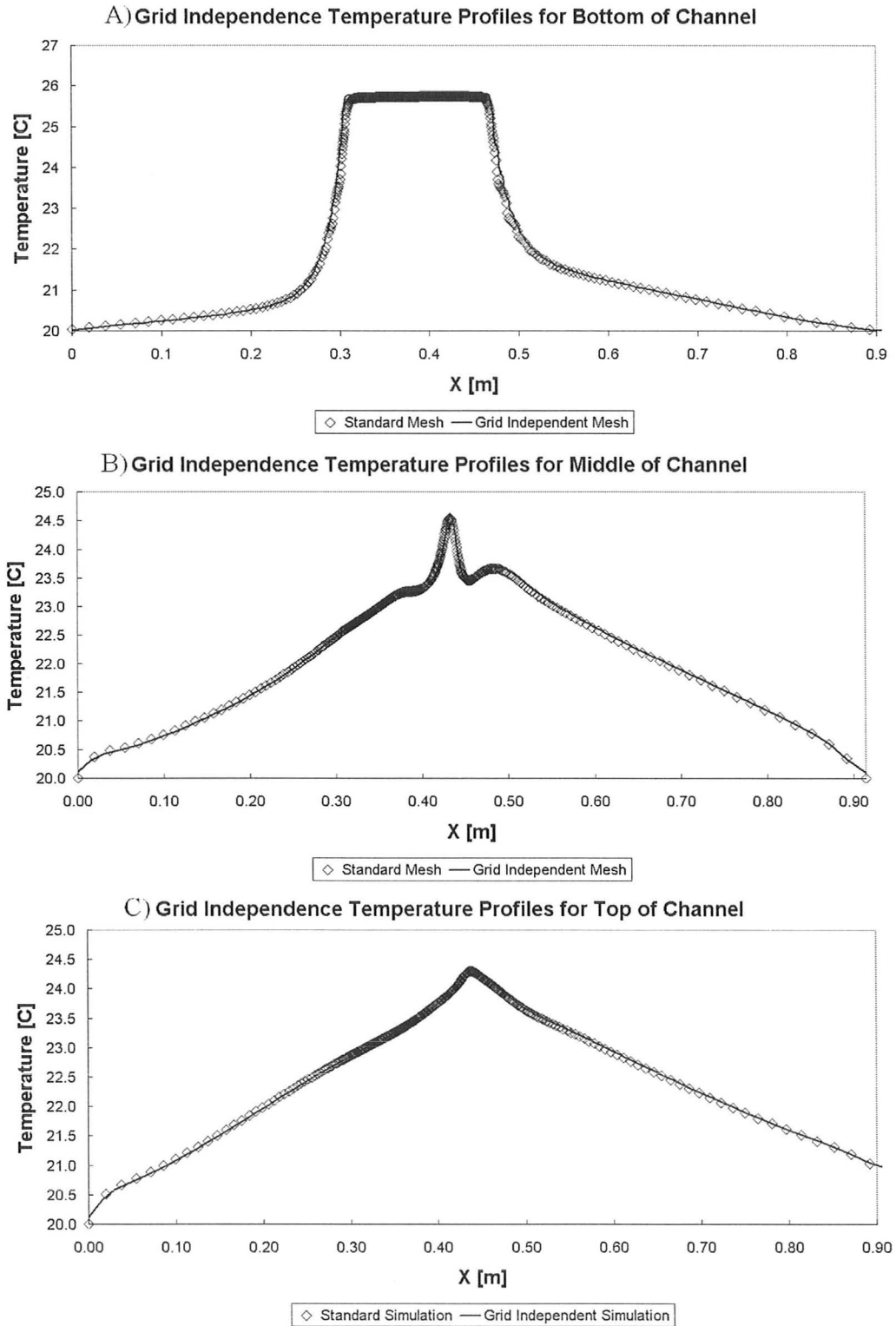


Figure 5.6 Temperature Profiles for Grid Independent Simulation at; A) $y/H=0$, B) $y/H=0.5$, C) $y/H=0.875$

Recirculating Flow

As mentioned in the boundary conditions the simulation produced a recirculating flow in the outlet section shown in Figure 5.4. Figure 5.7 shows the flow in this section.

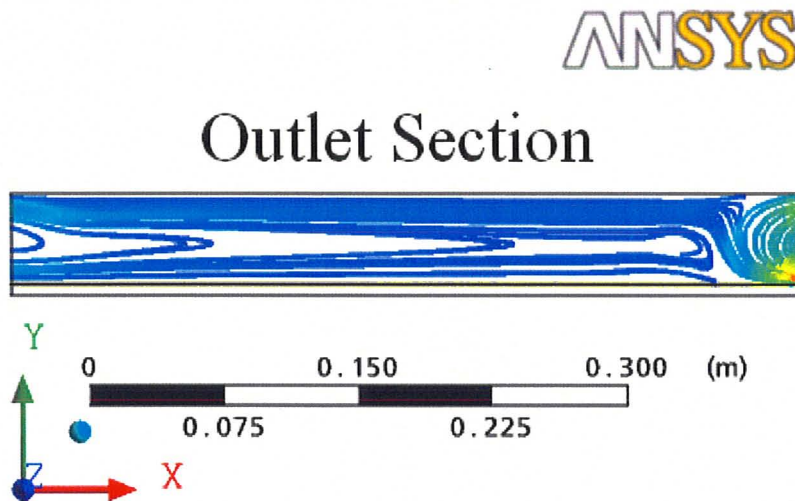


Figure 5.7 Recirculating Flow at Channel Exit

The experimental data indicated that there was some recirculating flow after the heated section but it was not shown how it resolved at the channel exit. This is the reason why simulations with an extended channel were run.

Temperature Profiles

As seen in Figure 5.5 the error in the simulation increases as the results move farther from the bottom of the channel. The maximum error along the bottom of the channel is 0.8 K. The general shape of the temperature curve is also correct; only the magnitude of the flat section over the heated section is under estimated. The middle height of the channel has a maximum error in the temperature profile of 1.1 K and although it has the correct general shape it is shifted up and towards the end of the channel. The top part of the channel has a maximum error of 1.2 K and has the proper

shape but it is shifted up and towards the beginning of the channel. This would suggest that the simulation source of error may be in the modeling of the air. Figure 5.5 shows that the temperature is under predicted over the heated section and over predicted in the air.

Temperature Difference

In addition to the error in the magnitude of the temperature, the simulation also under predicts the temperature stratification in the channel. It should be noted that the stratification is in the reverse of what is normally observed in stratified air because the heat flux is from the bottom of the channel, which makes the lower air hotter than the air at the top. Figure 5.8 show the experimental temperature difference from the middle of the channel to the bottom.

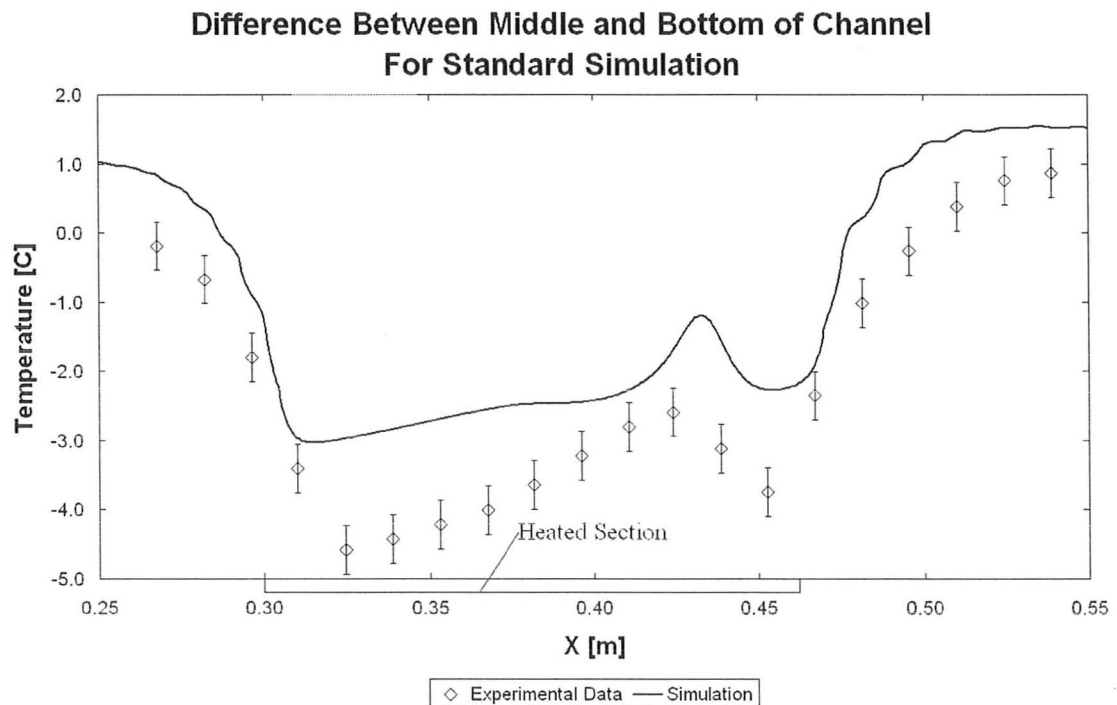


Figure 5.8 Temperature Difference Between $y/H=0.5$ and $y/H=0$

The predicted temperature difference has the same shape as the experimental data but under predicts the magnitude of difference. Figure 5.9 shows the same data for the top of the channel with respect to the bottom of the channel.

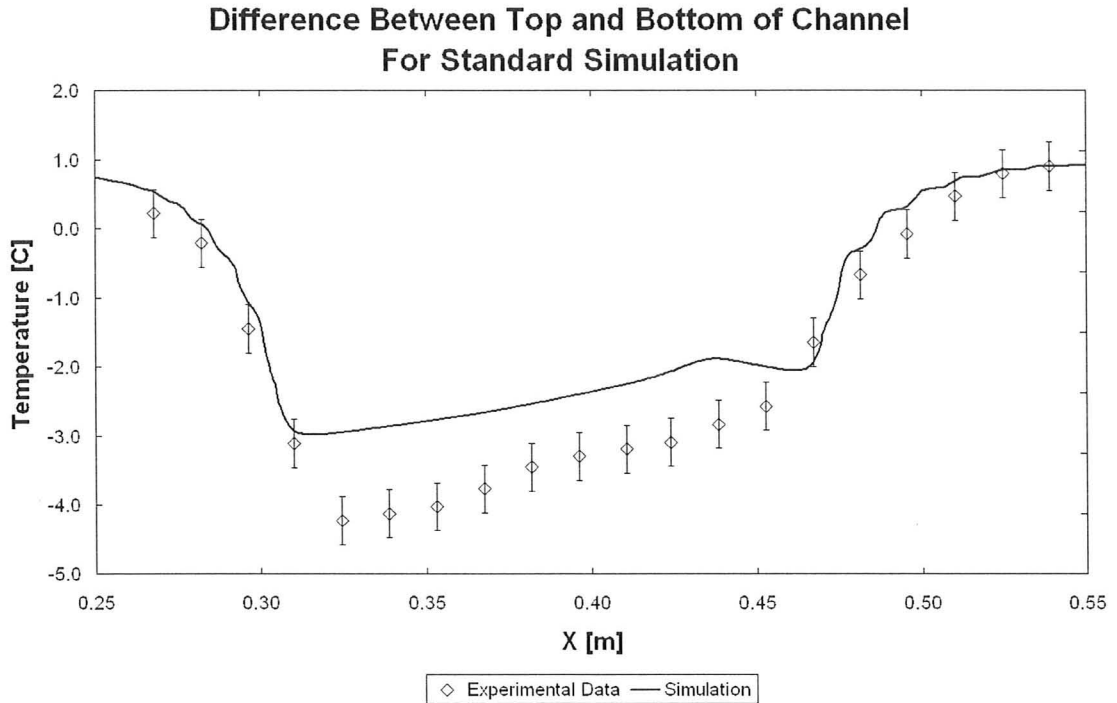


Figure 5.9 Temperature Difference Between $y/H=0.875$ and $y/H=0$

Figure 5.9 also shows the temperature difference between the top and bottom of the channel has the same trend of under prediction with the correct general shape.

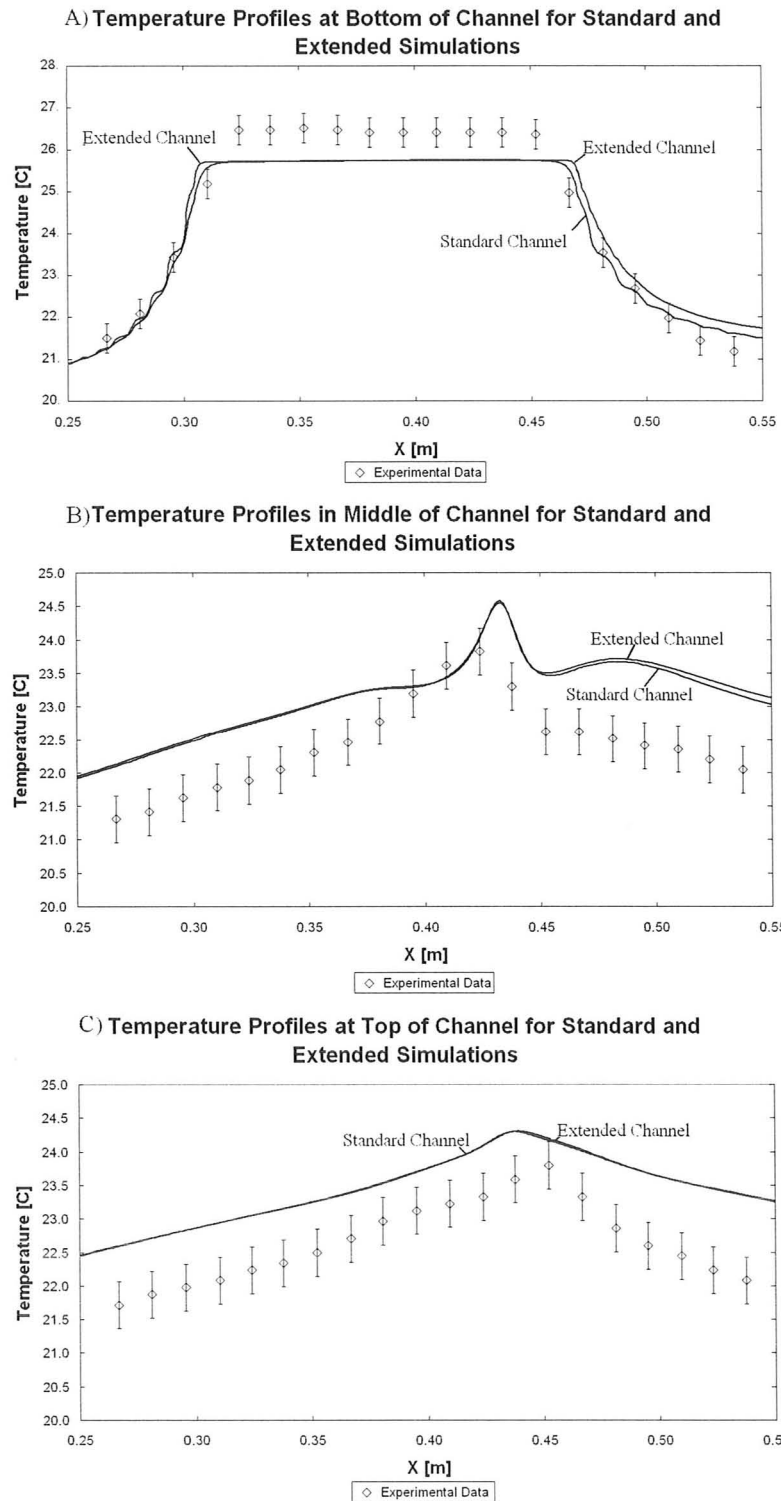


Figure 5.10 Temperature Profiles for Extended Simulation at; A) $y/H=0$, B) $y/H=0.5$, C) $y/H=0.875$

Discussion:

Figure 5.10 show that there is almost no change in the temperature profiles above the heated section. The temperature profiles after the heated section show a small change in the results. The change is more noticeable as the results approach the bottom of the channel. At the top there is virtually no difference between the temperature profiles. The bottom profiles show the same magnitude of temperature over the heated section but the flat area extends farther towards the exit with the extended channel and has smooth approaches to the flat area rather than the waves seen in the standard channel.

If the temperature is shown for the entire channel length, as in Figure 5.11 below, there is a greater difference in the result as the flow approaches the exit.

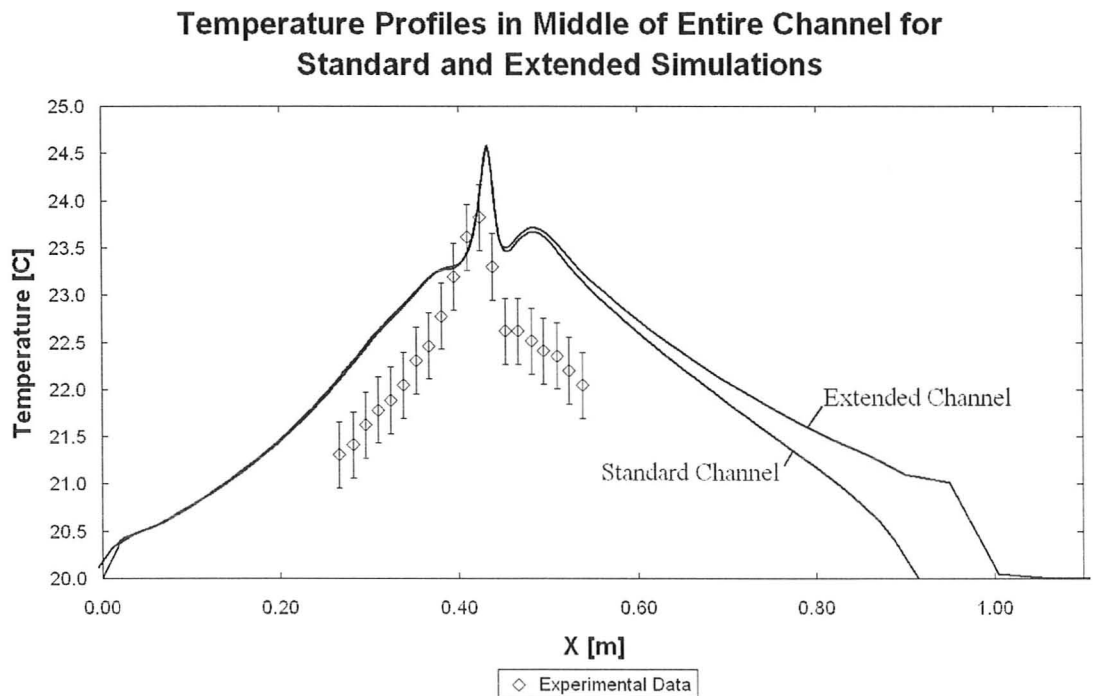


Figure 5.11 Extended and Standard Simulation for Entire Channel Length.

However, this was expected as the exit location changed. Therefore, the solution over the heated section was insensitive to the recirculation at the channel exit.

5.2.3 Ambient Temperature Variations

Motivation:

The experimental data is provided in the non-dimensional variable of theta, as defined in Table 5.1, however, the data does not provide the ambient temperature at the time it was collected. For the purpose of the standard simulation the ambient temperature was assumed to be 20°C. It is important to determine if the results are sensitive to the ambient temperature otherwise, the precise ambient temperature during the experiment must be known.

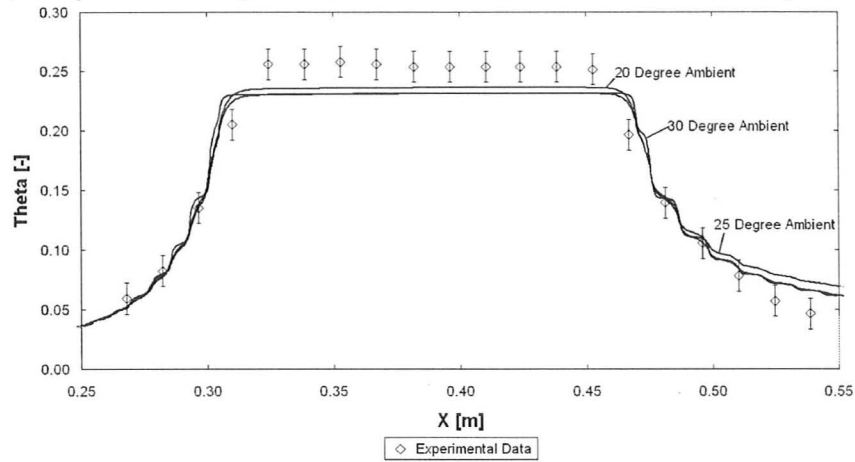
Modification:

The boundary condition variable T_{amb} was modified to reflect an ambient temperature of 25°C and 30°C. This included the surfaces with a coefficient of heat transfer, the ends of the insulation, the entrance and the exit of the channel.

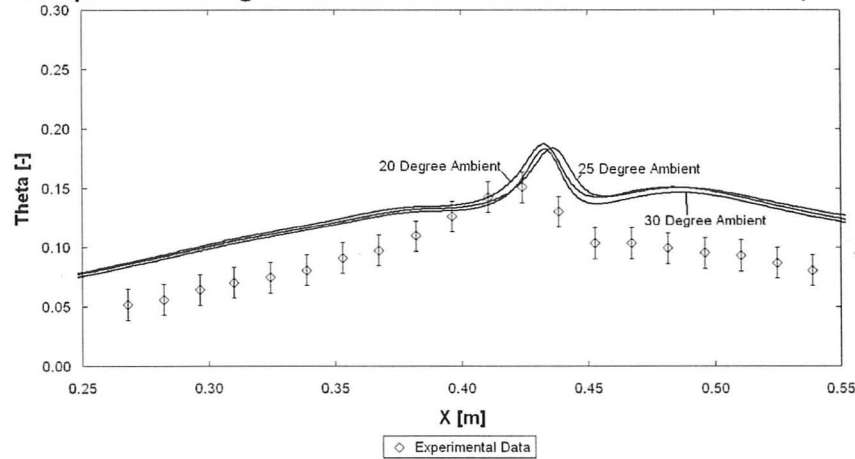
Results:

The results were shown in the dimensionless temperature theta, as shown in Table 5.1. This was done so that the results could be compared as shown in Figure 5.12 below.

A) Temperature Along Bottom of Channel for Different Ambient Temperatures



B) Temperature Along Middle of Channel for Different Ambient Temperatures



C) Temperature Along Top of Channel for Different Ambient Temperatures

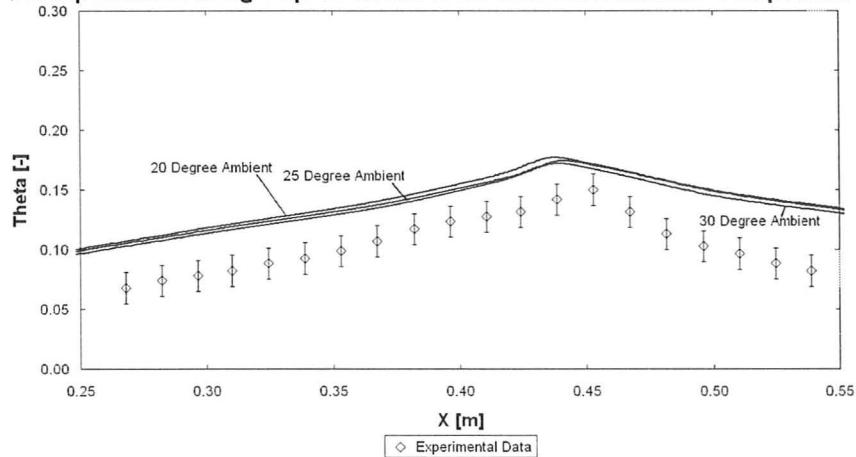


Figure 5.12 Temperatures for ambient temperature simulations at; A) $y/H=0$, B) $y/H=0.5$, C) $y/H=0.875$

Discussion:

Figure 5.12 shows very little sensitivity to the ambient temperature. At all three heights there is little change in the solution provided. The differences shown are insignificant when compared to the error in the experimental data.

5.3 Conclusions

ANSYS CFX was able to model the general trends of the temperatures in the horizontal channel. The simulations also under predicted the temperature difference between the top and the bottom of the channel and did not match the temperature field in terms of magnitude, often over predicting the temperature of the air. The maximum error however was 1.2 K. The stratification in the channel was under predicted but the general trends were followed. Therefore ANSYS CFX does a good job of simulating the qualitative aspects of the simulation, but could improve the quantitative aspects.

Chapter 6 Atrium Validation Simulations

6.1 Background

6.1.1 Interaction of Phenomena



Figure 6.1a Concordia's Atrium
[Photo Credit: Solar Building Research Network &
Concordia University, Used with Permission of Meli Stylianou]

operates with a much higher Rayleigh number than validation data is generally available for and with much more complicated radiation interaction. This chapter presents simulations of the heat transfer and fluid flow within the Concordia university engineering building atrium. Predictions are compared to experimental results collected by Eleni Mouriki and Dr. Karava.

Atria are an important feature of building design. This thesis has evaluated ANSYS CFX's ability to model the individual phenomena that are important to an atrium. In order to determine ANSYS CFX's ability to handle the three phenomena together a genuine atrium simulation must be made. What makes an atrium unique is the interaction between these phenomena. Scale is also an important component. An atrium

6.1.2 Definitions

For the purposes of this chapter and all related discussion the variables and parameters are defined in Table 6.1

Symbol	Description	Value	Units
BI	Diffuse Radiation Source Magnitude on the Blinds	$0.08*SI*\cos(\text{SOLAR})$	$[\text{W}/\text{m}^2]$
FI	Heat Flux for Sun on the Floor	$SI*\sin(\text{SOLAR})$	$[\text{W}/\text{m}^2]$
SI	Solar Radiation Heat Flux	1370	$[\text{W}/\text{m}^2]$
SOLAR	Zenith Angle of the Sun	32°	[Degrees]
T	Temperature		[C]
ΔT	Temperature Stratification	$T_{16}-T_{14}$	[C]
T_{14}	Temperature at 2.1m		[C]
T_{15}	Temperature at 6.3 m		[C]
T_{16}	Temperature at 10.3m		[C]
X_1	Location marker for floor heat flux	$Y_1/\tan(\text{SOLAR})$	[m]
X_2	Location marker for floor heat flux	$Y_1/\tan(\text{SOLAR})$	[m]
X_3	Location marker for floor heat flux	$Y_1/\tan(\text{SOLAR})$	[m]
X_4	Location marker for floor heat flux	$Y_1/\tan(\text{SOLAR})$	[m]
X_5	Location marker for floor heat flux	$Y_1/\tan(\text{SOLAR})$	[m]
X_6	Location marker for floor heat flux	$Y_1/\tan(\text{SOLAR})$	[m]
Y_1	Height to beginning of first gap in blinds	1.00 m	[m]
Y_2	Height to ending of first gap in blinds	1.26 m	[m]
Y_3	Height to beginning of second gap in blinds	5.00 m	[m]
Y_4	Height to ending of second gap in blinds	5.26 m	[m]
Y_5	Height to beginning of third gap in blinds	9.00 m	[m]
Y_6	Height to ending of third gap in blinds	9.26 m	[m]
ϵ_{Facade}	Emissivity of the facade		[-]

Table 6.1 Variables and Parameters

6.1.3 Models & Theory

Solar Heat Flux Magnitudes:

In order to calculate the magnitude of the solar radiation heat flux of surfaces not perpendicular to the solar angle, conservation of energy was used. Figure 6.1 below shows the control volume used in the conservation of energy equation.

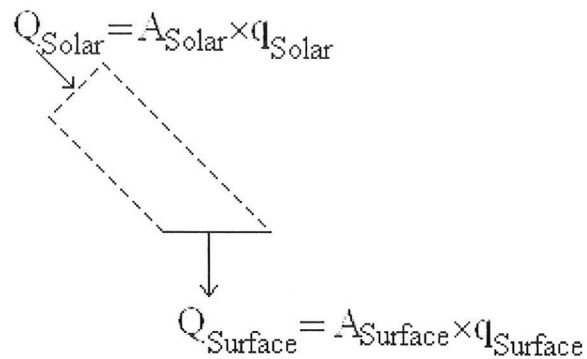


Figure 6.1 Control Volume for Solar Heat Flux Magnitude Calculations

The side surfaces of the control volume are parallel with the solar radiation; therefore, the total energy for the solar radiation must impact on the surface. Since the total energy must be conserved $Q_{\text{Solar}} = Q_{\text{Surface}}$. Figure 6.2 shows the dimensions used to calculate the areas for the atrium simulation.

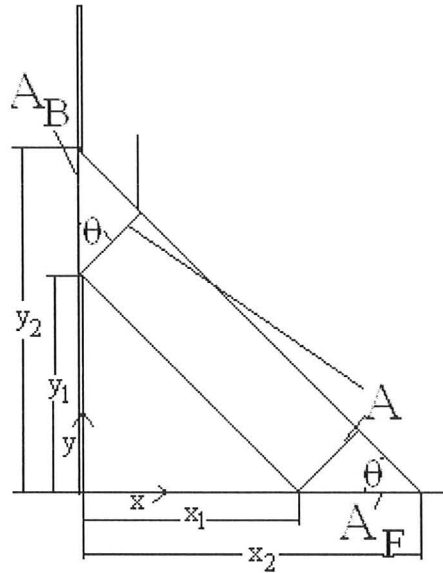


Figure 6.2 Surfaces and Diagrams for Calculation of Solar Radiation Magnitude

The general principle was that the amount of heat flux should be uniform on any surface struck and that each surface regardless of the relative angle should have the same total heat flow. This is expressed in equation 6.1.

$$A_B BI = ASI = A_F FI \quad (\text{Equation 6.1})$$

The areas can be related by trigonometry as shown in equation 6.2, and therefore equation 6.1 can be rearranged into equation 6.3 & 6.4.

$$A = A_F \sin \theta = A_B \cos \theta \quad (\text{Equation 6.2})$$

$$FI = SI \frac{A}{A_F} = SI \sin \theta \quad (\text{Equation 6.3})$$

$$BI = SI \frac{A}{A_B} = SI \cos \theta \quad (\text{Equation 6.4})$$

These equations were used to determine the magnitude of the heat fluxes and diffuse radiation sources, which resulted from the solar radiation.

ANSYS CFX Solar Model:

ANSYS CFX does not provide a method to predict the angle or properties of solar radiation. As such, the calculations for the sun's zenith angle were done manually. The full calculations involved can be found in Appendix G. Furthermore, directional radiation sources are only available in the Monte Carlo radiation model. This model was not used, for reasons discussed in the Chapter 4. Therefore, the location that the solar radiation struck the floor had to be calculated and a heat flux used, as was done in Chapter 4. Finally, the heat flux from the solar radiation was only included on the floor to simplify the model. This was done by assuming that the sun was positioned directly in front of the atrium. In practice, the sun was approximately only three degrees from this position at the time at which the experiments took place.

6.2 Simulations

6.2.1 Concordia Atrium Simulation

Description:

This simulation is based on the atrium in the University of Concordia's EV building at St Catherine and Guy in Montreal. The simulation is steady state and based on a simplified geometry of the actual atrium. The time of day was set to noon and blinds of the atrium were partially closed, in agreement with experimental conditions.

Measurements:

The absolute temperature recorded within the atrium was used for validation. The temperatures were recorded by thermocouples with an error of ± 0.2 K and were hung from the ceiling along three strings. These thermocouple strings are referred to as East,

Center and West, based on their location in the atrium. Each string held three thermocouples, located at 10.3m, 6.3m and 2.1m from the floor of the atrium.

Validation Source:

The data used to validate the simulations and to develop the boundary conditions was collected at Concordia University on October 26, 2007. The data collection was done when the blinds of the atrium were partially closed and the mechanical ventilation in use.

Domain:

The simulation was run using a simplified model of the atrium interior. The domain was filled with air using constant properties for conditions of 25°C and standard pressure. The Boussinesq buoyancy model was used along with the $k-\omega$ turbulence model. The Rayleigh number based on the maximum temperature difference and atrium height is 2.3×10^{12} . The general dimensions of the atrium were followed but for convenience the staircase and chairs were ignored, as were small nooks in the design. For reasons related to the mesh generator and ANSYS CFX the overall domain was divided into twenty-eight sub-domains. Figure 6.2 shows the atrium's orientation and general shape.

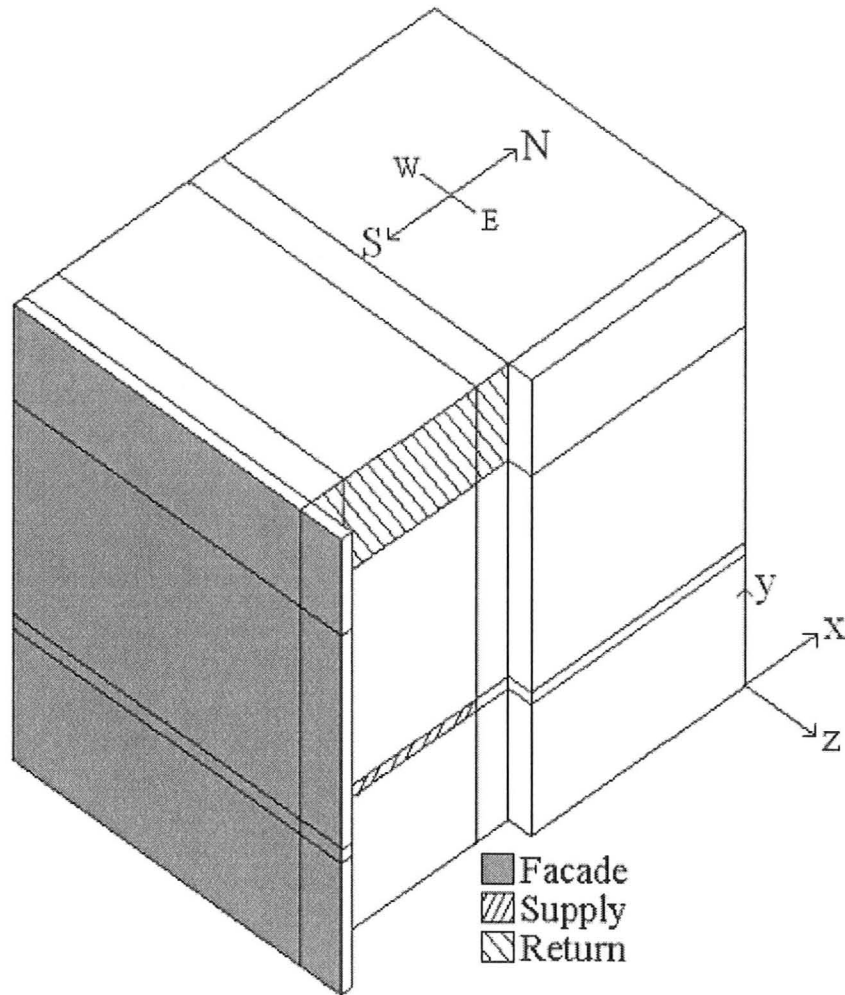


Figure 6.3 Atrium Domain and General Orientation.

Figure 6.4 shows both the atrium's dimensions and sub-domains.

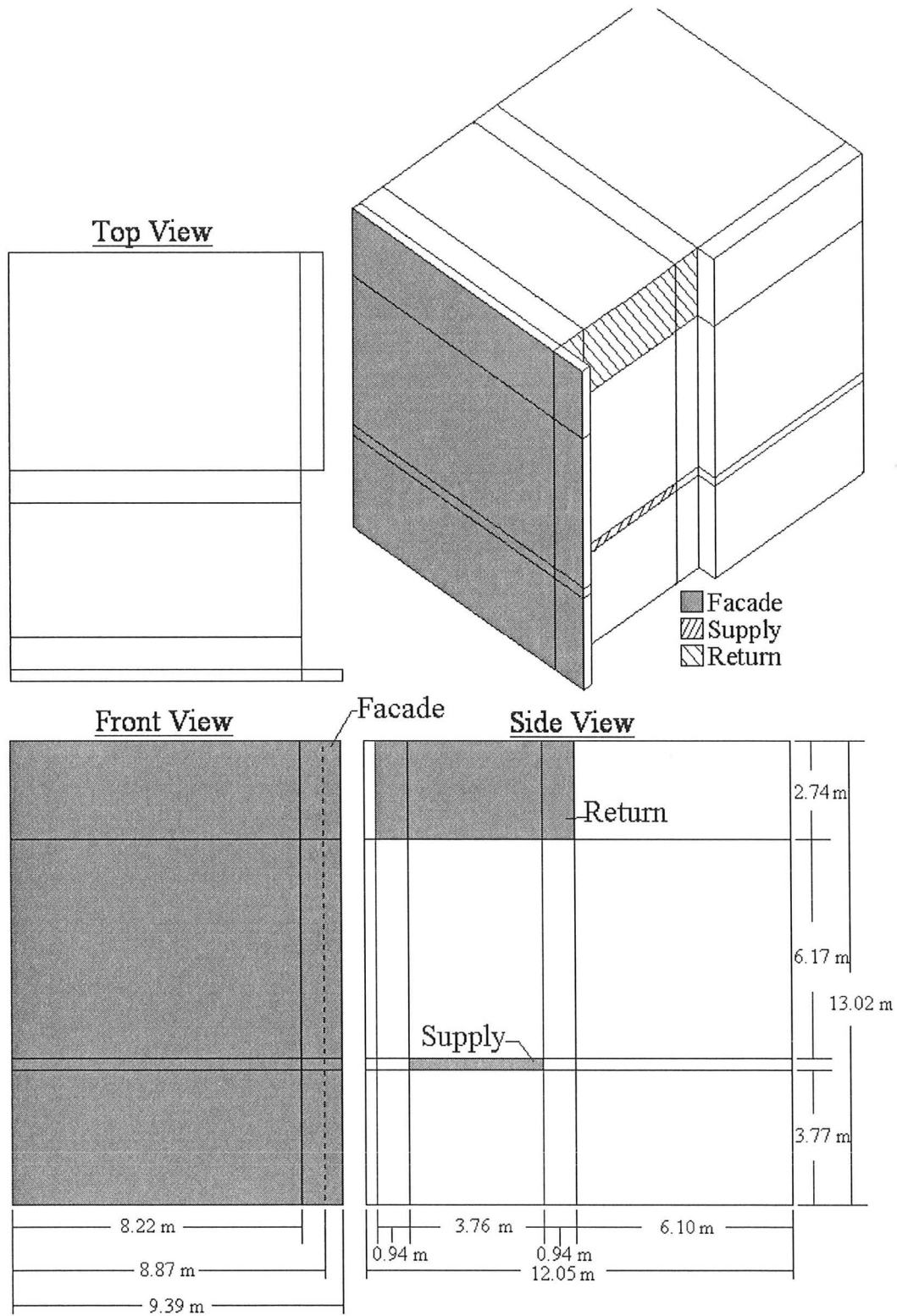


Figure 6.4 Atrium Dimension and Sub Domains

Boundary Conditions:

Façade: The façade is the transparent wall of the atrium that allows solar radiation to easily enter the atrium. The façade was a no slip wall with a specified temperature boundary condition. In the experimental atrium the blinds covered most of the façade. The specified temperature was developed based on temperature recordings along the blinds. The profile is constructed of three sections, each corresponding to one of the areas of blinds, combined using the methods discussed in Appendix F. The blinds, which partially covered the façade, transmitted approximately 8% of the sunlight into the atrium as a diffuse source. As such, the simulations include a diffuse radiation source. The diffuse source is only located where the blinds would be and is absent otherwise. The equation for the magnitude of this source can be found in Table 6.1. The façade was treated as a black body with an emissivity of unity, unless otherwise indicated in specific simulations. Figure 6.5 shows how the temperature is distributed on the façade.



Facade Specified Temperature Profile

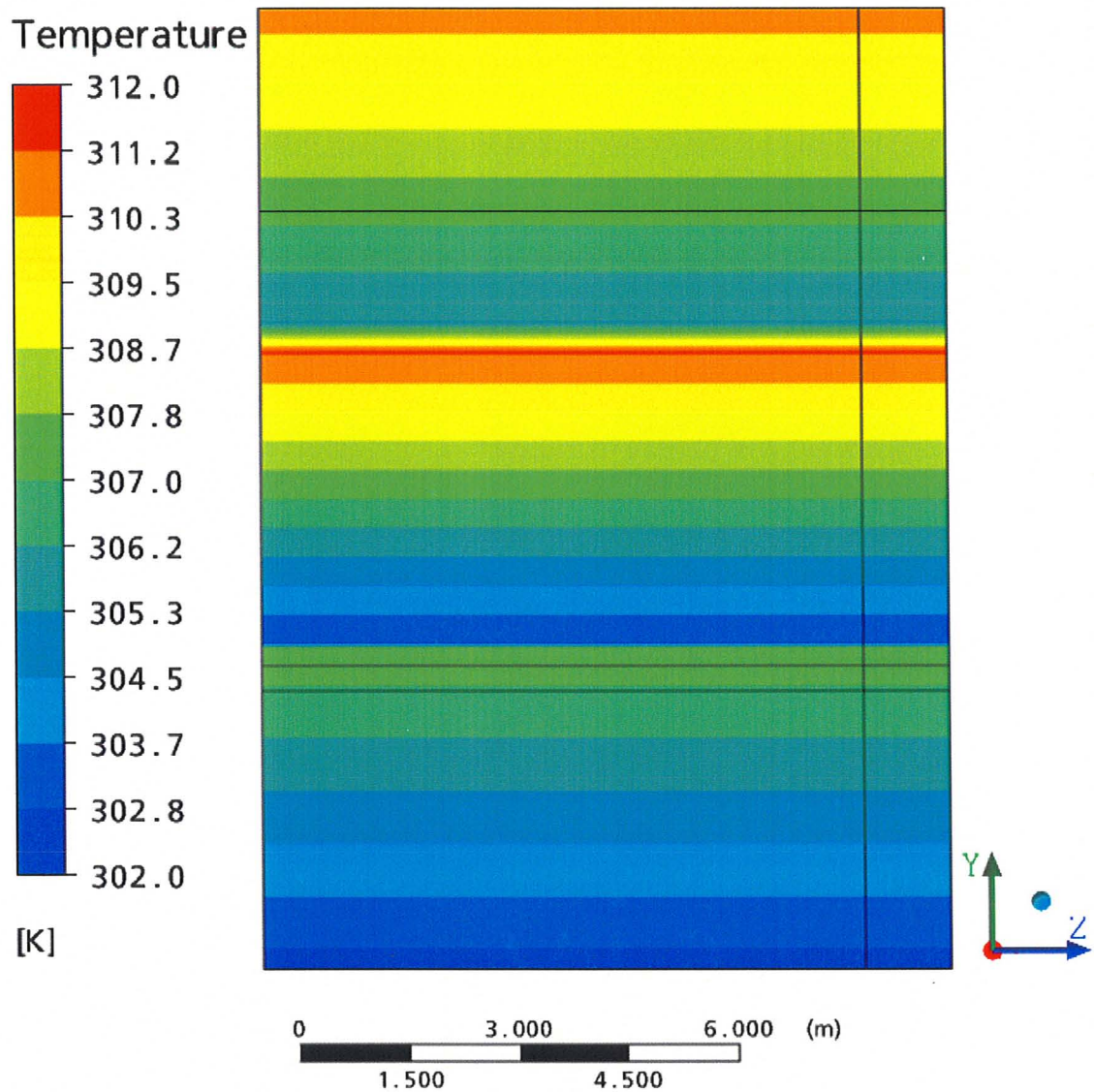


Figure 6.5 Façade Specified Temperature Boundary Condition

Floor: The floor of the atrium was bound by a specified heat flux. The areas where the sunlight, which passed through the façade, struck the floor were given a heat flux. Therefore, the entire floor is given a specified heat flux with a value of zero except where

sunlight struck the floor. The equation for the magnitude of the flux can be found in Table 6.1.

Supply: The supply is the source of mechanical ventilation for the atrium. It supplies air at a constant temperature of 17°C and a uniform velocity that creates the correct mass flow rate of 0.42 kg/s. These values were determined based on measurements taken in the atrium at the time considered by the simulation. There is some uncertainty in the values, because the measurement was only taken at single point.

Return: The return serves as the mechanical exhaust for the atrium and is modeled as an opening with a pressure of zero and a temperature of 25 °C.

Walls: The walls were adiabatic no slip walls.

North End: The north end is the boundary on the north end of the atrium opposite of the façade. In the experimental atrium the north end opens onto the corridors of the floors which connect with the atrium. In the simulation the north end was treated as a no slip adiabatic wall.

Mesh:

The domain was meshed with an expanding mesh. The initial spacing was set to 0.006m with an expansion factor of 1.14. This produced a mesh with 740,000 nodes. For the grid independence mesh the initial distance was halved and the expansion factor kept the same. Figure 6.6 shows the isometric image of the mesh.

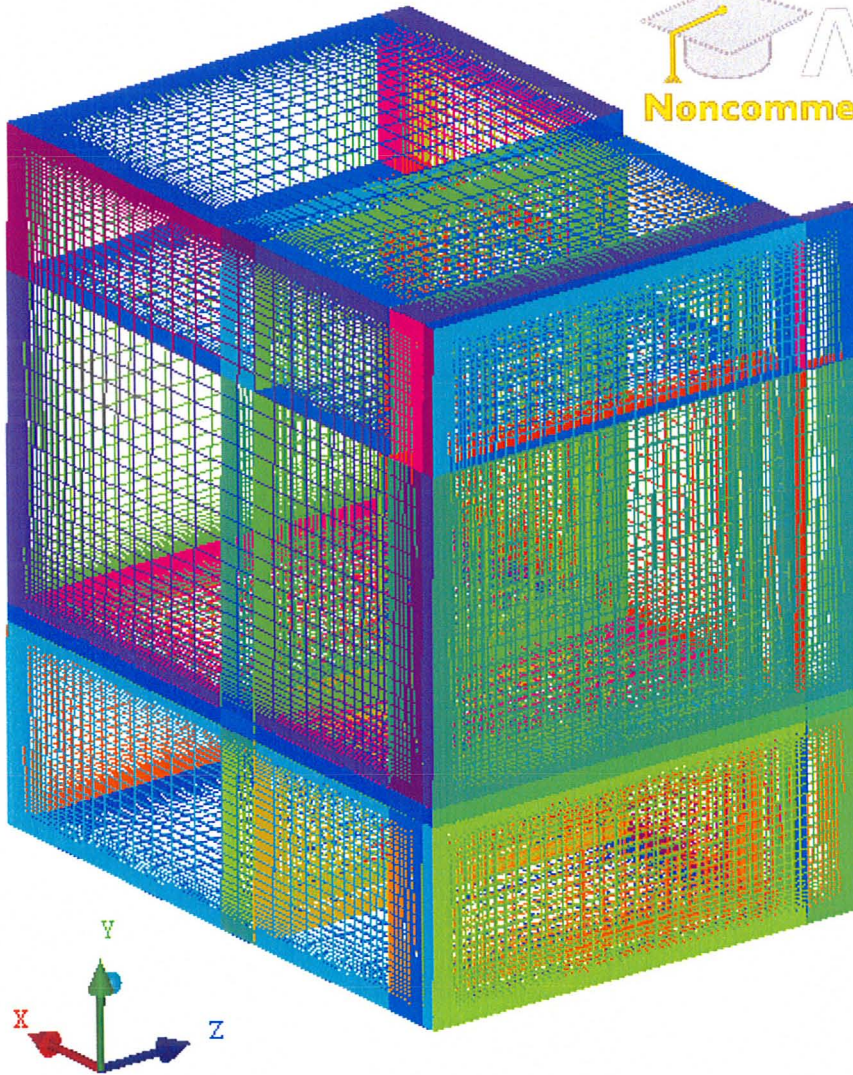


Figure 6.6 Isometric View of Mesh

The mesh in the y direction was designed to allow for fine mesh at the supply area of the atrium. This was done in a smooth fashion with a uniform mesh across the supply area. Figure 6.7 shows the mesh in the y direction.

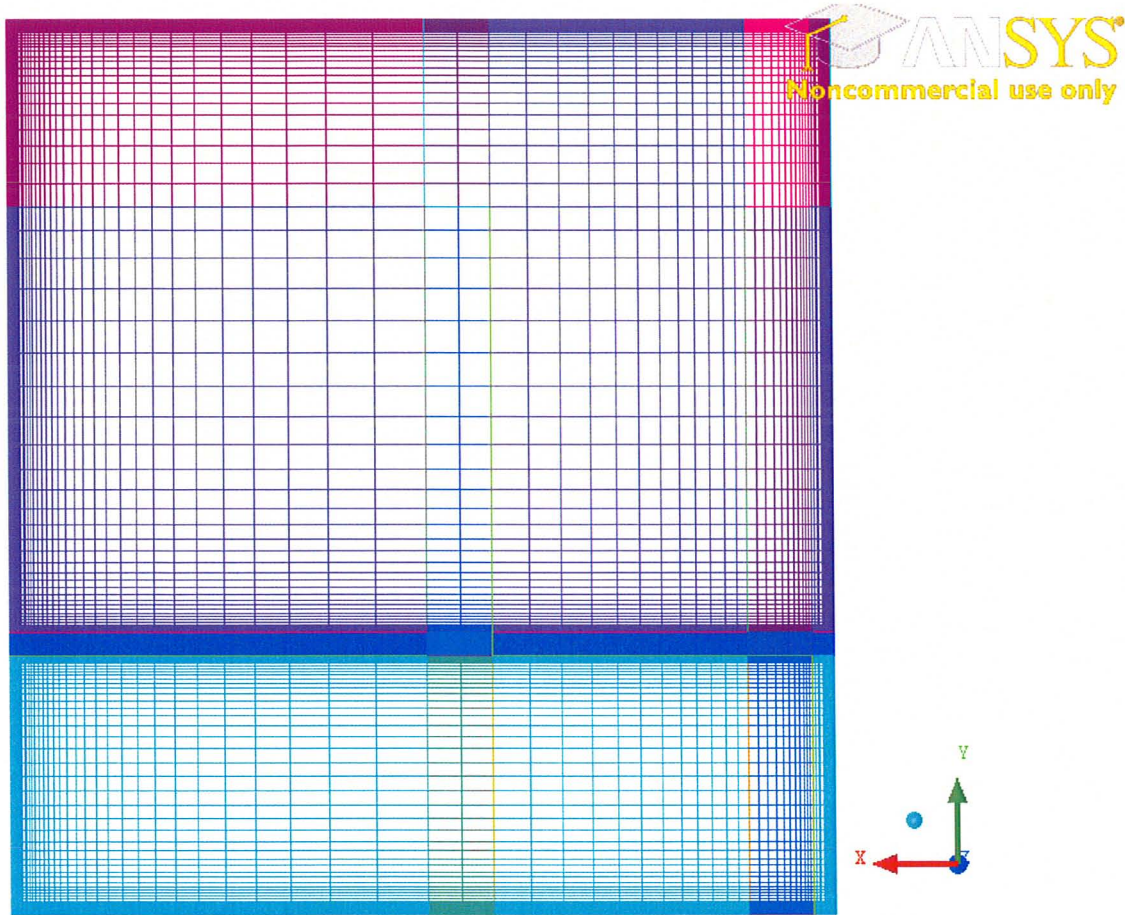


Figure 6.7 Mesh in the y Direction

Variations:

The standard simulation was run using full solar radiation. Other simulations changed the emissivity of the façade and the magnitude of the solar radiation. Table 6.2 shows all of the simulations presented here and their parameters.

Simulation	Radiation Model	Solar Radiation Magnitude	Façade Emissivity
Solar Radiation	Discrete Transfer	1370 W/m ²	1.0
Façade Emissivity 1	Discrete Transfer	1370 W/m ²	0.5
Façade Emissivity 2	Discrete Transfer	1370 W/m ²	0.8
0% SI	Discrete Transfer	0 W/m ²	1.0
25% SI	Discrete Transfer	343 W/m ²	1.0
50% SI	Discrete Transfer	685 W/m ²	1.0
75% SI	Discrete Transfer	1028 W/m ²	1.0

Table 6.2 Atrium Simulations Presented

Further atrium simulations can be found in Appendix H.

Results:

Temperature

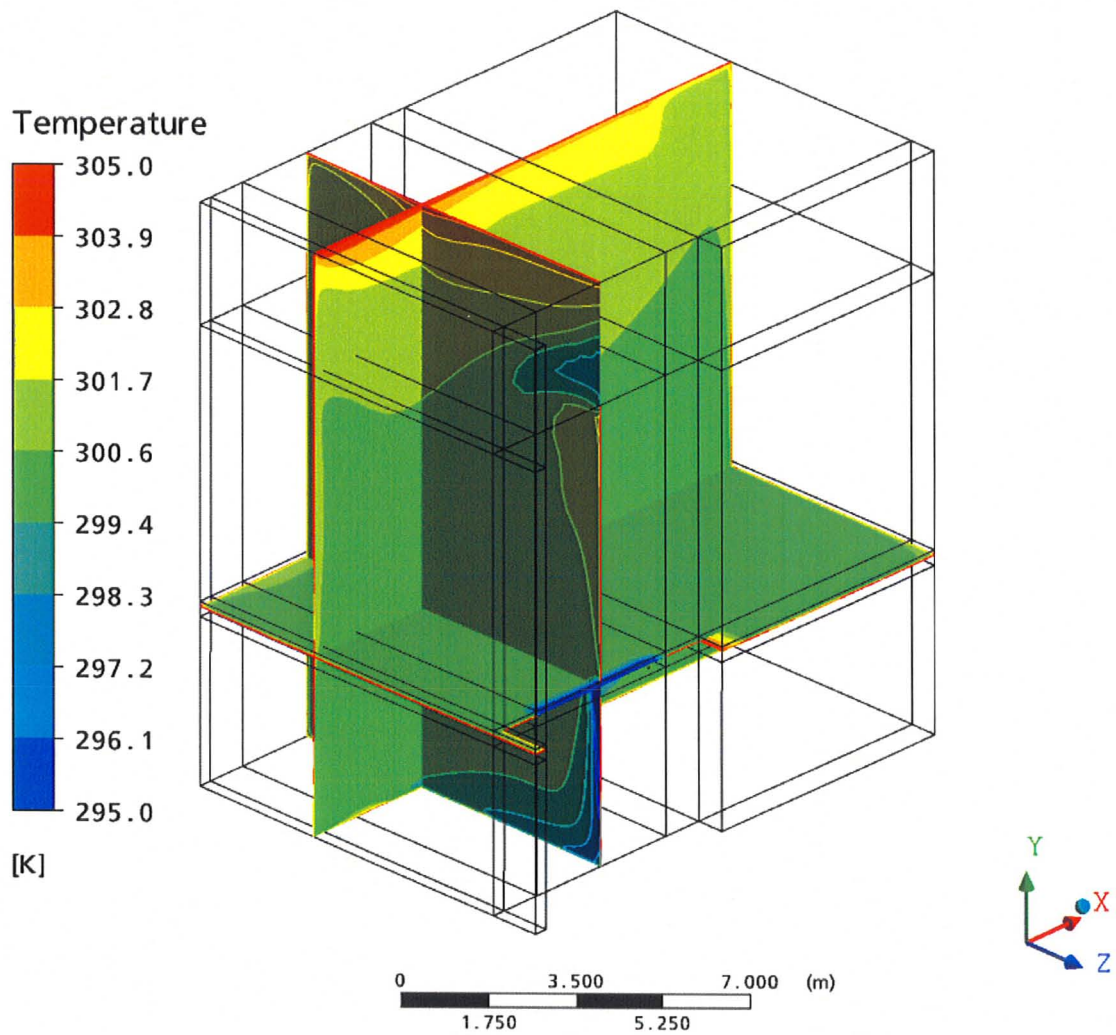


Figure 6.8 Temperatures Along Three Planes in the Atrium

The highest temperatures were located on the floor and these are shown in Figure 6.9.

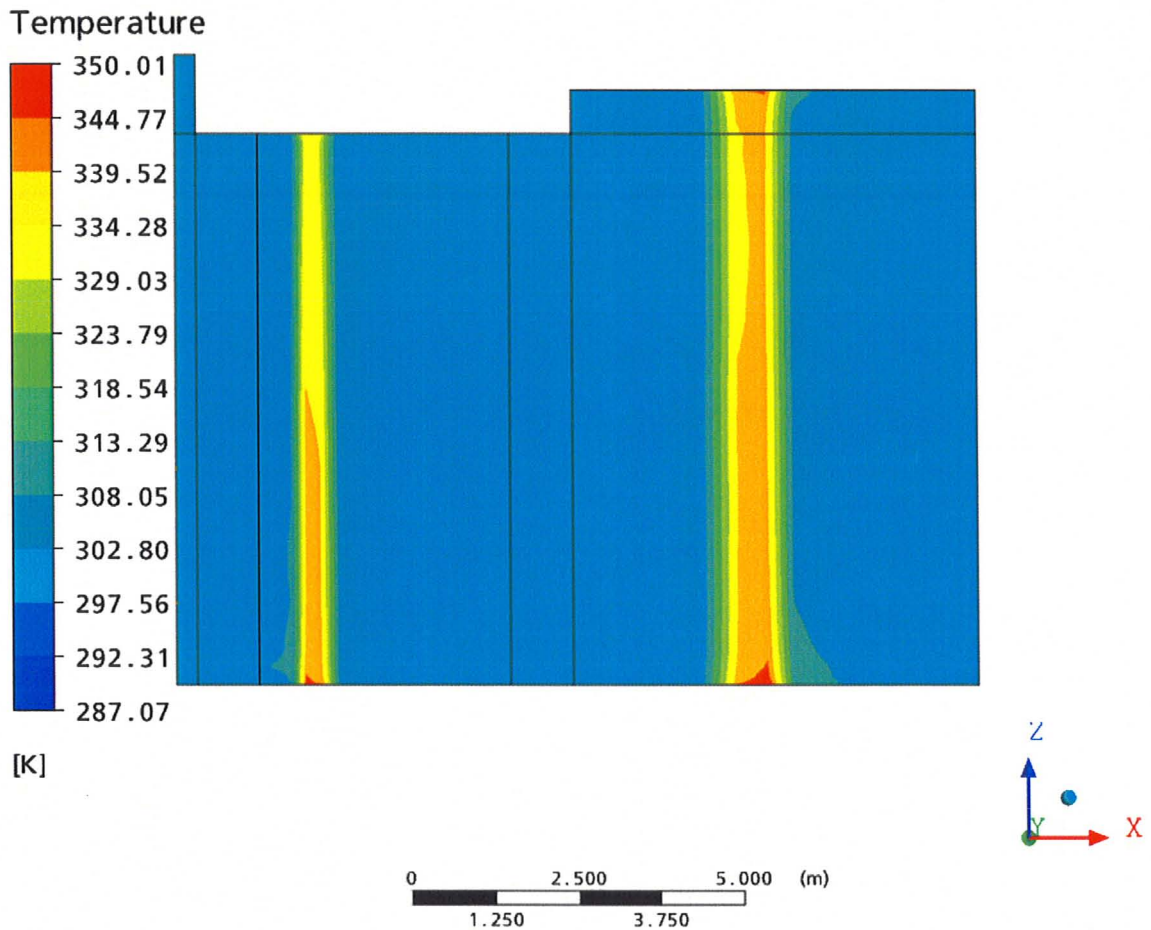


Figure 6.9 Floor Temperature for Solar Simulation

Aside from the general temperature field the temperatures recorded by the thermocouples discussed in the measurement section of this chapter were used as a measurement of accuracy. Figure 6.10 compares the temperatures recorded during the experiment and those of the simulation.

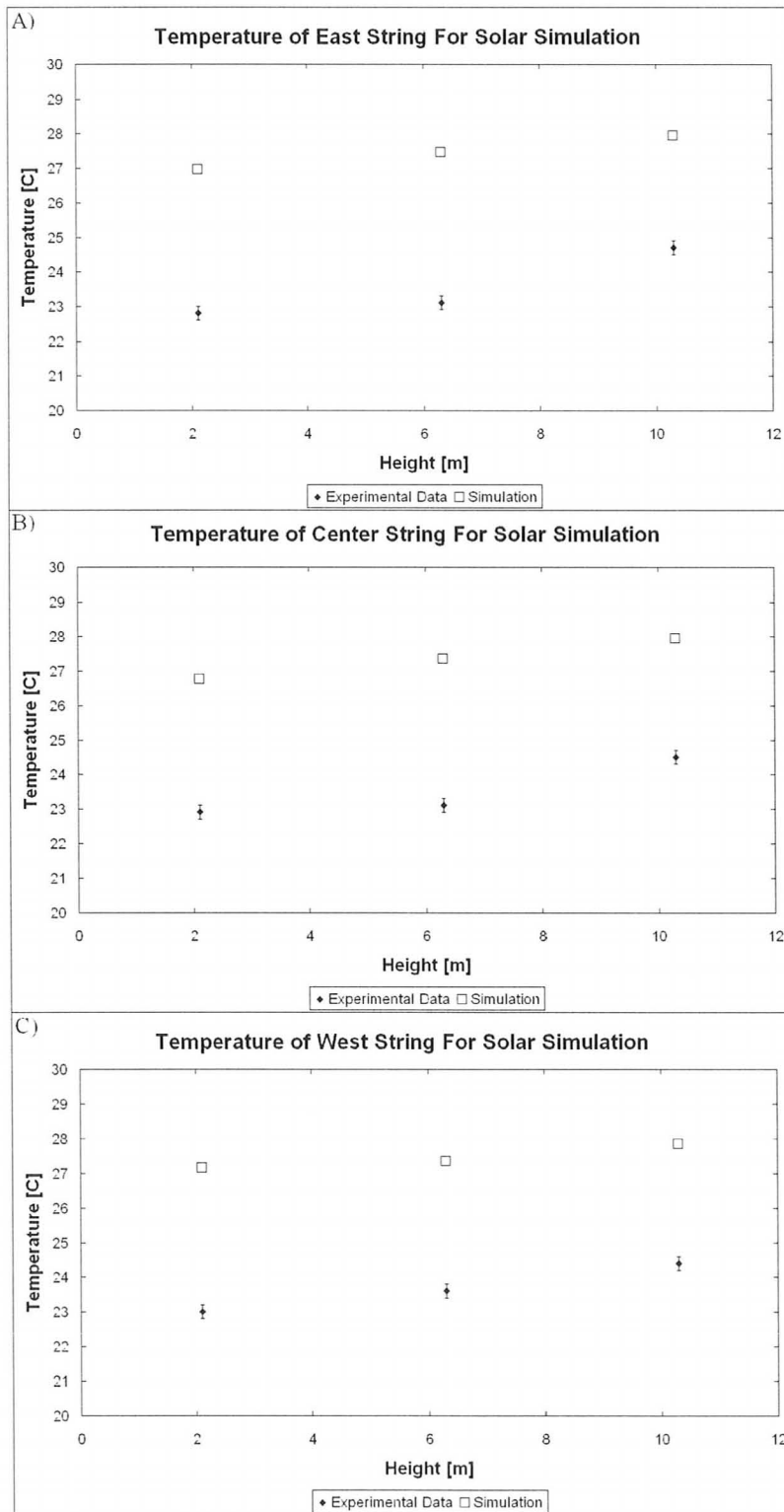


Figure 6.10 Temperature at Thermocouple Strings; A) East String, B) Center String, C) West String

The amount of stratification, the temperature difference between the top and bottom thermocouple of each string of thermocouples, is also an important measurement, a comparison of which is shown in Figure 6.11 below.

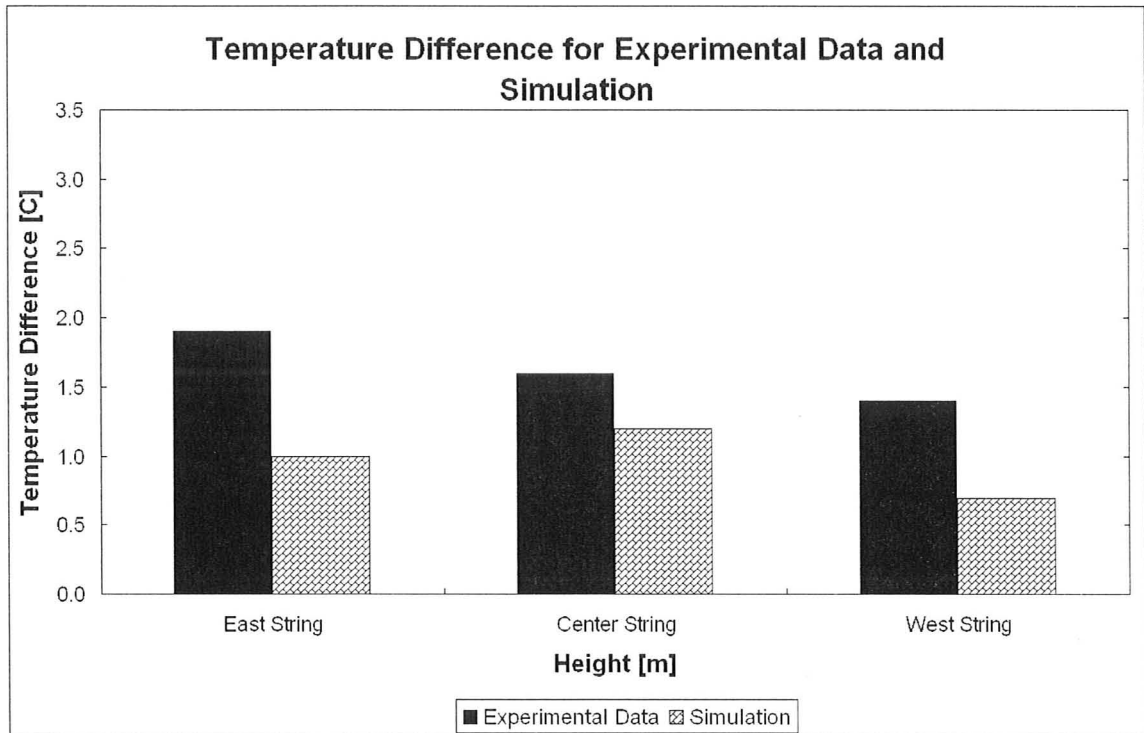


Figure 6.11 Comparison of Temperature Difference

Velocity Field

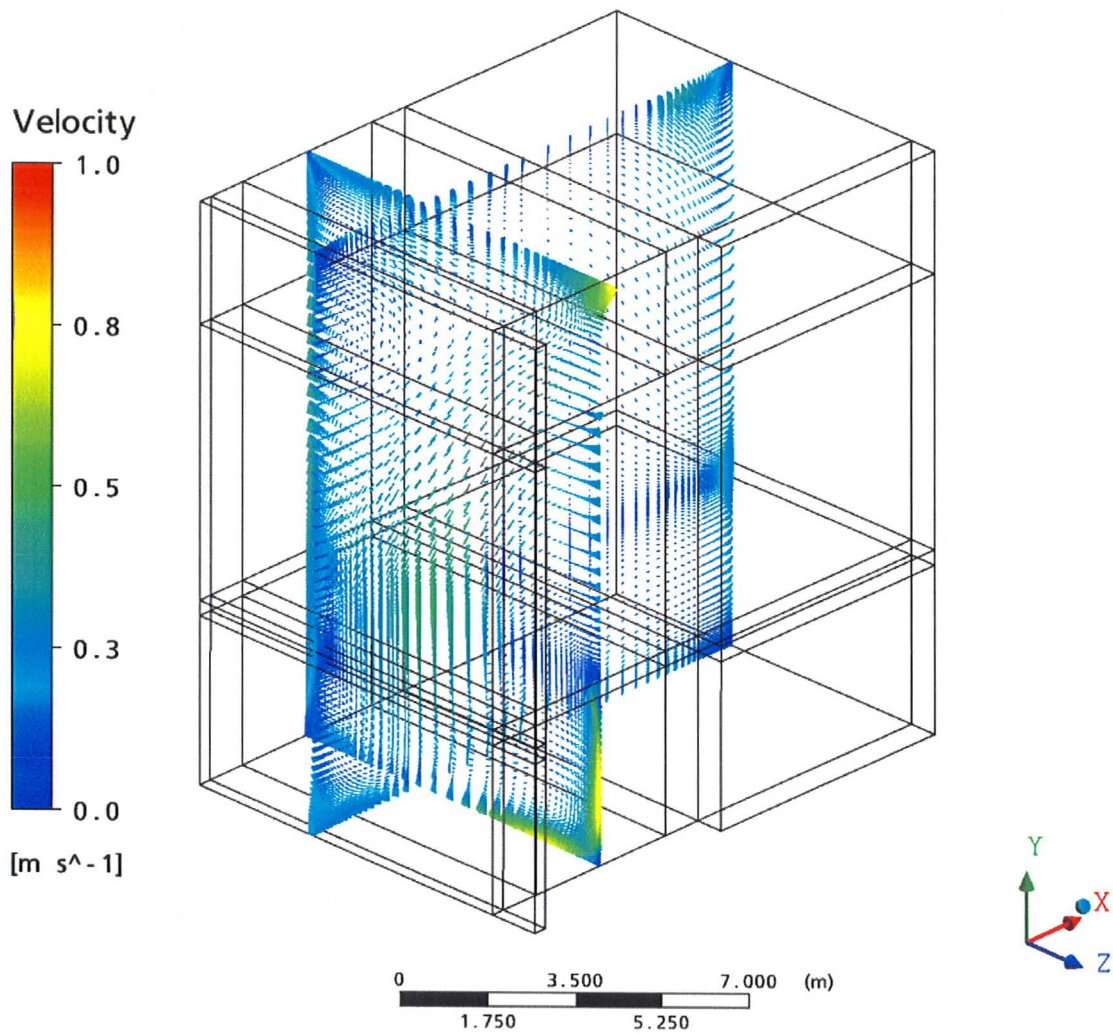


Figure 6.12 Velocity Vector Plots for Solar Simulation

Heat Flow

Figure 6.13 shows the heat flow for each of the boundaries for the standard solar simulation, broken down by type.

Heat Flow for Solar Simulation

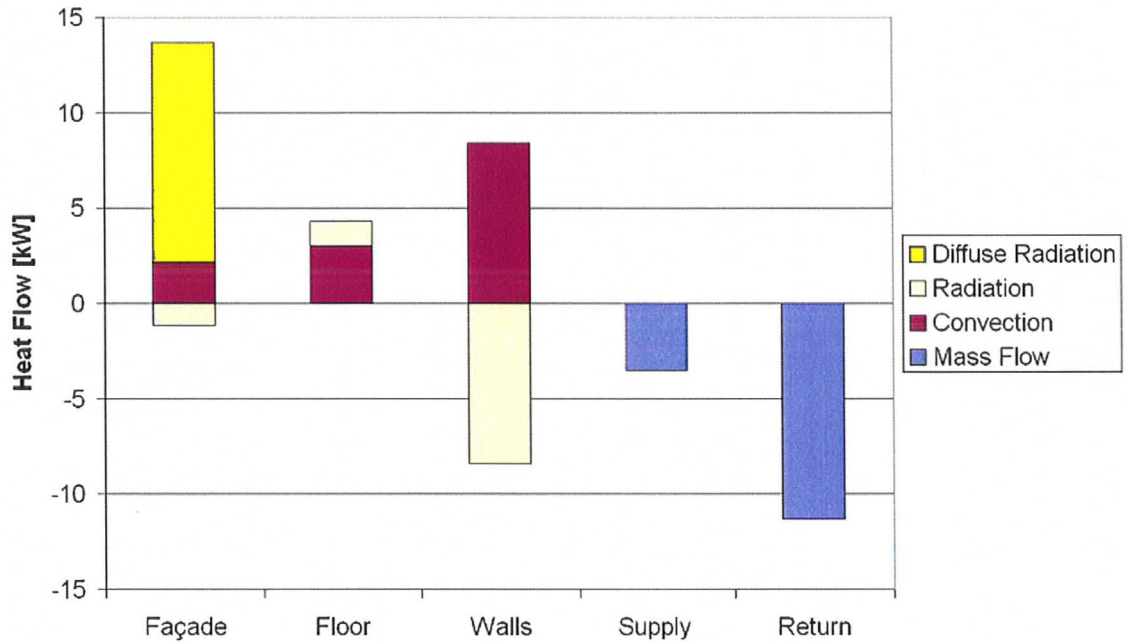


Figure 6.13 Heat Flow at Each Boundary of the Standard Simulation

Discussion:

Grid Independence

Grid independence was determined using the temperature along the thermocouple strings described in the measurement section of this chapter. Figure 6.14 shows the temperature for all of the strings compared with the results from the grid independence mesh. The GI strings are the results from the mesh with smaller grid spacing.

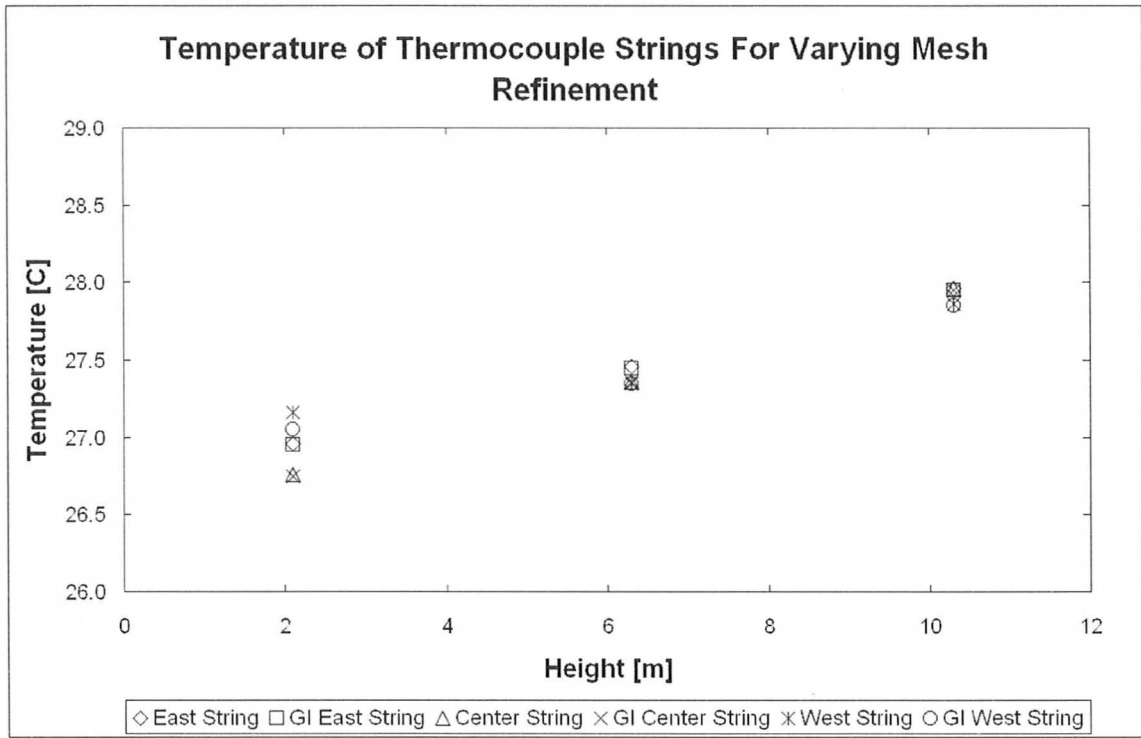


Figure 6.14 Temperature at Thermocouples for Varying Levels of Mesh Refinement

The largest difference was a tenth of a degree, located at the lowest level of the west thermocouple string. Figure 6.15 shows the temperature profile of the YZ Plane which intersects the central string, the thermocouple locations being shown by the yellow crosses.

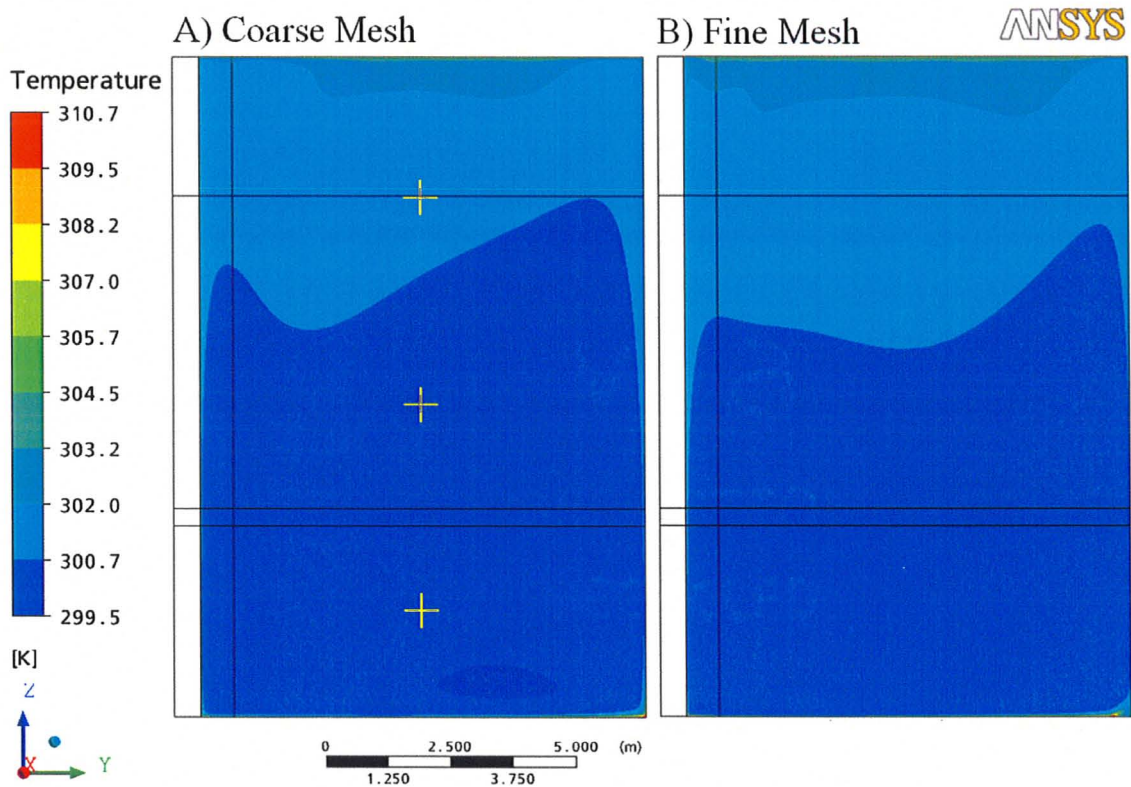


Figure 6.15 Temperature Profiles for Varying Mesh Refinement

Under Relaxation

Under relaxation was necessary for the simulations to converge, in the same manner as the turbulent natural convection simulations. It was discovered that the correct relaxation factor was independent of the use of radiation or of the use of heat flux boundary conditions. A relaxation factor of 0.9 proved universally correct provided the turbulence model and mesh were constant.

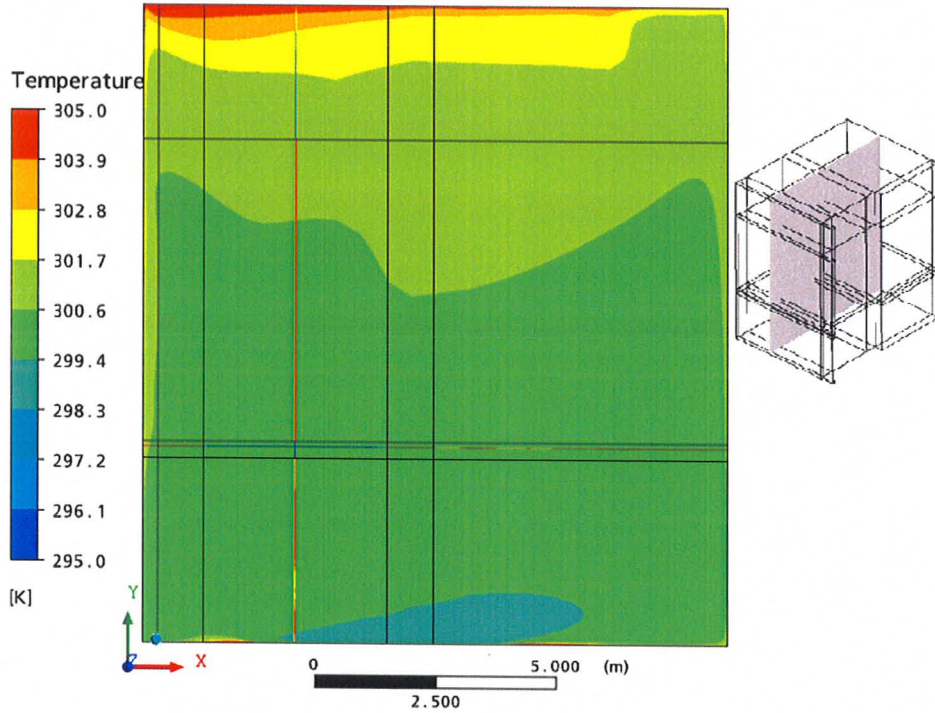
Temperature

One of the primary interests is the temperature field within the atrium. Figure 6.8 shows the general temperature field in the atrium along three planes, with the YZ and XZ planes intersecting the supply. The simulation over predicted the temperature at the

thermocouples by an average of 3.9°C. This was expected because the boundary conditions used restricted the flow of heat from the atrium. Adiabatic walls prevent heat escaping from the atrium. Most significantly the north end of the atrium was modeled as an adiabatic wall instead of allowing air to flow between the atrium and the connected corridors; this limited natural ventilation and prevented heat flow through the north end of the atrium. The only methods available for energy to leave the atrium are by the airflow through the return or heat loss through the façade. In these simulations the convection heat flow is positive because the air is cooler than the façade. Therefore, to balance the energy gained from the sun the air flowing through the return is the only option and this means the air must be hotter. The floor is the hottest region of the atrium, specifically where the heat fluxes are applied to simulate sunlight. If the same temperature range had been used for the floor in Figure 6.8 as the air in Figure 6.7 the floor would be almost entirely red. This is further supported by Figure 6.12, which shows that the floor is the only surface with a positive radiative heat flux and is therefore, the hottest surface. Given the floor's temperature of 77°C under the sunlight, the simulation is likely over predicting the floor's temperature. This is probably a result of the air and other walls being excessively hot as well. The stratification of the atrium was under predicted as shown by the lower values of ΔT for the simulation than the experimental data in Figure 6.10. The average error in ΔT for the thermocouple strings is 41%, based on the experimental ΔT . Nonetheless, the temperature profiles shown in Figure 6.8 show that the simulation produced stratification. Figure 6.16 shows the temperature profiles for the XY and XZ plane from Figure 6.8 in more detail.



A)



B)

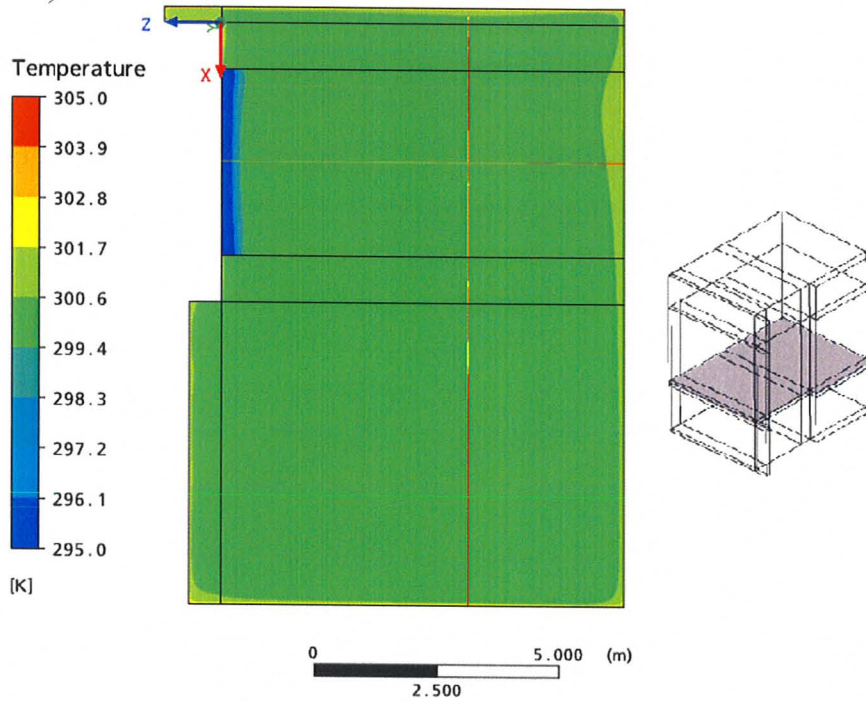


Figure 6.16 Temperature Profile in Atrium; A) XY plane, B) XZ plane

Figure 6.16A shows that as expected the temperature rises with the height of the atrium. Figure 6.16B shows that at a given height there is a nearly constant temperature, with the exception of the air coming from the supply.

Velocity Field

The velocity fields are also of interest because of how they effect thermal comfort. Figure 6.12 shows the velocity vectors along the XY and YZ planes shown in Figure 6.7. The velocity field produced by the simulation shows a strong relationship between air temperature and velocity. This suggests that despite the mechanical ventilation, natural convection is dominating the velocity field. Figure 6.17 show the velocity and temperature fields on an YZ plane which intersects with the middle of the supply and return.

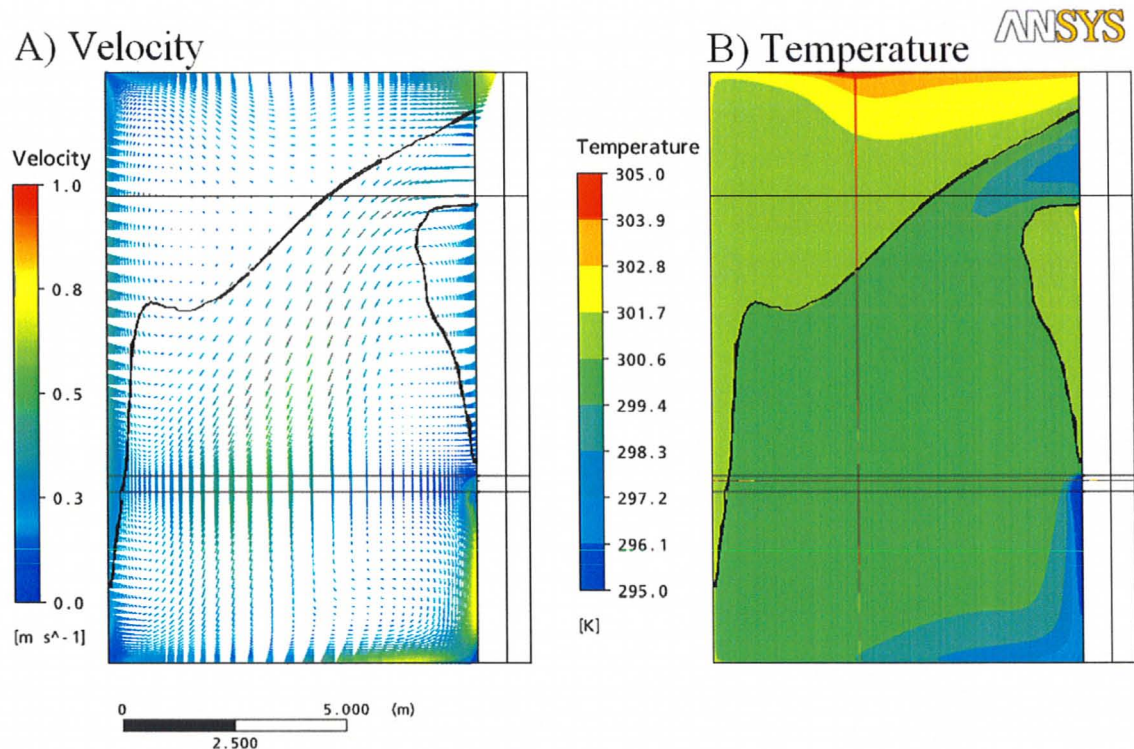


Figure 6.17 Velocity and Temperature Field Comparison; A) Velocity, B) Temperature

Notice in figure 6.17B the region outlined in black, which had a lower temperature than the air immediately surrounding it. The same region of the velocity vector plot show velocities in a downward direction. Except where the air meets the even cooler supply air, shown by the area of dark blue. Similarly the supply air drops to the bottom of the atrium, despite its velocity only in the negative z direction. The region around the supply produces some of the highest velocities in the atrium.

Heat Flow

Figure 6.13 shows the heat flow through each of the boundaries of the atrium. It should be noted that the walls are acting as predicting in Chapter 4. They are converting a radiation heat flux from hotter walls and diffuse radiation sources to a convection heat flux to the air. Also, the largest source of energy is from the solar radiation, both the diffuse radiation from the blinds and the heat flux on the atrium's floor. The largest of the two is the diffuse radiation sources along the blinds with a heat flow of 11.6 kW. The heat flux from the floor is from the solar radiation that passes through the façade and accounts for 4.3 kW.

Conclusions:

The absolute temperatures in the atrium were over predicted. The temperature stratification, however, was under predicted but was clearly present. There was also a clear relationship between velocity and temperature.

6.2.2 Façade Emissivities Simulations

Motivation:

The standard simulations assumed that the thermal radiation emitted from the blinds was as significant as the convection transfer to the air and therefore the emissivity of the façade would potentially have a significant effect on the amount of energy that enters the atrium. In order to determine the effect that emissivity has the emissivity of the façade was adjusted. It should be noted that Figure 6.12 shows that the blinds actually have a negative net radiation flux which means that they are not the hottest wall and absorb more radiation than they provide. However, by changing the emissivity the heat flux from the façade should still change.

Modifications:

The emissivity of the façade was changed to two different values. These were 0.5 and 0.8. All other emissivities were unchanged.

Results:

Figure 6.18 shows the temperature predictions of the simulation using various values of $\varepsilon_{\text{Façade}}$.

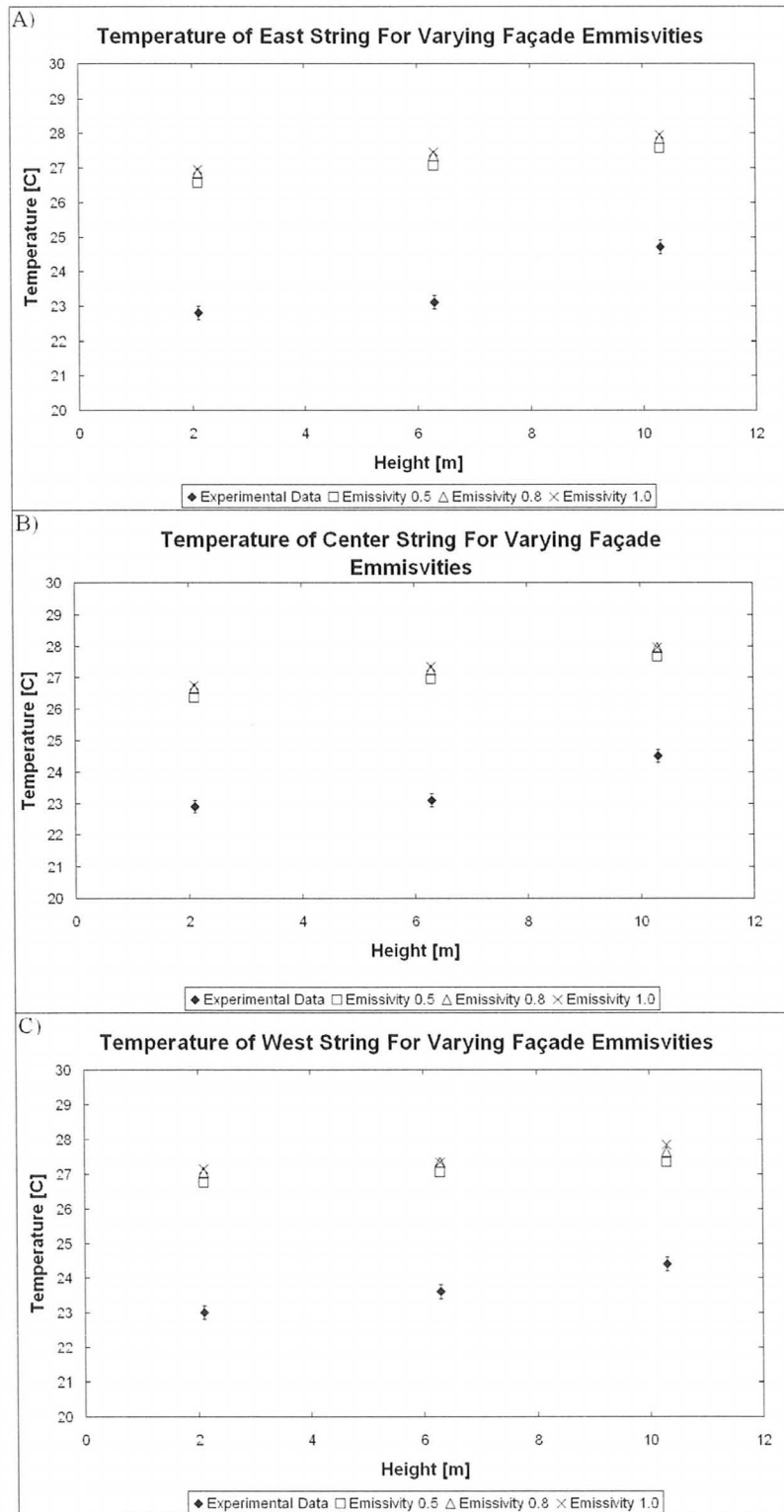


Figure 6.18 Temperature at Thermocouple Strings for Varying Façade Emissivities; A) East String, B) Center String, C) West String

Figure 6.19 plots the temperature difference for each façade emissivity.

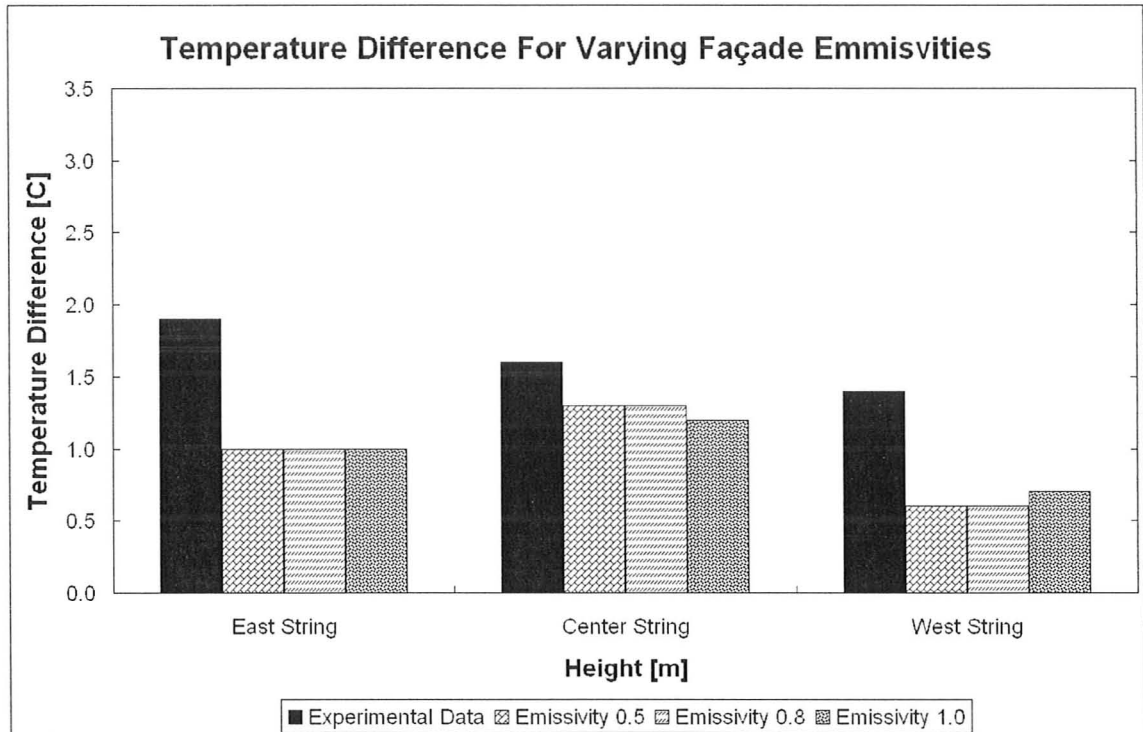


Figure 6.19 ΔT for Varying Façade Emmissivities

Discussion:

Figure 6.18 and 6.19 shows that the temperature field and stratification is essentially insensitive to the emissivity of the façade. None of the ΔT values changes by more than one tenth of a degree. None of the temperatures changes by more than one half of a degree. Figure 6.20 shows this trend clearly by plotting the temperatures along the central string versus the façade's emissivity.

Temperature of Central String as a Function of Façade Emissivity

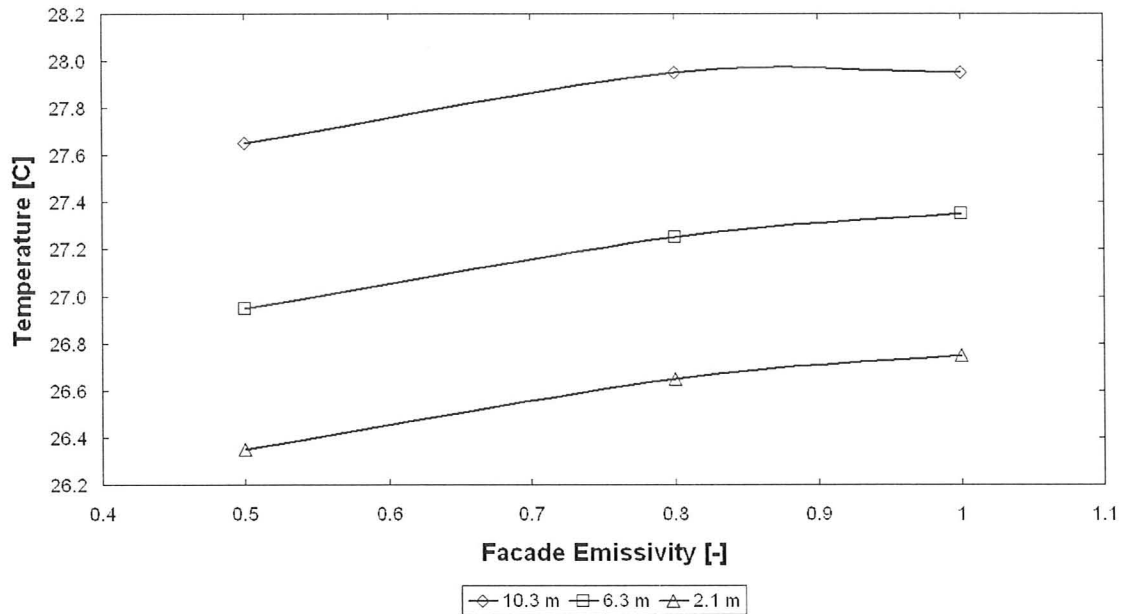


Figure 6.20 Center String Temperature vs. Façade Emissivity

There is a reduction in temperature as the emissivity drops, as would be expected since the same façade temperature would produce a smaller heat flux. However, at this level of solar radiation the thermal radiation from the blinds is insignificant. The magnitude is less than a tenth of the diffuse radiation sources along the façade. Therefore, even a drastic reduction in the thermal radiation provided by the blinds did not significantly affect the temperature in the atrium.

6.2.3 Solar Radiation Flux Simulations

Motivation:

One of the uncertain values in the simulation was the magnitude of the solar radiation. The simulations used the estimation of the average solar radiation heat flux of 1370 W/m^2 given by Wieder [1982]. This is based on the optimal solar radiation. Factors such as the reflectivity of the façade's surface and attenuation from the atmospheric conditions will change the actual value. Therefore, the sensitivity of the simulation to the magnitude of solar radiation must be determined.

Modifications:

The boundary conditions were the same as the standard solar simulation with only the variable SI adjusted to change the solar heat flux magnitude used. The solar radiation magnitudes used were 75%, 50%, 25% and 0% of the standard value of 1370 W/m^2 .

Results:

Figure 6.21 shows the temperature results for the experimental results of four solar radiation flux simulations as well as the standard simulation with 100% SI.

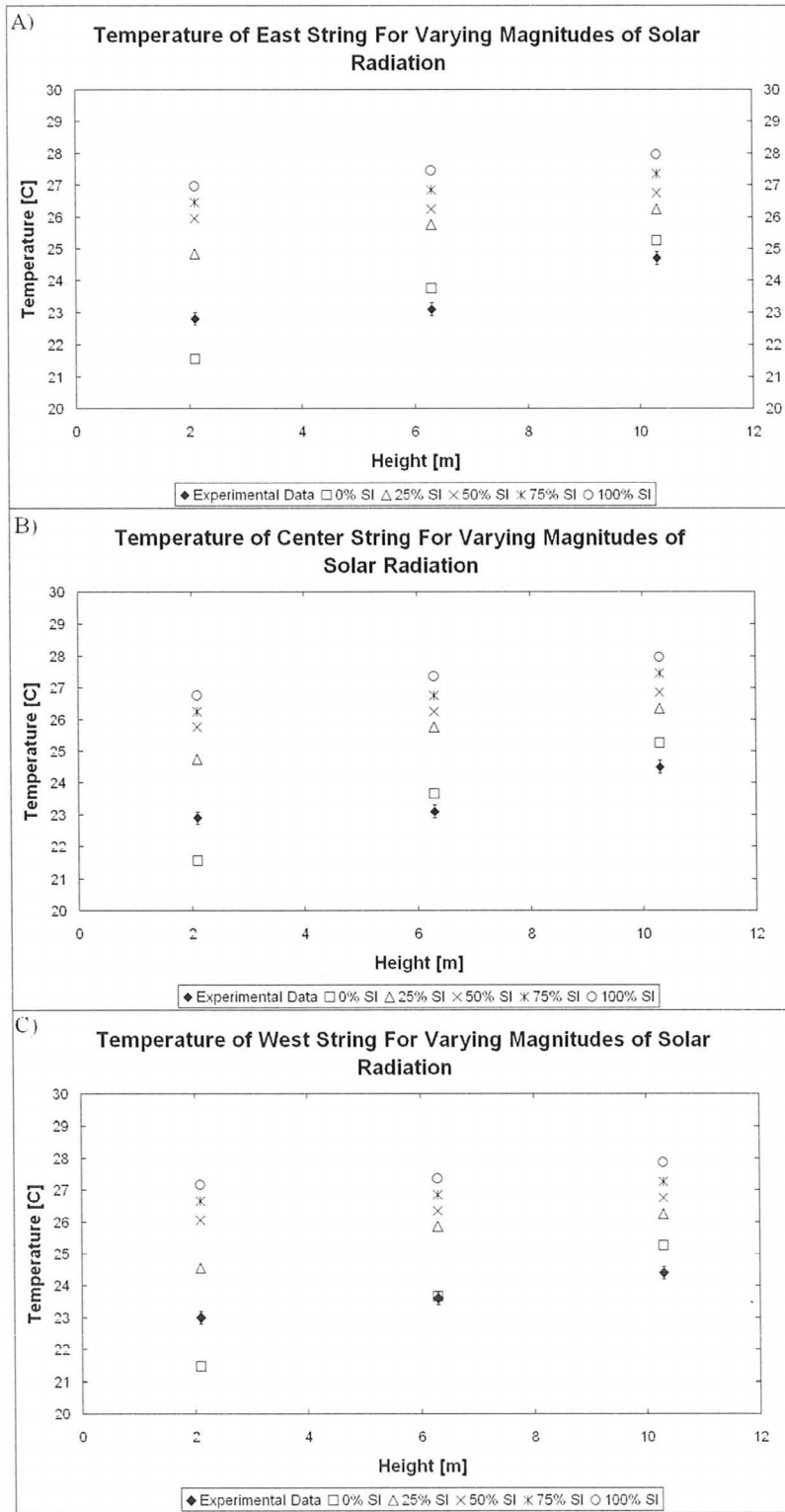


Figure 6.21 Temperatures at Thermocouple Strings for Varying Solar Radiation Magnitudes; A) East String, B) Center String, C) West String

Figure 6.22 shows the ΔT values for each level of solar radiation.

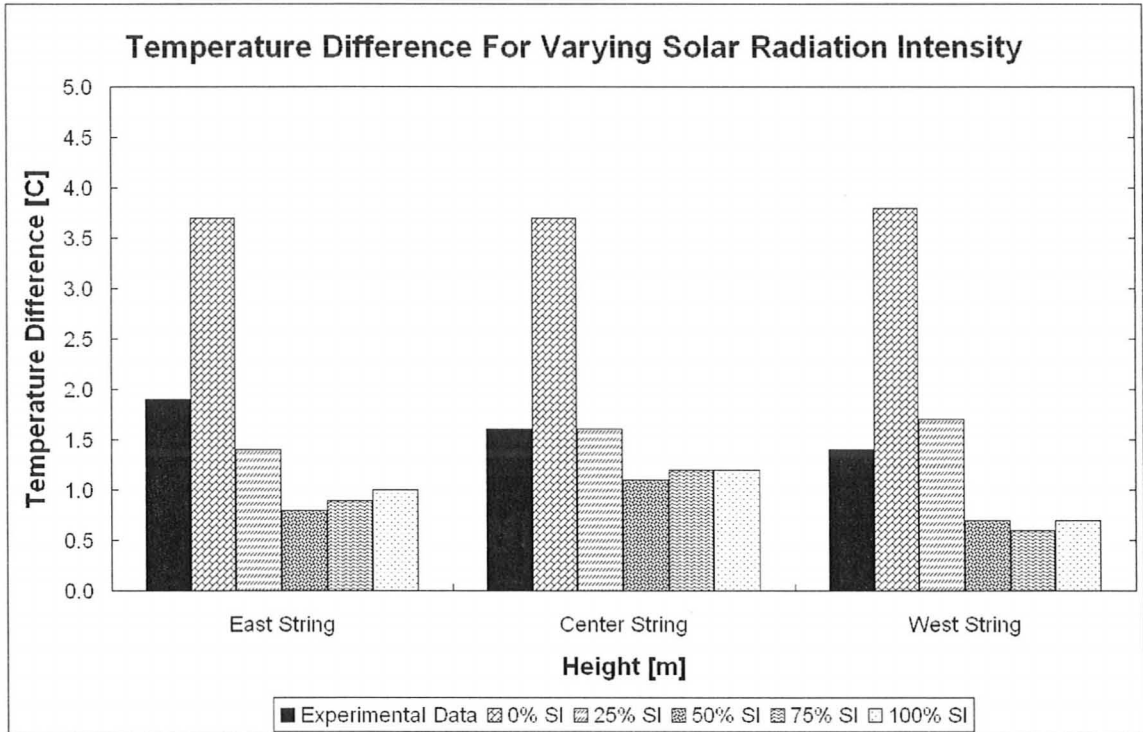


Figure 6.22 ΔT along Each Thermocouple String for Varying Solar Radiation Magnitudes

Discussion:

The reduction of solar energy shows a non linear relationship with simulated temperatures. Figure 6.23 below shows the temperature along the central thermocouple string as a function of solar radiation magnitude.

Temperature Along Central String as a Function of Solar Radiation Magnitude

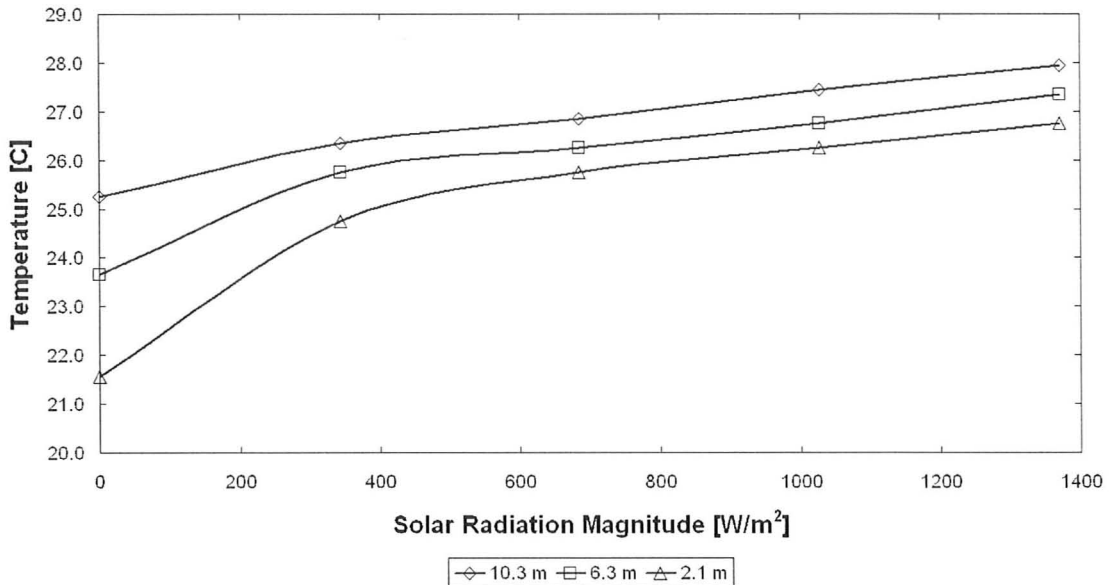


Figure 6.23 Temperatures along Center Thermocouple String vs. SI

The relationship between the temperature and the solar radiation magnitude is linear above the 25% magnitude. All other temperatures drop by approximately half of a degree with each reduction of 25%. Thus, the temperature magnitudes decrease but the temperature difference does not. However, at 25% of the solar magnitude or 343 W/m^2 the bottom temperature decreases by 1.0 K , twice that of the other temperatures.

Given the drop in energy input from the solar radiation a larger decrease in temperature would be expected. As can be seen in Figure 6.5 the diffuse solar radiation and floor heat flows, which are the direct result of the solar radiation, provide 15.8 kW of energy to make up 88% of the energy entering the atrium. When this is halved the temperature should be altered. At fifty percent of the standard solar radiation the highest temperature had only decreased by forty percent of what would be expected if it was a

perfectly linear relationship between temperature and solar radiation flux. Furthermore the middle and bottom temperature only decreased by thirty and twenty percent respectively. As mentioned before the temperature at the top of the atrium is responsible for energy leaving the atrium. As such, a small change in temperature should, on the surface, not allow for the considerable drop in energy input. On closer inspection the average temperature of the return for 25% of SI, 50% of SI and the standard simulation was 25.8°C, 26°C and 26.5 °C respectively. Given the average mass flow rate of the atrium of 0.42 kg/s such a small change in temperature does not account for the change in solar input. Figure 6.24 shows the energy balance for the 25% SI simulation.

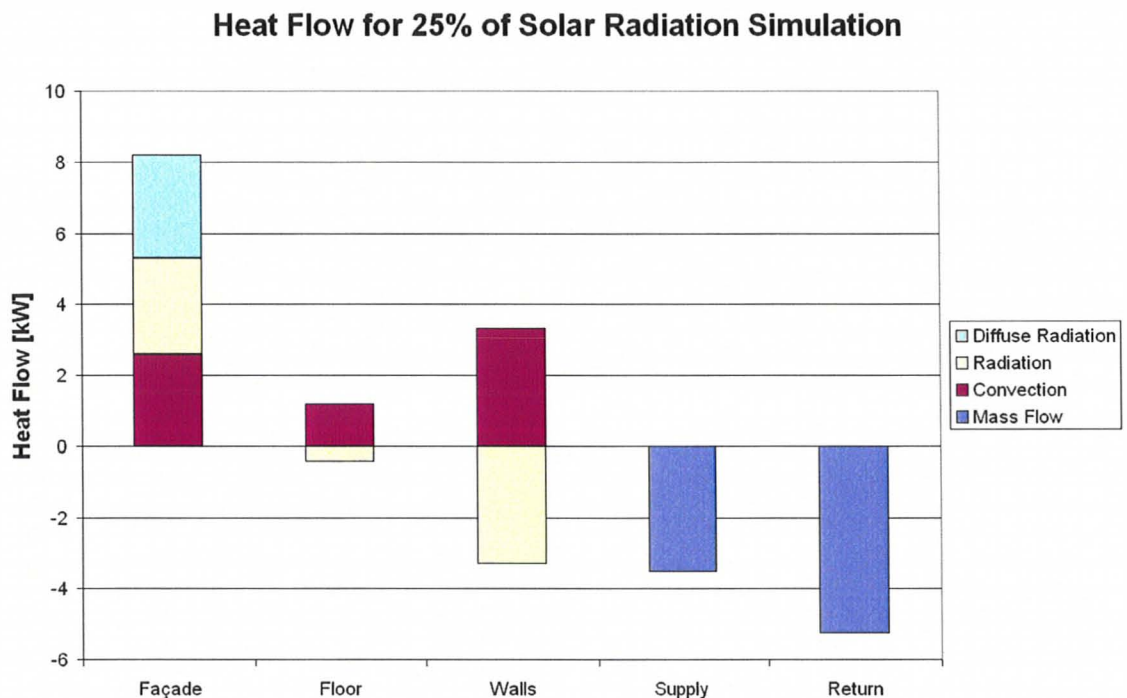


Figure 6.24 Heat flow at Each Boundary of Solar Simulation with 25% SI

Notice that despite the small drop in temperature, there is a significant drop in the return heat flow as compared to Figure 6.13. The reason for this difference is found in examining the heat flow of the return. The assumption of average temperature change being proportional to heat flow is based on an assumption of uniform velocity. Figure 6.25 shows the return's heat flux, temperature and velocity for several values of solar radiation flux.

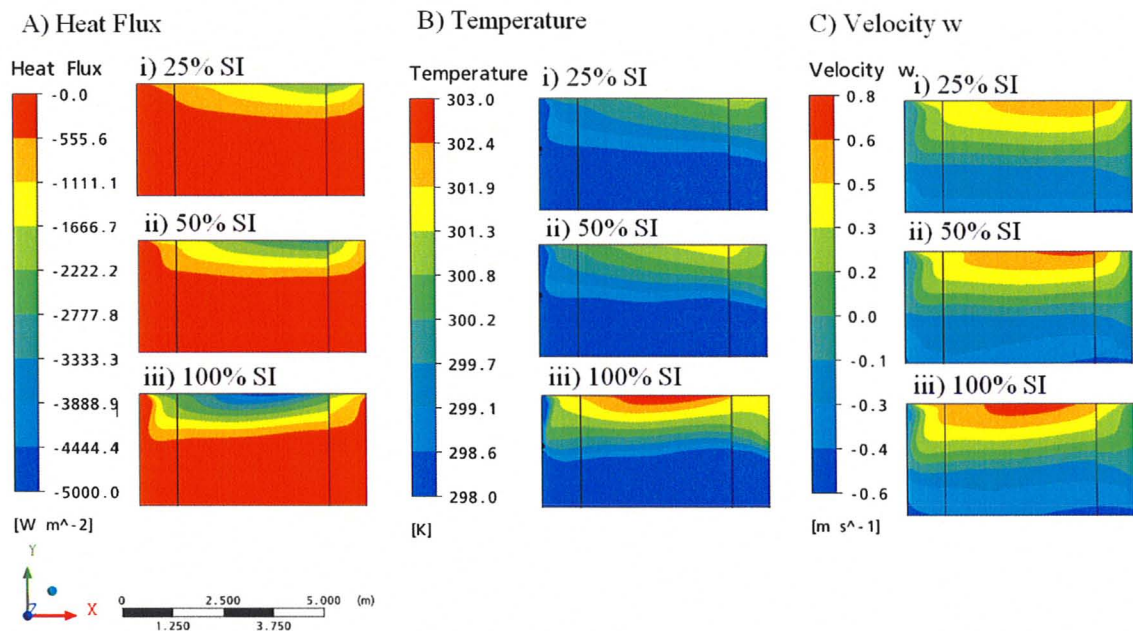


Figure 6.25 Results for Different Solar Radiation Magnitudes for; A) Heat Flux, B) Temperature and C) Velocity

Notice that the very high magnitudes of heat flux occur where the areas of high temperature and velocity occur. Essentially, as the atrium gets hotter the return concentrates the mass flow through a smaller area providing a much less uniform velocity profile. In addition, it begins to allow for air to flow back into the atrium at the lower

return boundary condition temperature. The simulation had effectively used a combination of velocity and temperature peaks to allow for a large change in heat flux with little effect on the average temperature of the return or the rest of the atrium.

Conclusion:

This section showed that the magnitude of the solar radiation was significant in determining the atrium's temperature field. Furthermore, it was shown that the relationship was not as simple as expected. This was due to the effect that solar radiation magnitude had on the velocity field, particularly near the return. A modest increase in velocity and the temperature allowed for much larger changes in heat flow through the return than would be suggested by the change in air temperature alone. Despite the smaller than expected change in temperatures the change in solar radiation flux had the most dramatic effect on the temperature field.

6.3 Conclusion

This chapter presented the results of a number of simulations of Concordia's atrium. These simulations were used to determine the simulation's sensitivity to the façade emissivity and the magnitude of solar radiation. The most realistic simulation captured two important features of an atrium; the temperature stratification and the importance of natural convection. The magnitudes of the temperatures were too high but this was expected given the limits of the known boundary conditions. i.e. the presumption of adiabatic internal walls and that the north end of the atrium was treated as an adiabatic wall. The amount of stratification was also in error by 25-50%. The experimental data indicated a stratification of 1.4 K to 1.9 K, compared to the simulation which predicted

stratification of 0.7 K to 1.2 K. The results proved insensitive to the façade emissivity because the radiation from the façade was minor when compared to the diffuse radiation source along the blinds and the solar radiation absorbed by the floor. The magnitude of solar radiation did have the most noticeable impact on both the temperature and stratification. The temperature at the thermocouples for the simulation with 25% SI dropped by an average of 1.8 K from the standard simulation. The stratification for the same simulation increased an average of 0.6 K, which decreased the error to 0.26%. The impact was less than expected due to the interaction of the velocity field and the temperature field, which allowed more energy to leave the atrium than would be accounted for by the change in temperature alone. Lastly, it was established that additional data would be required to establish a highly accurate simulation. Additional energy must be allowed to leave the atrium but it requires the data to impose a velocity profile on the north end of the atrium and make accurate assessments of the coefficients of heat transfer for the walls. Therefore, ANSYS CFX does capture the general trends in an atrium but requires much more detailed boundary condition information to obtain good quantitative results.

Chapter 7: Summary

7.1 Summary and Conclusions

This thesis considers the validation of ANSYS CFX for simulation of the heat transfer and fluid flow in atria. This was done, by validating several of the most important physical phenomena that influence atria. These included natural convection, radiation heat transfer and conjugate heat transfer. Finally, ANSYS CFX was used to simulate the working atrium located at Concordia University.

The validation of natural convection was performed for both laminar and turbulent conditions. The laminar natural convection showed excellent agreement with published benchmark results. For simulations of turbulent natural convection three different two-equation turbulence models were compared. The effectiveness of the buoyancy turbulence production model used to increase the turbulence in order to account for buoyant flows was also considered. For the turbulent simulations the $k-\epsilon$ model produced the worst results. The $k-\omega$ model and the SST model produced similar results with the $k-\omega$ model modeling the velocity profiles with greater accuracy and the SST model showing fewer errors in the average Nusselt numbers. However, based on the velocity peaks accuracy of the $k-\omega$ model and the additional time it took for the SST model to converge the $k-\omega$ model is recommended for further work.

The radiation validation was performed for two models; the Monte Carlo model and the Discrete Transfer model. The first validations used enclosures with either a fixed wall temperature or a fixed radiation heat flux since analytical solutions are readily

available. Generally, much better results were obtained with the Discrete Transfer model. The placement of the first node was also shown to be crucially important, as ANSYS CFX's tendency to try to average the node at the corner of two walls was the largest source of error. Otherwise, the accuracy was quite high. The final validations modeled solar radiation striking part of the floor of a cubic room. This was done initially to test the directional boundary radiation source option of the Monte Carlo model. However, it was shown that when it was used the simulation would not converge. Therefore, the validation was done in order to show an alternative method to account for directional radiation sources using the Discrete Transfer radiation model. This alternative method proved successful

The conjugate heat transfer validation used a horizontal channel with a heat source on the bottom of the channel. While the simulations did approximate the qualitative results, the temperature curves were somewhat displaced from the experimental results. The error in the curves decreased as the measurement location approached the conjugate heat transfer surface. This suggests that the problems may be related to modeling the air flow rather than the conjugate heat transfer. The stratification of the air in the channel was under predicted.

The atrium simulations were steady state, based on the data recorded on October 27, 2007 at Concordia's atrium. The blinds were partially closed and the hybrid ventilation turned off. The boundary conditions were created from the data recorded at the blinds when air temperature readings were taken. The standard simulation used full radiation modeling and accounted for solar radiation. Sensitivity to the boundary

conditions was tested. These tests included the façade's emissivity and solar radiation's magnitude. The façade's emissivity's effect was minimal because the long wave radiation from the façade's blinds was a minimal source of energy input. The solar radiation's intensity had a more noticeable effect; however, it was not as significant as expected. The best simulation over predicted the temperatures and under predicted the stratification. The over prediction of the temperatures was expected since the walls were adiabatic and no heat was allowed to escape through the north end of the atrium.

Therefore, ANSYS CFX was moderately successful in simulating atrium conditions. The qualitative trends were present, however, the absolute values of air temperatures were too high and the stratification was under estimated. These problems may be addressed by considering the recommendations for further work included below, mainly by making the simulation transient and by finding better boundary conditions for the north end of the atrium.

7.2 Recommendations for Further Work

a) Transient Simulations

Transient elements such as thermal mass may be influential in determining the conditions in an atrium. Transient simulations were omitted from this thesis in order to establish the viability of steady state solutions

b) North End Boundary Conditions

A more realistic boundary condition for the north end of the atrium should be found. The current method of using a wall limits the possibility of natural ventilation.

The most obvious solution of using an opening is explored in Appendix H. Based on the work in Appendix H a specified velocity profile at the north end would be required. This boundary condition would require more detailed information to implement.

c) Reference Geometry

Determine how important the niches in the atrium geometry are to the final results. Their presence significantly increased the difficulty of meshing the atrium and if they could be omitted it would make for quicker simulations. Furthermore, it would simplify the process when using ANSYS CFX for different geometries.

d) Orientation

Determine the sensitivity of the simulation to the orientation of the sun, specifically the azimuth. The simulations made the assumption that the solar radiation only struck the floor and not the walls. This is only valid if the façade's orientation and the sun's orientation is identical.

e) Seasonal Changes

Consider the differences between the winter and summer months.

References

- Ampofo, F. & T.G. Karayiannis. (2003). Experimental benchmark data for turbulent natural convection in an air filled square cavity. International Journal of Heat and Mass Transfer. 46. 3551-3572
- ANSYS CFX. “CEL Functions”. *ANSYS CFX Reference Guide*. 2006
- ANSYS CFX. “Comparison of the Radiation Models”. *ANSYS CFX Reference Guide*. 2006
- ANSYS CFX. “Discrete Transfer Model”. *ANSYS CFX Reference Guide*. 2006
- ANSYS CFX. “Guidelines for Mesh Generation”. *ANSYS CFX Reference Guide*. 2006
- ANSYS CFX. “Hybrid and Conservative Variables”. *ANSYS CFX Reference Guide*. 2006
- ANSYS CFX. “Lists of Symbols”. *ANSYS CFX Reference Guide*. 2006
- ANSYS CFX. “Mathematical Formulation”. *ANSYS CFX Reference Guide*. 2006
- ANSYS CFX. “Model Selection and Application”. *ANSYS CFX Reference Guide*. 2006
- ANSYS CFX. “Near Wall Treatment”. *ANSYS CFX Reference Guide*. 2006
- ANSYS CFX. “Numerical Errors”. *ANSYS CFX Reference Guide*. 2006
- ANSYS CFX. “Radiation Modeling”. *ANSYS CFX Reference Guide*. 2006
- ANSYS CFX. “Radiation Transport”. *ANSYS CFX Reference Guide*. 2006
- ANSYS CFX. “The k- ϵ Model”. *ANSYS CFX Reference Guide*. 2006
- ANSYS CFX. “Two Equation Turbulence Models”. *ANSYS CFX Reference Guide*. 2006
- ANSYS CFX. “Wall Heat Transfer”. *ANSYS CFX-Solver Modeling Guide*. 2006
- ASHRAE, (2005), ASHRAE Handbook-Fundamentals(SI), Atlanta: American Society of Heating, Refrigerating and Air-Conditioning Engineers, Inc.: Atlanta

- Bahador, M.N. & A.M. Sayigh (1979). Solar Thermal Energy Storage Systems. Solar Energy Applications in Buildings. (ed. A.M. Sayigh). pp.81-104. New York: Academic Press, Inc. 1979.
- Breesch, H., Bossaer, A. & A. Janssens. (2005). Passive cooling in a low-energy office building. Solar Energy.79. 682-696.
- Bowman, N.T., Eppel, H., Lomas, K.J. Robinson, D.& M.J. Cook. (2000).Passive Draught Evaporative Cooling. Indoor Built Environment. 9. 284-290.
- Chiu, W.K.S., Richards, C.J. & Y. Jaluria. (2001). Experimental and Numerical Study of Conjugate heat Transfer in a Horizontal Channel Heated From Below. Journal of Heat Transfer. 123:668-697.
- Chow, W.K, & C.L. Chow. (2005). Evacuation with smoke control for atria in green sustainable buildings. Building and Environment.40. 195-200
- City of Montreal. Ville de Montréal - Les attraits - Montréal in the world.
http://ville.montreal.qc.ca/portal/page?_dad=portal&_pageid=66,1211449&_schema=PORTAL. Accessed: September 9, 2008.
- Davidson, L. & S.H. Peng. (2001). Large Eddy Simulation for Turbulent Buoyant Flow in a Confined Cavity. International Journal of Heat and Fluid. 22. 323-331
- Galasiu, AD & M.R. Atif.(2002). Applicability of daylighting computer modeling in real case studies: comparison between measured and simulated daylight availability and lighting consumption. Building and Environment. 37. 363-377
- Gan. G. & S.B. Riffat. (2004). CFD modelling of air flow and thermal performance of an atrium integrated with photovoltaics. Building and Environment. 39. 735-748
- Hanjalic, K. (1994). Advanced turbulence closure models: a view of current status and future projects. International Journal of Heat and Fluid Flow. 15. 178-203.
- Hiramatsu, T., T. Harada, S. Kato, S. Murakami & H. Yohino. Study of Environmental in Experimental Real-scale Atrium. *5th International Conference on Air Distribution in Rooms*. July, 1996
- Henkes, R.A.W.M. & C.J. Hoogendoorn. (1995). Comparison exercise for computations of turbulent natural convection in enclosures. Numerical Heat Transfer. Part B. 28. 59-78 .
- Holford, J.M. & G.R. Hunt. (2003). Fundamental atrium design for natural ventilation. Building and Environment. 38. 409-426.

- Hortmann, M., Peric, M. & Scheuerer, G. (1990). Finite volume multigrid prediction of laminar natural-convection- bench-mark solutions. International Journal for Numerical Methods in Fluids. 11. 189-207.
- Ibanez, M. Lazaro, A., Zalba, B. & L.F. Cabeza. (2005). An approach to the simulation of PCMs in building application using TRNSYS. Applied Thermal Engineering. 25. 1796-1807
- Incropera, F.P. and DeWitt, D.P. (2002). Introduction to Heat Transfer. (4th ed.). John Wiley & Sons: New York
- International Energy Agency. (1996). Atrium Models for the Analysis of Thermal Comfort and Energy Use. Trondheim, Norway. Author.
- Lauder, B.E. & Spalding D.B. (1973). The Numerical Computation of Turbulent Flows. Computer Methods in Applied Mechanics and Engineering. 3. 269-289
- Lawand, T.A. & B. Saulnier. “Some Solar-Heated Buildings in Canada”. *Solar Energy Application in Buildings*. pp.253-277. New York: Academic Press, Inc. 1979
- Menter, F.R. (1996). A Comparison of Some Recent Eddy-Viscosity Turbulence Models. Journal of Fluid Engineering. 118. 514-519
- Ozeki, Y., S. Kato & S. Murakami. (1996). Numerical Analysis on Flow and Temperature Fields in Experimental Real Scale Atrium. *5th International Conference on Air Distribution in Rooms*. July 1996.
- Pappas, A. & Z. Zhai. (2008). Numerical investigation on thermal performance and correlations of double skin façade with buoyancy-driven airflow. Energy and Buildings. 40. 466-475.
- Pfafferott, J., Herkel, S. & M. Wambsganss. (2004). Design, monitoring and evaluation of a low energy office building with passive solar cooling by night ventilation. Energy and Buildings. 36. 455-465
- Pfrommer, P, Loman, K.J. & Seale, C. (1995). The radiation transfer through coated and tinted glazing. Solar Energy. 54. 287-299
- Siegel R. & Howell, J.R. (1981). Thermal Radiation Heat Transfer. (2nd Ed.) McGraw-Hill Book Company: Washington.

- Tan, G. & Glicksman, L.R. (2005). Application of integrating multi-zone model with CFD simulation to natural ventilation prediction. Energy and Buildings. 37.1049-1057
- Voeltzel, A., Carrie, FR., & G. Guarracino. (2001). Thermal and ventilation modelling of large highly-glazed spaces. Energy and Buildings. 33.121-132
- Wall, M. (1997). Distribution of solar radiation in glazed spaces and adjacent buildings. A comparison of simulation programs. Energy and Buildings. 26. 129-135.
- Wang, C. & Huang, H. (2004). A study in the Procedure of Decision-Making for Entrance Architecture of Modern MRT Station in Taiwan. Journal of Asian Architecture and Building Engineering.3. 320-326
- Wieder, S. (1982). An Introduction to Solar Energy for Scientists and Engineers. John Wiley & Sons: New York.
- Wilcox, D.C. (1993). “Comparison of Two Equation Turbulence Models for Boundary Layer s with Pressure Gradient” in AIAA Journal. 31. 1414-1421

Appendix A: Two Dimensional Domains in ANSYS CFX

It should be noted that in ANSYS CFX it is impossible to create and mesh a two dimensional domain. However, two dimensional results are common in the experimental data and analytical solutions used to validate CFD code. This was handled by making the domain's width in the dimension neglected one tenth of the smallest scale in either of the other directions. Figure A.1 shows how the domain actually appears in three dimensions, where z represents the dimension that is being neglected in the two dimensional assumption.

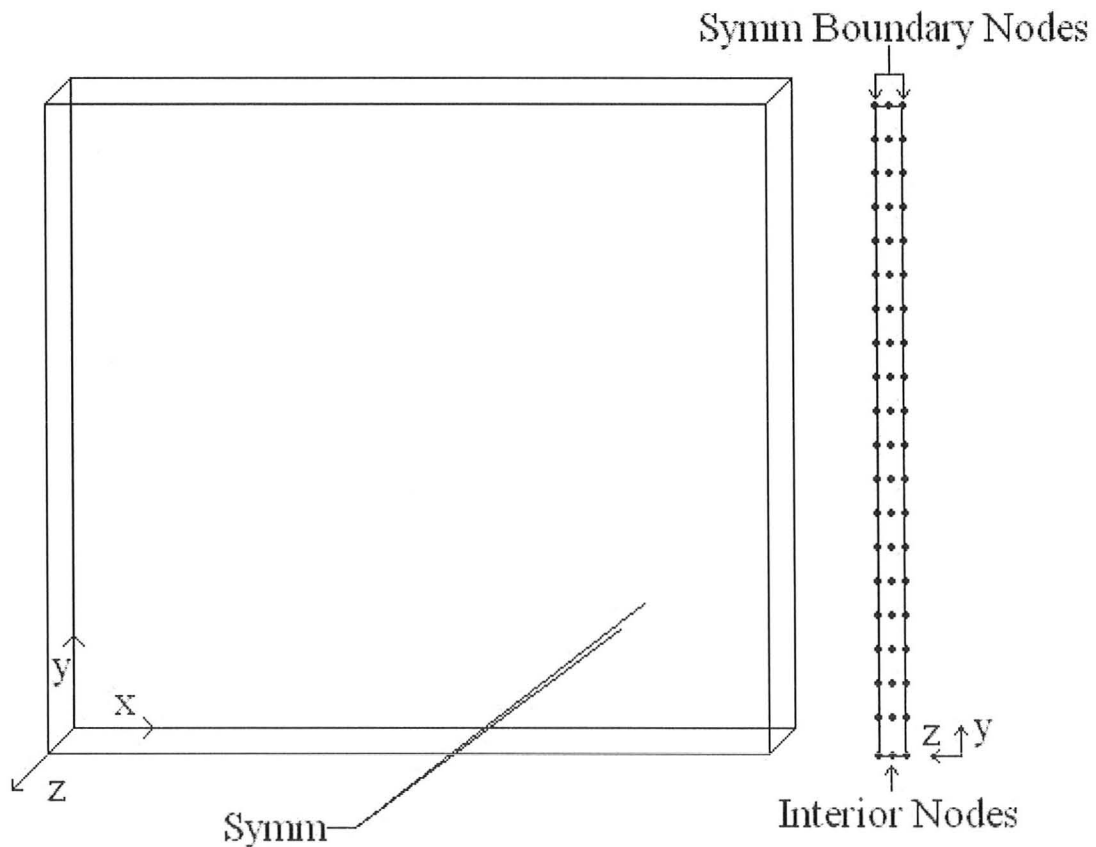


Figure A.1 Actual Three Dimensional Domain Used in Two Dimensional Simulations and Cross Section of Nodes in z Direction Mesh.

Meshing this domain and maintaining two-dimensional behaviour requires the use of the symmetry boundary condition. The mesh in the z direction is limited to three nodes and the boundary areas, denoted by SYM in Figure A.1, are assigned the aforementioned symmetry boundary condition. This boundary condition sets the partial derivatives of the variables in the z direction to zero. This means that the interior node next to the symmetry boundary condition has the same value as the node at the boundary. Since there are only three nodes, two exist on a boundary there is only one interior node that must be the same as both adjacent symmetry boundary nodes. This requires that all three nodes have the value for all variables so there is no variation in the z direction. Therefore, two dimensional behaviour is maintained.

Appendix B: Extrapolation Equations

With a sufficient number of simulations it is possible to extrapolate what the solution to a simulation would be with an infinite number of nodes. By assuming that the error in the calculation is proportional to the length between consecutive nodes raised to some power and by using three different lengths between consecutive nodes (Δx) the extrapolated value can be found. The three different lengths create a system of three equations with three unknowns, the proportional constant (A), the exponent (α) and the true value of the variable (T). If the error is replaced with the true value minus the calculated value (S) the true value can be calculated using the equations below:

$$T - S_1 = A(\Delta x_1)^\alpha \quad (\text{Equation. B.1})$$

$$T - S_2 = A(\Delta x_2)^\alpha \quad (\text{Equation. B.2})$$

$$T - S_3 = A(\Delta x_3)^\alpha \quad (\text{Equation. B.3})$$

If the grids are designed so that the lengths between consecutive nodes have the following relationship the system can be easily solved for the true value of the variable.

$$\Delta x_1 = 2\Delta x_2 \Rightarrow \frac{\Delta x_1}{\Delta x_2} = 2 \quad (\text{Equation. B.4})$$

$$\Delta x_2 = 2\Delta x_3 \Rightarrow \frac{\Delta x_2}{\Delta x_3} = 2 \quad (\text{Equation. B.5})$$

By dividing equation B.1 by equation B.2 and equation B.2 by equation B.3 the variable A can be eliminated and equation B.6 and B.7 formed.

$$\frac{T - S_1}{T - S_2} = \left(\frac{\Delta x_1}{\Delta x_2} \right)^\alpha \quad (\text{Equation B.6})$$

$$\frac{T - S_2}{T - S_3} = \left(\frac{\Delta x_2}{\Delta x_3} \right)^\alpha \quad (\text{Equation B.7})$$

Then take the natural logarithm of both sides of equations B.6 and B.7 to bring the exponent α down and then divide equation B.6 by equation B.7 to eliminate it. A single equation B.8 is created with the only unknown being the true value of the variable. This variable then can be isolated using the properties of logarithms, exponents and the previously discussed relationships of the lengths between the consecutive nodes.

$$\frac{\ln\left(\frac{T - S_1}{T - S_2}\right)}{\ln\left(\frac{T - S_2}{T - S_3}\right)} = \frac{\alpha \ln\left(\frac{\Delta x_1}{\Delta x_2}\right)}{\alpha \ln\left(\frac{\Delta x_2}{\Delta x_3}\right)} \Rightarrow \ln\left(\frac{T - S_1}{T - S_2}\right) \ln\left(\frac{\Delta x_2}{\Delta x_3}\right) = \ln\left(\frac{T - S_2}{T - S_3}\right) \ln\left(\frac{\Delta x_1}{\Delta x_2}\right) \quad (\text{Equation B.8})$$

$$\left(e^{\ln\left(\frac{T - S_1}{T - S_2}\right)} \right)^{\ln\left(\frac{\Delta x_2}{\Delta x_3}\right)} = \left(e^{\ln\left(\frac{T - S_2}{T - S_3}\right)} \right)^{\ln\left(\frac{\Delta x_1}{\Delta x_2}\right)} \Rightarrow \left(\left(\frac{T - S_1}{T - S_2} \right) \right)^{\ln\left(\frac{\Delta x_2}{\Delta x_3}\right)} = \left(\left(\frac{T - S_2}{T - S_3} \right) \right)^{\ln\left(\frac{\Delta x_1}{\Delta x_2}\right)} \quad (\text{Equation B.9})$$

Equation B.4 and B.5 mean that both exponents are identical so that they can be removed by taking both sides of equation to the inverse power. This produces equation B.10, which can be rearranged into equation B.11.

$$(T - S_1)(T - S_3) = (T - S_2)^2 \quad (\text{Equation B.10})$$

$$T = \frac{S_2^2 - S_1 S_3}{2S_2 - S_3 - S_1} \quad (\text{Equation B.11})$$

Similarly the exponent α can be solved for using previous equations and back substituting the true value.

$$\alpha = \frac{\ln\left(\frac{T - S_1}{T - S_2}\right)}{\ln\left(\frac{\Delta x_1}{\Delta x_2}\right)} \quad (\text{Equation. B.12})$$

Note that the extrapolated value relies on the accuracy of the equations B.1, B.2, and B.3. Those equations assume that the solution error is determined from the first neglected term in the Taylor series expansion. A sufficiently fine grid is required for that term to be the dominant term in the error equation. As such, that assumed form of the error is not valid for coarse grids.

Appendix C: Conservative and Hybrid Variables

ANSYS CFX is a finite volume difference solver, which is the reason for conservative and hybrid variables [ANSYS CFX, “Hybrid and Conservative Variables”, 2006]. The difference is in how a finite difference solver and a finite volume difference solver treats the nodes near the wall. Figure C.1 shows this difference.

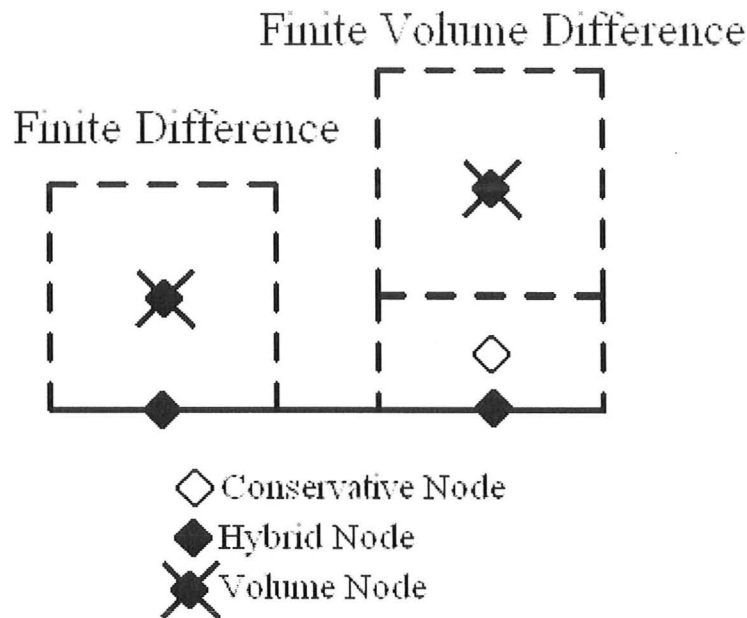


Figure C.1 Finite Difference and Finite Volume Difference Nodes at Wall Boundary.

Finite difference solvers have no volume around the boundary node and as such their boundary or hybrid node does not have any conservation equation, such as conservation of momentum, applied to its volume. The finite volume difference boundary node will have conservation equations applied because it has a volume associated with the node. However, if the boundary were a no slip wall then by using the boundary node value, i.e. the boundary condition, there would be no flow through the volume. To solve this ANSYS CFX uses the concept of a conservative variable which is used in the

conservation equations instead of the value of the boundary condition [ANSYS CFX, “Hybrid and Conservative Variables”, 2006]. In order to find this value they interpolate between the boundary node, or hybrid node and the volume node. Figure C.2 shows a rough approximation of the principle.

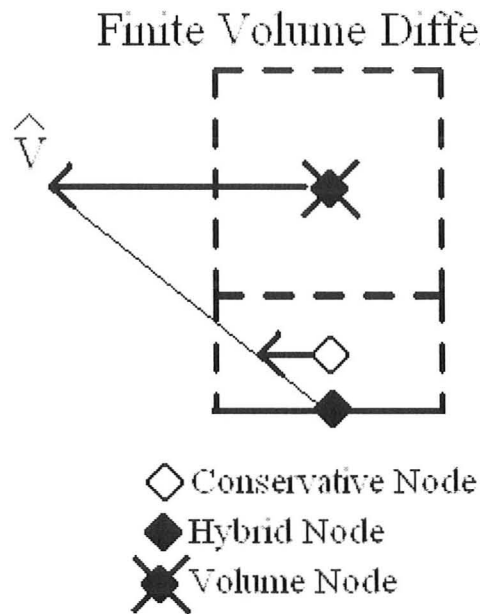


Figure C.2 Interpolation for Conservative Value

It should be noted that the conservative node is not part of the mesh. It is a concept rather than object. The hybrid value is the value assigned to the hybrid/boundary node based on the boundary conditions after the final solution is found for the simulation.

Appendix D: Radiation Heat Flux Boundary Conditions

Motivation:

During the radiation validation it was necessary to be able to input boundary conditions for radiation heat fluxes. This was done in two cases; the first where a total radiation heat flux had to be specified in order to validate CFX's ability to determine the correct wall temperature, the second when an external radiation source, i.e. solar rays, entered through an opening and struck a surface. This appendix shows that the boundary conditions used did produce the desired results

Methods:

In both cases the heat flux boundary condition was used. This boundary condition allows the user to specify the heat flux through the wall.

Analysis:

In CFX there are three heat flux variables that exist at a boundary wall; the wall convection heat flux (Q_{Con}), the wall radiative heat flux (Q_{Rad}) and the wall heat flux (Q_{BC}) [ANSYS CFX, Wall Heat Transfer, 2006]. Figure D.1 shows the diagram of the heat fluxes at the wall and compares them to the two situations we wish to emulate.

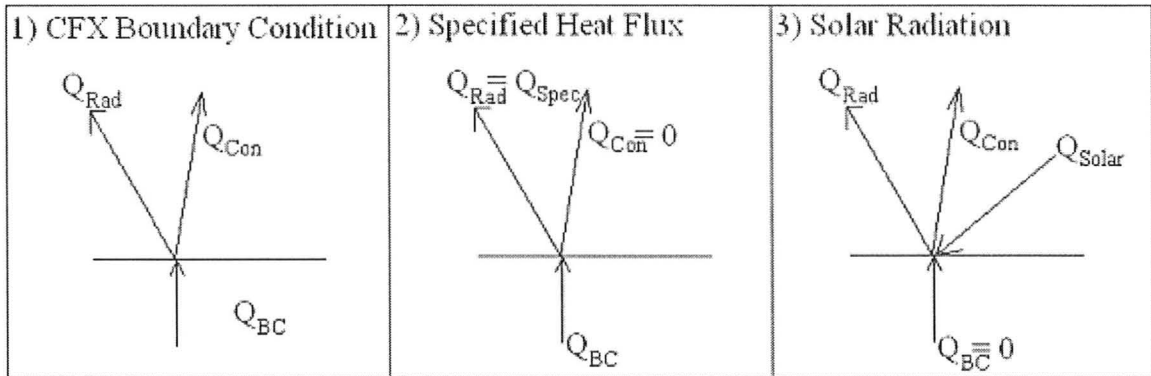


Figure D.1 Heat Fluxes at Boundary Wall

To simulate both situations in ANSYS CFX, a specified heat flux boundary conditions would be used so that Q_{BC} would be set to either Q_{Spec} or Q_{Solar} . It can be shown that this is equivalent to the other situations. To do this the energy balance at the boundary will be used as it is defined by CFX, which is shown in equation D.1 [ANSYS CFX, Wall Heat Transfer, 2006].

$$Q_{BC} = Q_{Rad} + Q_{Con} \quad (\text{Equation. D.1})$$

Specified Radiation Heat Flux

For the case where a specified wall radiative heat flux is desired, the wall convection heat flux is set to zero by setting the thermal conductivity of the material in the domain to zero or a very low number. When this is done for the Discrete Transfer radiation model the convection heat flux was at most 0.0006 percent of the radiative heat flux. This means we can treat Q_{Con} as insignificant. Equation D.2 shows the effect of removing the convection heat flux from the equation.

$$Q_{BC} = Q_{Con} + Q_{Rad} = 0 + Q_{Spec} = Q_{Spec} \quad (\text{Equation. D.2})$$

The specified heat flux at the boundary is equal to the radiative heat flux and therefore, by determining one the other is also set to that value. Therefore, using the specified heat flux boundary condition produces the same results as specifying the wall radiative heat flux.

Solar Radiation

For the case where the solar radiation must be simulated it can be shown that if the wall would be adiabatic without the solar radiation in the real situation then setting the wall heat flux to the desired solar radiation is mathematically identical. By rearranging the energy balance and setting Q_{BC} to zero equation D.3 shows that the Q_{Solar} is equal the wall convection heat flux and wall radiative heat flux.

$$Q_{BC} + Q_{Solar} = Q_{Rad} + Q_{Con} \Rightarrow 0 + Q_{Solar} = Q_{Solar} = Q_{Rad} + Q_{Con} \quad (\text{Equation D.3})$$

When this is compared to equation D.1 it is clear that the Q_{Solar} is equivalent to the Q_{BC} in that they are equal to the sum of the convection and radiation heat fluxes.

It should be noted that this assumes that the wall is a black body and therefore, all of the radiation is absorbed. If this is not the case then by changing the Q_{Solar} to what energy is expected to be absorbed and adding a diffuse radiation source equal to the radiation that would not be absorbed at the boundary would produce the desired results.

Appendix E: Solar Opening Analytical Model

Motivation:

This analytical solution was devised to provide temperature values to compare with the values provided by ANSYS CFX for the solar cube simulations in Chapter 4.

Known:

Table E.1 lists the variables that are considered known quantities for each simulation and are treated as constants in the following equations.

For Each Surface		General	
Symbol	Description	Symbol	Description
h	Coefficient of Heat Transfer	T_2	Temperature of Surface 2
q	Wall Heat Flux	θ_s	Solar Elevation Angle
T_{amb}	Ambient Temperature	a	See Figure E.1, $a = 1/\tan(\theta_s)$
A	Area of Surface		

Table E.1 Known Values

Unknowns:

Table E.2 lists the variables for which the solution solves.

Symbol	Description
T_{1A}	Temperature of Surface 1A
T_{1B}	Temperature of Surface 1B
T_3	Temperature of Surface 3

Table E.2 Unknown Variables

It should be noted that the view factors require calculation but are an aside that is dealt with in more detail in Table E.3

Assumptions:

- 1) Walls are black bodies
- 2) Surfaces are a uniform temperature
- 3) Steady state
- 4) No conduction along the walls, i.e. T_{1A} is not the same as T_{1B}
- 5) The cube is filled with a non conductive stationary material, i.e. the only heat transfer is by radiation

Domain:

The domain consists of a cube with the walls numbered as shown in Figure E.1.

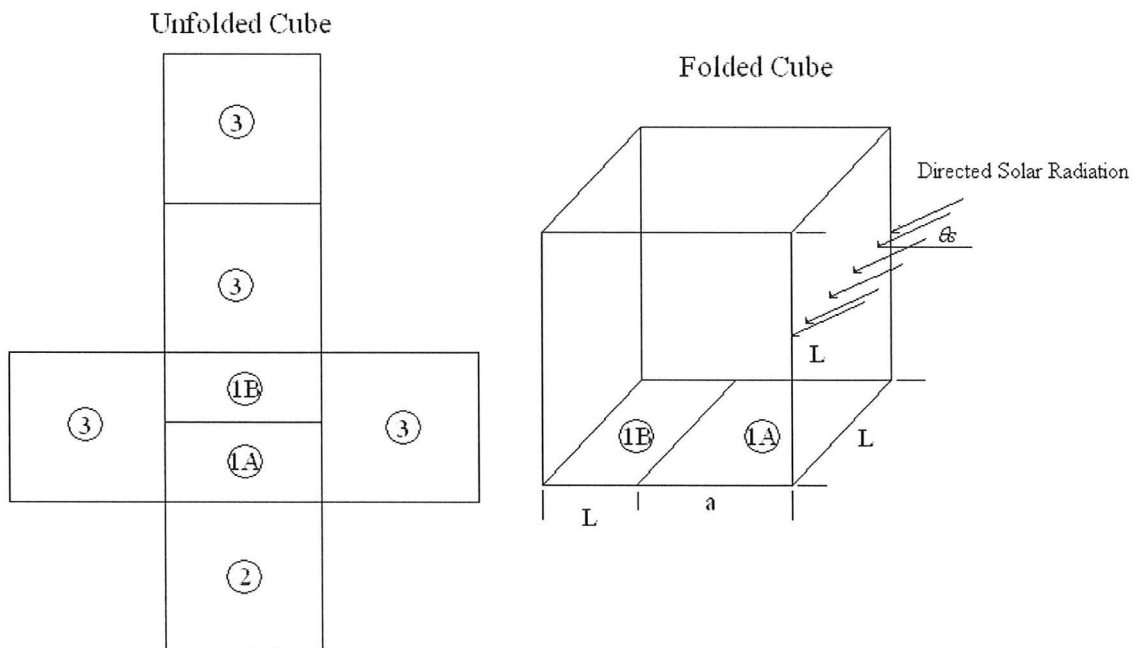


Figure E.1 Labeling Conventions for the Cube's Walls

Side 1 is the floor of the cube and divided into two surfaces: the A section that receives the solar radiation and the B section which is unlit. Side 2 is an opening, through which sunlight enters the cube, it is held at a constant temperature, representing the ambient conditions. The remaining sides are grouped together as surface 3 and are black bodies with a convective heat transfer co-efficient and an ambient temperature.

Equations:

The equation system is based on the conservation of energy equation for each surface. Figure E.2 shows the surface i and its related heat fluxes.

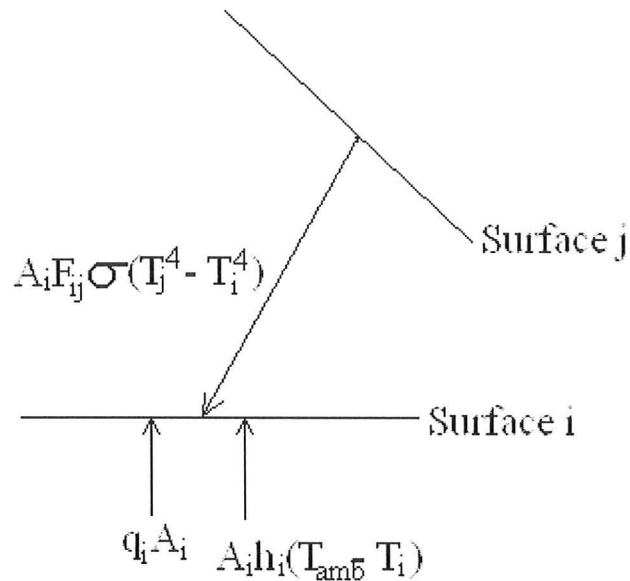


Figure E.2 Heat Fluxes for Surface i

Equation E.1 shows what the conservation of energy equation would be with these heat fluxes included.

$$\frac{\partial E}{\partial t} = \sum F_{ij} A_i \sigma (T_j^4 - T_i^4) + A_i h_i (T_{amb} - T_i) + q_i A_i \quad (\text{Equation E.1})$$

Since the simulation is steady state there should be no change with respect to time so the equation can be set to zero as in equation E.2.

$$0 = \sum F_{ij} A_i \sigma (T_j^4 - T_i^4) + A_i h_i (T_{amb} - T_i) + q_i A_i \quad (\text{Equation E.2})$$

This allows for the equation to be rearranged and the area to be removed from the equation as a common factor. This creates equation E.3 as shown below.

$$0 = -(\sigma T_i^3 \sum F_{ij} + h_i) T_i + \sigma \sum F_{ij} T_j^4 + (q_i + h_i T_{amb}) \quad (\text{Equation E.3})$$

Since the sum of all the view factors for a surface is equal to one, it can be replaced with that value [Incropera & DeWitt, 2002]. Then T_i with an exponent of one is isolated to create an equation for T_i , as in equation E.4.

$$T_i = \frac{\sum F_{ij} T_j^4 + (q_i + h_i T_{amb}) / \sigma}{T_i^3 + h_i / \sigma} \quad (\text{Equation E.4})$$

Equation E.4 solves for T_i , using T_i as a variable, and therefore iteration should be used to solve the equations with the previously calculated T_i used on the right hand side of the equation as in equation E.5.

$$T_i^{New} = \frac{\sum F_{ij} T_j^4 + (q_i + h_i T_{amb}) / \sigma}{(T_i^{Old})^3 + h_i / \sigma} \quad (\text{Equation E.5})$$

Since the only variables in the equation that are unknowns are the temperatures, the system of equations has three equations and three unknowns and is therefore solvable.

Determining View Factors:

In order to solve the iterative equations the view factors must be calculated. Table E.3 below lists the unknown view factors required for the solution.

Surface 1A	Surface 1B	Surface 2	Surface 3
F_{1A1A}	F_{1B1A}	F_{21A}	F_{31A}
F_{1A1B}	F_{1B1B}	F_{21B}	F_{31B}
F_{1A2}	F_{1B2}	F_{22}	F_{32}
F_{1A3}	F_{1B3}	F_{23}	F_{33}

Table E.3 Unknown View Factors

The value of the view factors change with each solar elevation angle and require the use of three properties of view factors, one equation and one energy balance to determine all of the view factors. The first property is the reciprocity relation expressed in equation E.6 [Incropera & DeWitt, 2002].

$$F_{ij} = F_{ji} \left(\frac{A_j}{A_i} \right) \quad \text{(Equation E.6)}$$

Therefore, if the areas of the surfaces are known then with a view factor from one surface to another the reverse view factor can be determined. The second property is the summation rule that was previously used in the creation of equation E.4 and is formally expressed by equation E.7 [Incropera & DeWitt, 2002].

$$1 = \sum_{j=1}^n F_{ij} \quad \text{(Equation E.7)}$$

The third property is that a plane or convex surface has a view factor of zero with respect to itself [Incropera & DeWitt, 2002]. This is also applies to surfaces 1A and 1B since they are part of the same plane. This allows the elimination of F_{1A1B} , F_{1B1A} , F_{1A1A} , F_{22} and F_{1B1B} as zero. The equation for the view factor between perpendicular rectangular surfaces, which have a shared edge, is known [Incropera & DeWitt, 2002]. Equation E.8 below is based on this equation and is used to calculate the view factor between surfaces 1A and 2.

$$F_{1A2} = \frac{1}{a\pi} \left(a \tan^{-1} \left(\frac{1}{a} \right) + \tan^{-1}(1) + (1+a^2)^{1/2} \tan^{-1} \left(\frac{1}{(1+a^2)^{1/2}} \right) + \frac{1}{4} \ln \left[\frac{2+2a^2}{2+a^2} \left(\frac{2a^2+a^4}{(1+a^2)^2} \right)^{a^2} \left(\frac{2+a^2}{1+a^2} \right) \right] \right) \quad \text{(Equation E.8)}$$

The final energy balance is based on the assumption that if surfaces 1A and 1B are the same temperature then, the radiation energy transfer between the surface 1 and 2 will be the same regardless of whether or not surface 1 is treated as one or two surfaces. Equation E.9 shows this energy balance.

$$F_{1A2}A_{1A}\sigma(T_2^4 - T_{1A}^4) + F_{1B2}A_{1B}\sigma(T_2^4 - T_{1B}^4) = F_{12}A_1\sigma(T_2^4 - T_1^4) \quad (\text{Equation E.9})$$

Sigma and the temperature difference can be eliminated as common factors since $T_1=T_{1A}=T_{1B}$. The equation can be then be rearranged, as in equation E.10, to solve for the view factor F_{1B2} as a function of F_{1A2} , F_{12} and the areas.

$$F_{1B2} = \frac{F_{12}A_1 - F_{1A2}A_{1A}}{A_{1B}} \quad (\text{Equation E.10})$$

The areas are known from the geometry and F_{1A2} can be calculated from equation E.8. F_{12} can be calculated from equation E.8 if a is replaced by 1. Finally because the view factor is purely geometric in nature it should be independent of the temperatures of the surfaces, as are the areas [Incropera & DeWitt, 2002]. Therefore, this equation for the view factor should hold if surfaces 1A and 1B are not the same temperature.

This information is sufficient to calculate all of the view factors, since the plane surfaces have a view factor of zero and equation E.8 and E.10 can be used to find all of the view factors for surfaces 1A and 1B except with respect to surface 3. However, using the summation rule, as outlined in equation E.7, on each surface allows for the determination of F_{1A3} and F_{1B3} .

$$\begin{aligned} F_{1A3} &= 1 - F_{1A2} \\ F_{1B3} &= 1 - F_{1B2} \end{aligned}$$

By Reciprocity

$$F_{31B} = F_{1B3} \frac{A_{1B}}{A_3}$$

$$F_{31A} = F_{1A3} \frac{A_{1A}}{A_3}$$

$$F_{21A} = F_{1A2} \frac{A_{1A}}{A_2}$$

$$F_{21B} = F_{1B2} \frac{A_{1B}}{A_2}$$

By Summation

$$F_{23} = 1 - F_{21B} - F_{21A}$$

By Reciprocity

$$F_{32} = F_{23} \frac{A_2}{A_3}$$

By Summation

$$F_{33} = 1 - F_{32} - F_{31A} - F_{31B}$$

Therefore all of the view factors can be determined.

Solution:

By removing the view factors that are zero and applying the boundary conditions the general equation E.5 can be applied to each surface with an unknown temperature to make a three equation system. For surface 1A there is no convective heat transfer to the ambient area, however, there is a wall heat flux modeling the sunlight. See Appendix D for the details of this boundary condition. Therefore, for surface 1A the equation is as shown in equation E.11.

$$T_{1A}^{New} = \frac{F_{1A2} T_2^4 + F_{1A3} T_3^4 + 1000/\sigma}{(T_{1A}^{Old})^3} \quad (\text{Equation E.11})$$

Surface 1B is adiabatic and has no wall heat flux or coefficient of heat transfer and is represented by equation E.12.

$$T_{1B}^{New} = \frac{F_{1B2}T_2^4 + F_{1B3}T_3^4}{(T_{1A}^{Old})^3} \quad (\text{Equation E.12})$$

Surface 2 is a known temperature and therefore does not need to be modeled in an equation. Surface 3 has a coefficient of heat transfer but no specified wall heat flux and is modeled by equation E.13.

$$T_3^{New} = \frac{F_{31A}T_{1A}^4 + F_{31B}T_{1B}^4 + F_{32}T_2^4 + h_3T_{amb}/\sigma}{(T_3^{Old})^3 + h_3/\sigma} \quad (\text{Equation E.13})$$

In the case where surface 3's boundary condition is a specified temperature equation E.13 is omitted from the solution and equations E.11 & E.12 are used with the variable T_3 treated as a constant.

Checking the Validity of Surface 3:

In creating the analytical solution four separate walls were treated as a single surface with a uniform temperature. Figure E.3 shows the average deviation from the average temperature as both an absolute value and a percentage of the total temperature difference in the solar cube.

Average Deviation from Average Temperature for Surface 3

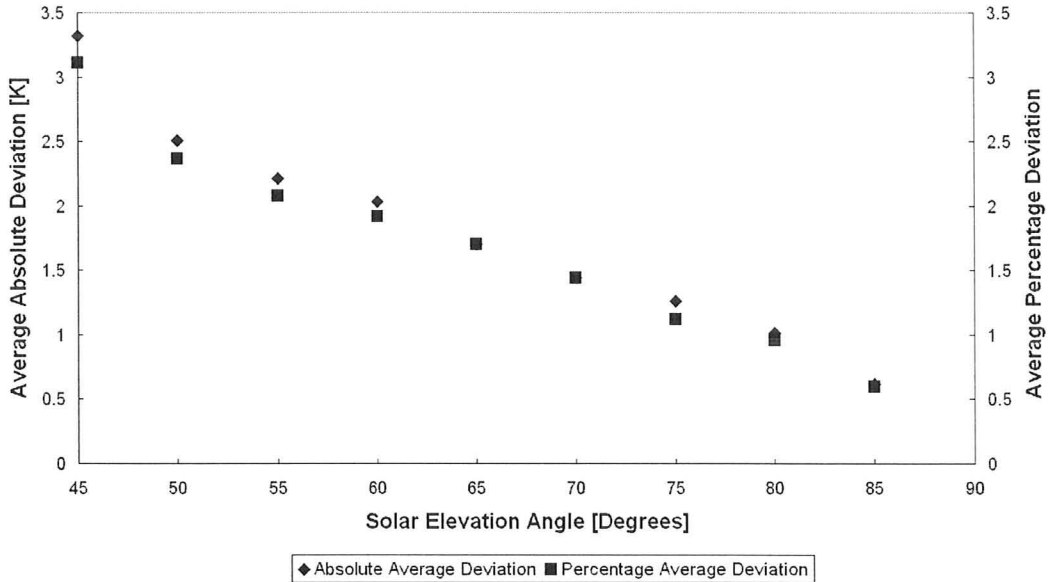


Figure E.3. Deviation as a Function of Angle

The deviation is defined for each node by equation E.14.

$$Deviation = |T - T_{AVG}| \quad (\text{Equation E.14})$$

There is a clear trend that the deviation decreases as the angle increases. Essentially the smaller the solar radiation input the smaller the deviation. The deviation percentage is larger than the error in the average temperature which remained unaffected by the value of the angle. This would suggest that surface 3 was not as uniform as assumed in the analytical solution; however, the average difference is still relatively small. This may account for some of the error in comparing the simulation to this solution.

Appendix F: Logical Functions Using CEL Code

Motivation:

ANSYS CFX 11 does not include logical functions, such as “if then” statements, that allow the user to set conditions for when or where an effect takes place. For example there is no explicit way for a user to limit a boundary source to an area. This very useful ability was required for the atrium simulation. The diffuse radiation through the blinds was limited to only the areas that had blinds and the temperature profile along the façade required a combination of three functions that occurred in three separate areas that did not correspond to the dimensions of the meshed areas. As such, the functions made available in CFX CEL code were used to create the required logical functions. This appendix explains the process and proves the validity of the method with truth tables and example simulations.

Basic Functions:

The Step Function

The step function serves as the primary logical unit in ANSYS CFX. It is defined as follows where x' must be a dimensionless variable. Figure F.1 shows the value of the step function over its domain.

$$\begin{aligned}x' < 0 &\rightarrow \text{step}(x') = 0.0 \\ \text{step}(x') &\Rightarrow \text{if } x' = 0 \rightarrow \text{step}(x') = 0.5 \\ x' > 0 &\rightarrow \text{step}(x') = 1.0\end{aligned}$$

(Equation F.1)[ANSYS CFX, CEL Functions, 2006]

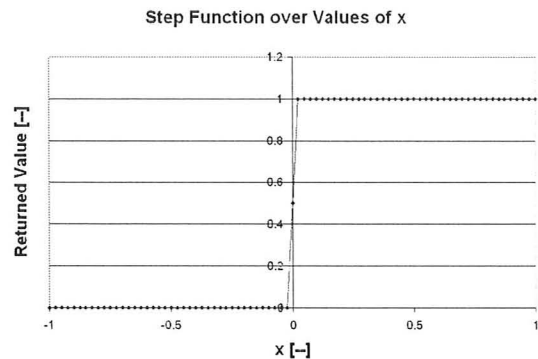


Figure F.1 Step Function

This function can be used as an on/off switch. The value at $x'=0$ could be problematic, however as it only occurs at a single point it should not effect the result significantly. In terms of making x' dimensionless, the simplest solution is to divide the value by a scale with the same units as x .

Minimum Value Function

The minimum value function returns the least value between two inputs.

$$\begin{aligned}x < y &\rightarrow \min(x, y) = x \\ \min(x, y) &\Rightarrow \text{if } x = y \rightarrow \min(x, y) = x \\ x > y &\rightarrow \min(x, y) = y\end{aligned}$$

(Equation F.2)

[ANSYS CFX, CEL Functions, 2006]

Maximum Value Function

The maximum value function returns the highest value between two inputs.

$$\begin{aligned} x < y &\rightarrow \max(x, y) = y \\ \max(x, y) &\Rightarrow \text{if } x = y \rightarrow \max(x, y) = y \\ x > y &\rightarrow \max(x, y) = x \end{aligned} \tag{Equation F.3}$$

[ANSYS CFX, CEL Functions, 2006]

Logical Statements:

Logical statements can be either true or false, for this thesis true results will be represented by 1 and false results will be represented by 0.

Greater Than Statement

If statement A is that ‘x is greater than a’, then A is logically equivalent to step(x-a). Table F.1 is a truth table that shows the logical equivalence of a greater than statement and the function step(x-a).

Location	A	x-a	step(x-a)
x<a	0	<0	0
x>a	1	>0	1

Table F.1. Greater Than Statement

Less Than Statement

If statement A is that ‘x is less than a’, then A is logically equivalent to step(a-x).

Table F.2 shows the logical equivalence

Location	A	a-x	step(a-x)
x<a	1	>0	1
x>a	0	<0	0

Table F.2. Less Than Statement

OR Statement

OR is the “or” statement which is true if either one or both of the arguments are true. This statement can be simulated using the maximum value function and Table F.3 shows their logical equivalence.

A	B	A OR B	max(A,B)
1	1	1	1
1	0	1	1
0	1	1	1
0	0	0	0

Table F.3. Logical OR Statement

AND Statement

AND is the “and” statement, which is only true if both arguments are true. This logical statement is logically equivalent to a minimum value statement, as shown in Table F.4.

A	B	A AND B	min(A,B)
1	1	1	1
1	0	0	0
0	1	0	0
0	0	0	0

Table F.4. Logical AND Statement

Alternative AND Statement

This type of “and” statement is simpler for a series of AND statements, such as (A AND B) AND (C AND D). It is a multiplication of the statements A and B. Table F.5 shows the logical equivalence.

A	B	A AND B	AxB
1	1	1	1
1	0	0	0
0	1	0	0
0	0	0	0

Table F.5. Alternative Logical AND Statement

XOR Statement

XOR is the “exclusive or” statement, which is true if only one of the arguments is true and false otherwise. To simulate this in CFX the difference of the maximum value and minimum value function for the same set must be used. It is important to note that C-D never becomes negative since the minimum of a set will always be equal to or less than the maximum of the same set. Table F.6 shows that truth table that proves the logical equivalence of the function and XOR.

A	B	A XOR B	C=max(A,B)	D=min(A,B)	(C-D)
1	1	0	1	1	0
1	0	1	1	0	1
0	1	1	1	0	1
0	0	0	0	0	0

Table F.6. Logical XOR Statement

Bounding Regions:

In order to define variables in a bounded area in CFX which does not match a surface it is easiest to bound the area with a logical statement that is only true in the desired area. The magnitude of the desired heat flux or other desired variable can be multiplied by the logical statement rendering it zero outside of the bounded area and the proper magnitude within the bounded area. There are two ways to bound areas, either by an AND statement or an XOR statement.

AND Bounded Regions

The first bounding method uses the AND logical statement to combine the constraint so that A is defined as $x > a$ and B is defined as $x < b$, where $b > a$ then the statement A AND B will only be true on the interval (a,b). Table F.7 shows the equivalency of the logical AND statement and x being bounded by a and b.

Location	A	B	A AND B
$x < a$	0	1	0
$a < x < b$	1	1	1
$x > b$	1	0	0

Table B.7. Bounding 1D with Logical AND Statement

It should be noted that if $a > b$ then the statement will always be false, as shown in the following Table F.8.

Location	A	B	A AND B
$x < b$	0	1	0
$b < x < a$	0	0	0
$x > a$	1	0	0

Table F.8. Logical AND Statement if $a > b$

Therefore, if the relative value of a and b change then new code must be used. When an area must be bound in multiple directions a combination of AND statements can be used. If the area must be bounded by $c < y < d$ and $a < x < b$, then the statement (A AND B) AND (C AND D) will only be true in the bounded area. This assumes that A and B are defined as previously and C is defined as $y > c$ and D is defined as $y < d$, where $d > c$. The following Table F.9 shows this.

X Location	Y Location	A	B	C	D	A AND B	C AND D	(A AND B) AND (C AND D)
$x < a$	$y < c$	0	1	0	1	0	0	0
$a < x < b$	$y < c$	1	1	0	1	1	0	0
$x > b$	$y < c$	1	0	0	1	0	0	0
$x < a$	$c < y < d$	0	1	1	1	0	1	0
$a < x < b$	$c < y < d$	1	1	1	1	1	1	1
$x > b$	$c < y < d$	1	0	1	1	0	1	0
$x < a$	$y > d$	0	1	1	0	0	0	0
$a < x < b$	$y > d$	1	1	1	0	1	0	0
$x > b$	$y > d$	1	0	1	0	0	0	0

Table F.9. Bounding 2D with Logical AND Statement

This is the case where the alternate definition of AND is useful since it would require the multiplication of four step functions rather than four step functions and three minimum value functions.

XOR Bounded Regions

The second method uses the XOR logical statement. By defining A as $x > a$ and B as $x > a + e = b$ where all values are positive it creates the effect that if B is true then A must also be true and it creates the following truth table shown in Table F.10.

Location	A	B	A XOR B
$x < a$	0	0	0
$a < x < b$	1	0	1
$x > b$	1	1	0

Table F.10. Bounding 1D with Logical XOR Statement

If the relative value of a and b switch such that $a > b$ the statement will still only return a value of one in the area bounded by the two values. As Table F.11 shows the statement is only true in the area bounded by (a,b).

Location	A	B	A XOR B
$x < b$	0	0	0
$b < x < a$	0	1	1
$x > a$	1	1	0

Table F.11. Bounding 1D with Logical XOR Statement when $a > b$

In order to bound a multiple dimensional region an AND logic statement can combine the two criteria, with statements A,B,C and D are defined in the previous section. Table F.12 shows that the combined logic statement is only true when $a < x < b$ and $c < y < d$.

X Location	Y Location	A	B	C	D	A XOR B	C XOR D	A XOR B AND C XOR D
$x < a$	$y < c$	0	0	0	0	0	0	0
$a < x < b$	$y < c$	1	0	0	0	1	0	0
$x > b$	$y < c$	1	1	0	0	0	0	0
$x < a$	$c < y < d$	0	0	1	0	0	1	0
$a < x < b$	$c < y < d$	1	0	1	0	1	1	1
$x > b$	$c < y < d$	1	1	1	0	0	1	0
$x < a$	$y > d$	0	0	1	1	0	0	0
$a < x < b$	$y > d$	1	0	1	1	1	0	0
$x > b$	$y > d$	1	1	1	1	0	0	0

Table F.12. Bounding 2D with Logical XOR Statements

It should be noted that XOR statements could be used to indicate the area outside of a bounded area. By making A mean that $x > a$ and B mean that $x < b$ then the XOR statement becomes false only in the bounded area. Table F.13 shows the truth table that demonstrates this.

Location	A	B	A XOR B
$x < a$	0	1	1
$a < x < b$	1	1	0
$x > b$	1	0	1

Table F.13. Outside of bounded area with Logical XOR Statement

This can also be expanded into two dimensions as with the inclusive bound, however, it requires that the AND statement be replaced with an OR statement. Table F.14 shows the truth table for this with A and B defined as in Table F.13, C defined as $y > c$ and D defined as $y < d$.

X Location	Y Location	A	B	C	D	A XOR B	C XOR D	A XOR B OR C XOR D
$x < a$	$y < c$	0	1	0	1	1	1	1
$a < x < b$	$y < c$	1	1	0	1	0	1	1
$x > b$	$y < c$	1	0	0	1	1	1	1
$x < a$	$c < y < d$	0	1	1	1	1	0	1
$a < x < b$	$c < y < d$	1	1	1	1	0	0	0
$x > b$	$c < y < d$	1	0	1	1	1	0	1
$x < a$	$y > d$	0	1	1	0	1	1	1
$a < x < b$	$y > d$	1	1	1	0	0	1	1
$x > b$	$y > d$	1	0	1	0	1	1	1

Table F.14. Outside of bounded area in 2D with Logical XOR Statements

In both cases the bounds can be functions rather than constants. Which method is superior depends on the situation. The AND method is simpler to code, especially when bounding in multiple directions, however, it requires additional statements if the relative values of the functions change, whereas the XOR bounding does not. The XOR statements are more adaptable, since they can be used indicate the region outside of the bounded area with a single change in sign within one step function.

Test Cases:

This test case will be a four meter square box with a bounded heat flux on the bottom. The remaining sides will have a heat transfer coefficient of $5 \text{ W/m}^2\text{K}$ and an external temperature of $280 \text{ }^\circ\text{K}$. Two different patterns will be used.

Pattern One: Trig Functions

This pattern is bounded by a cosine and sine function and the XOR method of bounding will be used. This should show that the code will work even if the functions change relative position. The equations are given by equations F.4 and F.5.

$$y_1 = \sin(2x) + 2 \quad (\text{Equation F.4})$$

$$y_2 = \cos(2x) + 2 \quad (\text{Equation F.5})$$

These equations translate into the boundaries:

$$\begin{aligned} \sin(2x) + 2 < y < \cos(2x) + 2 & \text{ if } \sin(2x) + 2 < \cos(2x) + 2, \text{ or} \\ \cos(2x) + 2 < y < \sin(2x) + 2 & \text{ if } \cos(2x) + 2 < \sin(2x) + 2, \end{aligned}$$

This will create the following pattern in Figure F.2.

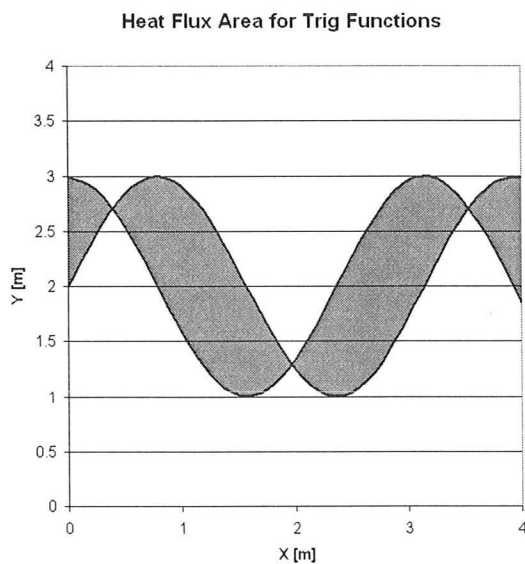


Figure F.2. Area Bounded by Trig Function

The code will take the form of:

$$\max(\text{step}(-\sin(2*x/1[\text{m}]) - 2 + y/1[\text{m}]), \text{step}(-\cos(2*x/1[\text{m}]) - 2 + y/1[\text{m}])) - \min(\text{step}(-\cos(2*x/1[\text{m}]) - 2 + y/1[\text{m}]), \text{step}(-\sin(2*x/1[\text{m}]) - 2 + y/1[\text{m}]))$$

(Equation F.6)

For the purposes of the simulation the logical statement was multiplied by a factor of ten. Figure F.3 shows the resultant heat flux of the code when run through a steady state, stationary simulation.

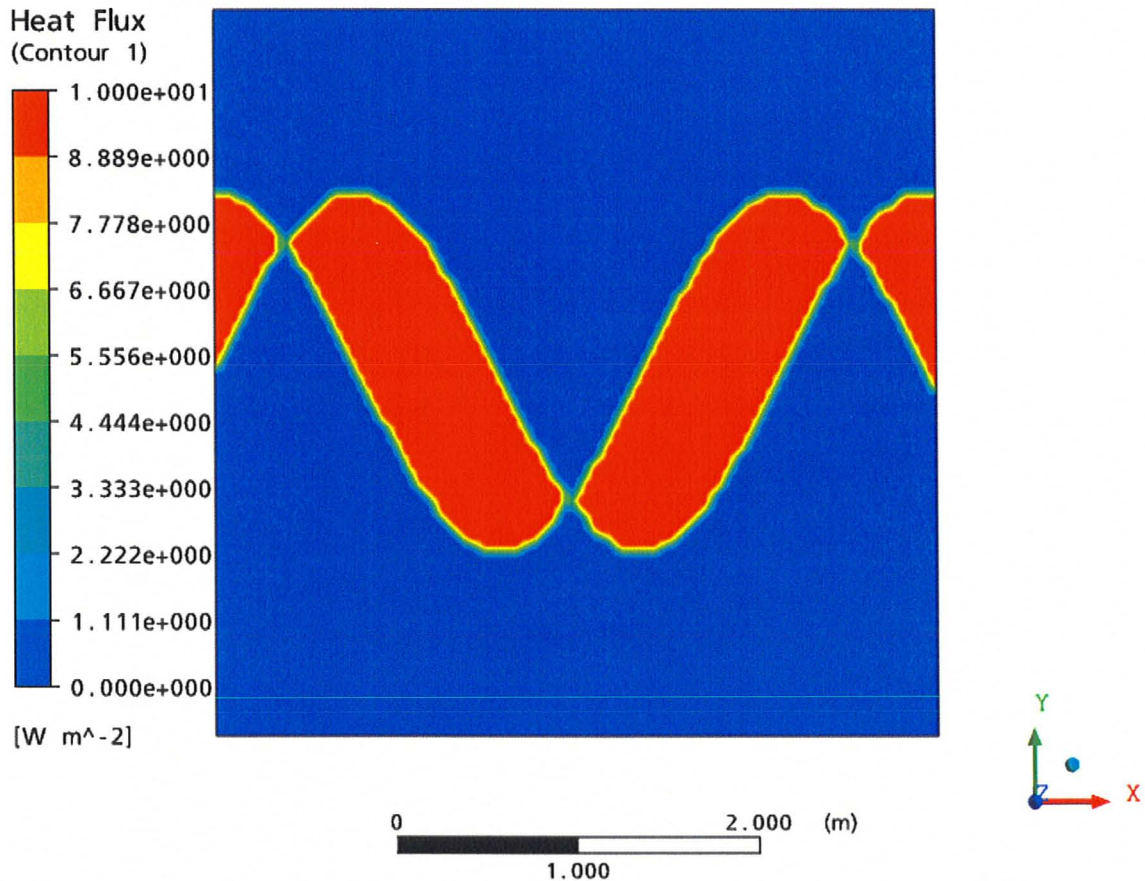


Figure F.3. Trigonometric Heat Flux in a Box.

The basic pattern was produced by the code. Figure F.3 clearly shows the areas bounded by the trig functions to have the proper heat flux and the areas outside of the bounded areas to have a heat flux of zero. However, there is a band of variable heat flux between the heated and adiabatic regions. In order to judge the range of this effect the heat flux along the centerline $y=2$ was plotted in comparison to the expected profile and is shown in Figure F.4.

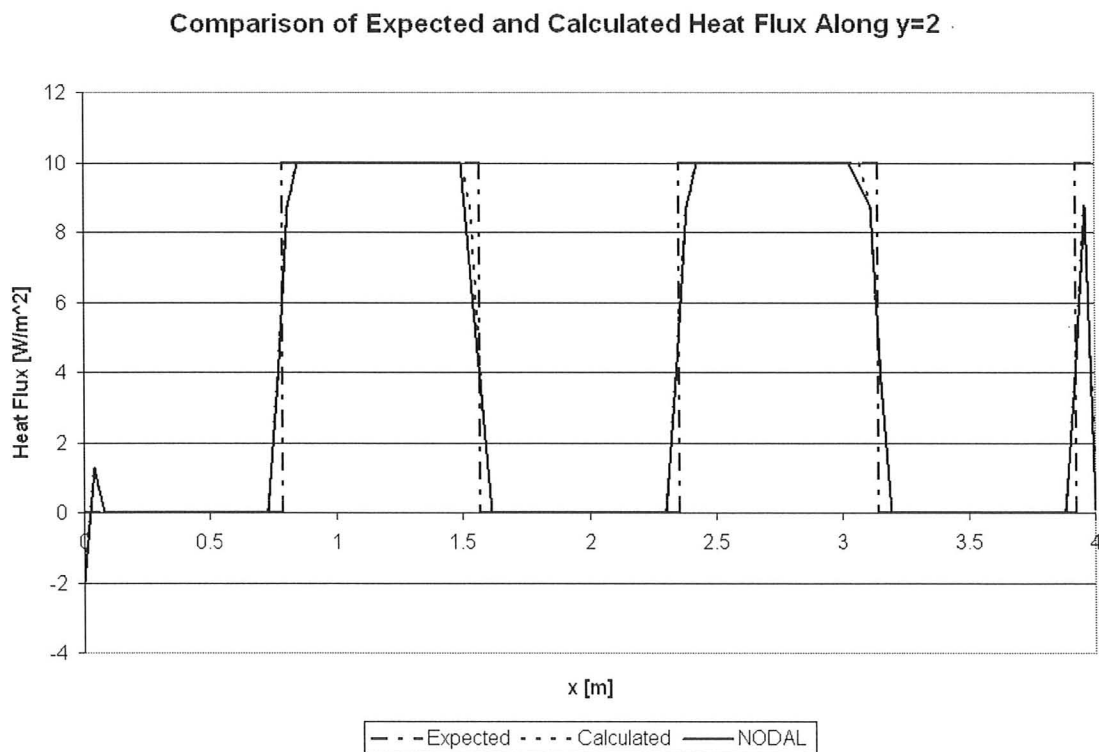


Figure F.4 Heat Flux along Line $y=2$

As Figure F.4 shows the actual heat flux is not as discontinuous as desired. This is partly due to the definition of the step function that produces a 0.5 exactly at the transition point. In addition, it appears that CFX attempts to adjust the heat flux to make

it more continuous. The area where this occurs is relatively small and it appears that net heat flow is preserved since it over and under estimates in approximately the same amount. However this may not be true for very small bounded areas.

Pattern Two: Lines

The heated area is bounded by the following lines and is depicted in the Figure F.5 below.

Line 1
 $y = x$ (Equation F.7)

Line 2
 $y = x + 1$ (Equation F.8)

Line 3
 $y = -x + 1$ (Equation F.9)

Line 4
 $y = -x + 2$ (Equation F.10)

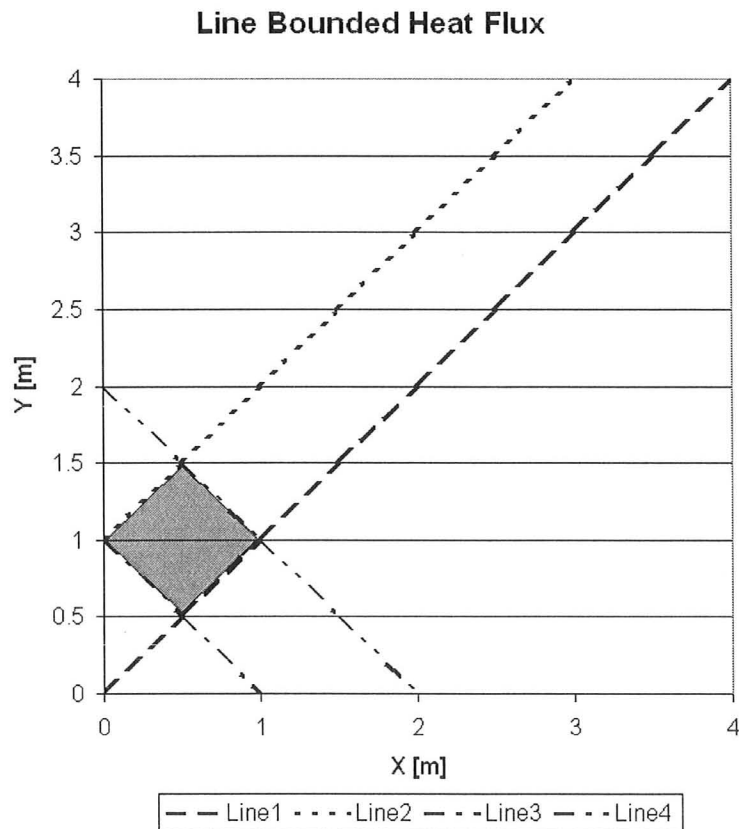


Figure F.5 Area Bounded by Four Lines

This requires two XOR Statements combined with an AND statement

XOR Statement #1

This statement describes the area between line 1 and line 2.

$$\max(\text{step}(y/1[m]-x/1[m]),\text{step}(y/1[m]-x/1[m]-1))-\min(\text{step}(y/1[m]-x/1[m]),\text{step}(y/1[m]-x/1[m]-1))$$

(Equation F.11)

XOR Statement #2

This statement describes the area between line 3 and line 4.

$$\max(\text{step}(y/1[m]+x/1[m]-2),\text{step}(y/1[m]+x/1[m]-1))-\min(\text{step}(y/1[m]+x/1[m]-2),\text{step}(y/1[m]+x/1[m]-1))$$

(Equation F.12)

Therefore the final statement is:

$$\min(\max(\text{step}(y/1[m]+x/1[m]-2),\text{step}(y/1[m]+x/1[m]-1))-\min(\text{step}(y/1[m]+x/1[m]-2),\text{step}(y/1[m]+x/1[m]-1)), \max(\text{step}(y/1[m]-x/1[m]),\text{step}(y/1[m]-x/1[m]-1))-\min(\text{step}(y/1[m]-x/1[m]),\text{step}(y/1[m]-x/1[m]-1)))$$

(Equation F.13)

The simulation resulted in the following heat flux pattern shown in Figure F.6.

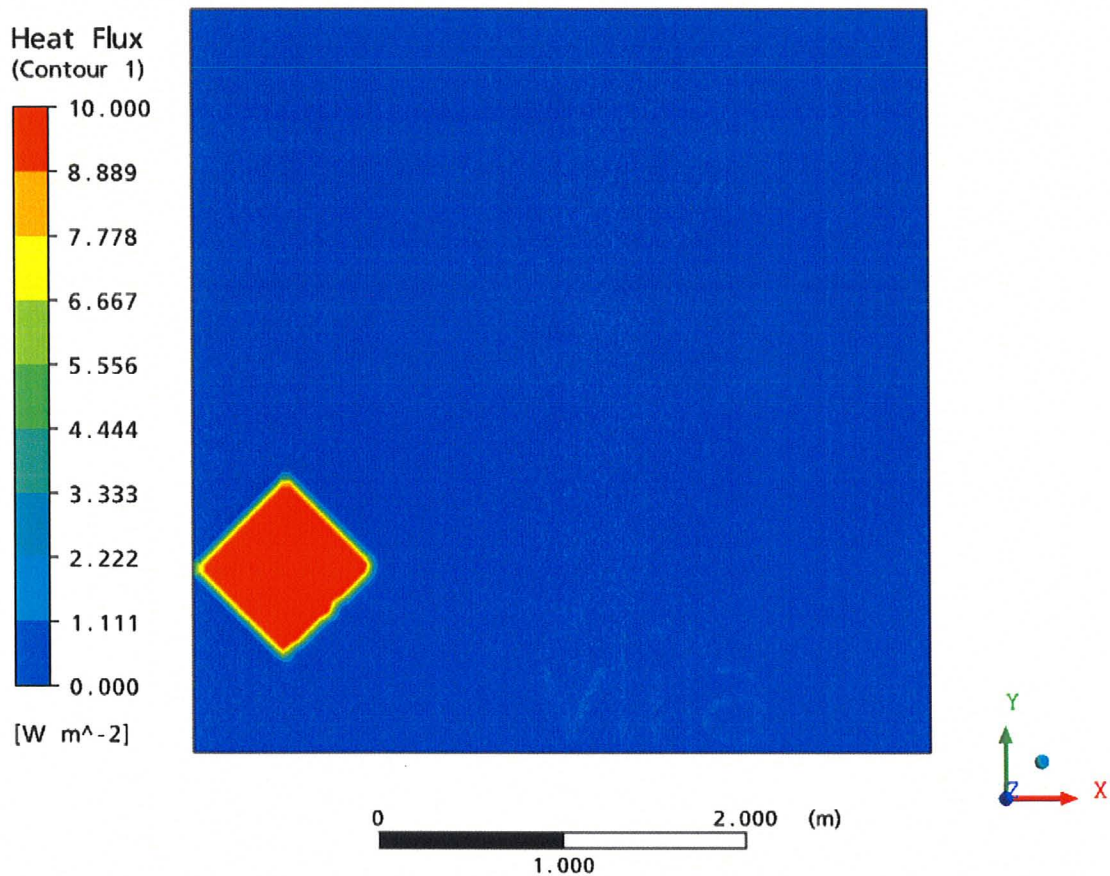


Figure F.6 Simulated Square Heat Flux Area.

Figure F.6 clearly shows the correct heat flux pattern, although the band of intermediate heat flux is still present. In order to gauge this band's effect, the total heat flux through the floor was compared to that of the expected results. The expected results show that the total heat flux should be 5 W whereas the simulation returned a value of 4.99 W. Therefore the intermediate heat flux values only create an error of 0.2% in the net heat flow through the floor. Further analysis was performed on the heat flux along the line $y=0.75$. This is shown in Figure F.7.

Comparison of Expected and Calculated Heat Flux Along $y=0.75$

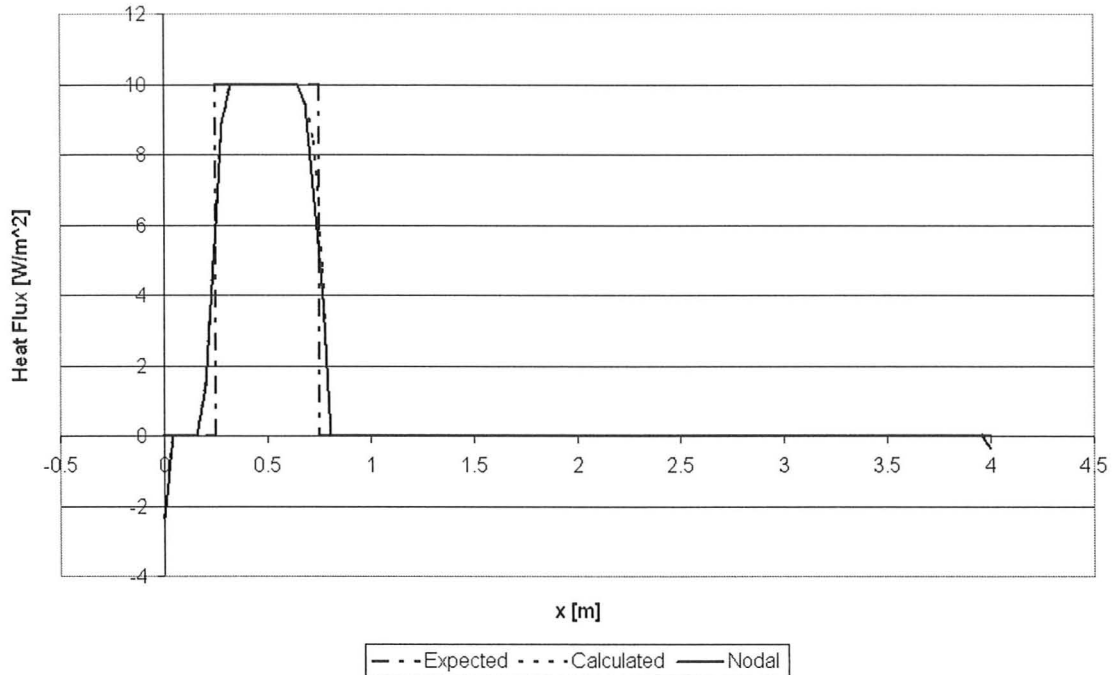


Figure F.7. Heat Flux Along $y=0.75$

Figure F.7 shows the same pattern of intermediate values as in Figure F.4. The range of error is proportionally larger because of the smaller area of heat flux. This may also be from the different angle that the line along which the heat flux was measured is intersecting with the pattern.

It should be noted that this simulation was done with radiation to insure that it did not affect the heat flux through the floor.

Appendix G: Solar Position Angles

Motivation:

It is necessary to be able to describe the position of the sun in order to determine the angle at which solar radiation will enter the atrium. Since the angle of the solar radiation determines both the amount of radiation and the location of its effect, it is essential for an accurate simulation. The zenith and solar elevation angle, which are the relative location of the sun and the direction of the solar radiation respectively, must be calculated. The angle depends on the time of day, day of the year and the location of the atrium on the earth's surface. These factors are expressed in the hour angle, codeclination and colatitude, of which the zenith angle is a function. As such, this appendix reviews the relevant factors and demonstrates the calculations used to determine the angle used in the atrium simulations.

Angle Definitions and Equations:

Codeclination (D')

The codeclination is the angle from the north pole to the direction vector that points towards the sun. It varies between 66.5 degrees at the summer solstice and 113.5 degrees at the winter solstice [Wieder, 1982]. Figure G.1 shows the co-declination for the earth. It can be calculated using equation G.1 [Wieder, 1982]:

$$\cos D' = \sin 23.5^\circ \sin \frac{360^\circ n}{365.25 \text{ days}} \quad (\text{Equation G.1})$$

where n is the number of days since the vernal equinox.

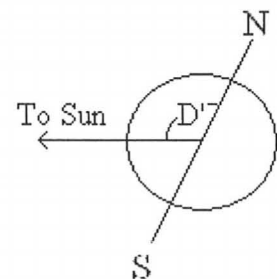


Figure G.1 Earth's Codeclination

Colatitude (L')

The colatitude is the compliment of the latitude. Rather than being measured from the equator the angle is measured from the closest pole. Figure G.2 shows the colatitude to a location on the earth's surface

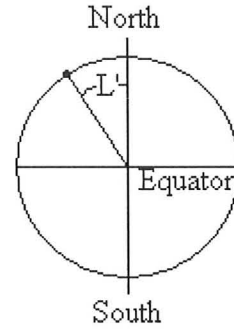


Figure G.2. Colatitude Angle

Local Time Until Solar Noon (t)

Represents the time since or until the local solar noon, for which t is zero. This time is determined by the location's relative longitude from the standard meridian of the time zone, and the EOT, which is available in table form for most days of every month [Wieder, 1982]. The exact relationship is shown in equation G.2.

$$t = Time_{Local} - 12 : 00 + 4(Long_{St} - Long_{Loc}) + EOT \quad \text{(Equation G.2)}$$

This equation provides a time in minutes but it must be converted to hours to be used in the rest of the calculations.

Hour Angle (H)

The hour angle is a measurement of how far the sun is from the local solar noon. Equation G.3 [Wieder, 1982] shows the relationship between the local time and the hour angle.

$$H = \pm \frac{360^\circ}{24hr} t \quad \text{(Equation G.3)}$$

Zenith Angle (Z)

The zenith angle is the angle between the sun and the normal of the earth's surface, if it were a smooth sphere. Figure G.3 shows the zenith angle for a location on the earth's surface. It should be noted that as the earth rotates on its axis the zenith angle will change. Equation G.4 [Wieder, 1982] shows this relationship.

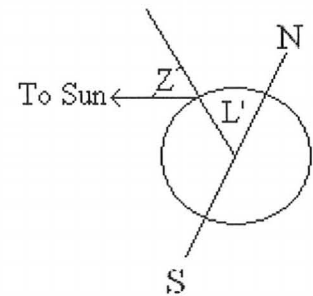


Figure G.3 Zenith Angle

$$\cos Z = \cos D \cos L + \sin D \sin L \cos H$$

(Equation G.4)

Solar Elevation (θ_s)

The solar elevation angle is angle between the horizon and the sun and is the compliment of the zenith angle.

$$\theta_s = 90^\circ - Z$$

(Equation G.5)

Simulation Calculations:

The atrium is in Montreal, which is located at 74W and 45N [City of Montreal, 2008] and the data used was collected at noon on October 26, 2007. This is sufficient information to determine the solar elevation angle. By substituting the information into the above equations, the angle of the sun can be calculated, as follows.

$$L' = 45^\circ$$

$$n = 217 \text{ [Wieder, 1982]}$$

$$t = (12:00 - 12:00 + 4(75 - 74) + 16) = 20 \text{ min} = 0.33 \text{ hr}$$

$$H = \frac{360^\circ}{24 \text{ hr}} (0.33 \text{ hr}) = 4.95^\circ$$

$$D' = \arccos \left(\sin 23.5^\circ \sin \frac{360^\circ (216 \text{ days})}{365.25 \text{ days}} \right) = 102.94^\circ$$

Substituting into the equation for the zenith angle

$$\cos Z = \cos(102.9^\circ) \cos(45^\circ) + \sin(102.9^\circ) \sin(45^\circ) \cos(4.95^\circ) = 0.529 \Rightarrow Z = 58.1^\circ$$

Therefore the solar elevation angle for the simulations should be 31.9 degrees.

[Wieder, 1982]

Appendix H: Opening Back Entrance (OBE)

Motivation:

An opening boundary condition was initially considered for the boundary at the north end of the atrium. In the experimental atrium the north end of the atrium connects to rest of the building and allows airflow between the two areas. Only an inlet with a specified velocity profile or an opening can model this re-circulating flow. There was insufficient data to construct a velocity profile so an opening was the most obvious choice for the north end boundary condition. Chapter 6 used an adiabatic wall instead of an opening. An opening boundary condition proved unusable. The result of simulations, which used an opening boundary condition, is presented here to illustrate the reason for the use of an adiabatic wall boundary condition.

Modification:

The simulation was run with the boundary at the north end of the atrium modelled as an opening rather than an adiabatic wall. The temperature of the opening was initially set to 30°C and then to a linear temperature profile to demonstrate the reason for the initial results.

Results:

Table H.1 shows temperature predictions for the simulation with the opening boundary condition at the north end of the atrium.

	Experimental Data			Opening Back Entrance		
	East Sting	Center String	West String	East Sting	Center String	West String
T ₁₆	24.7	24.5	24.4	29.9	30.0	30.0
T ₁₅	23.1	23.1	23.6	30.0	30.0	30.0
T ₁₄	22.8	22.9	23.0	30.0	30.0	30.0
ΔT	1.90	1.60	1.40	-0.10	0.00	0.00

Table H.1 Temperatures for Experimental Data and Opening Back Entrance Simulation

Discussion:

The opening boundary condition creates a uniform temperature within the atrium. The reason for this is clear from a velocity vector plot along the centre of the atrium, as in Figure H.1 below.

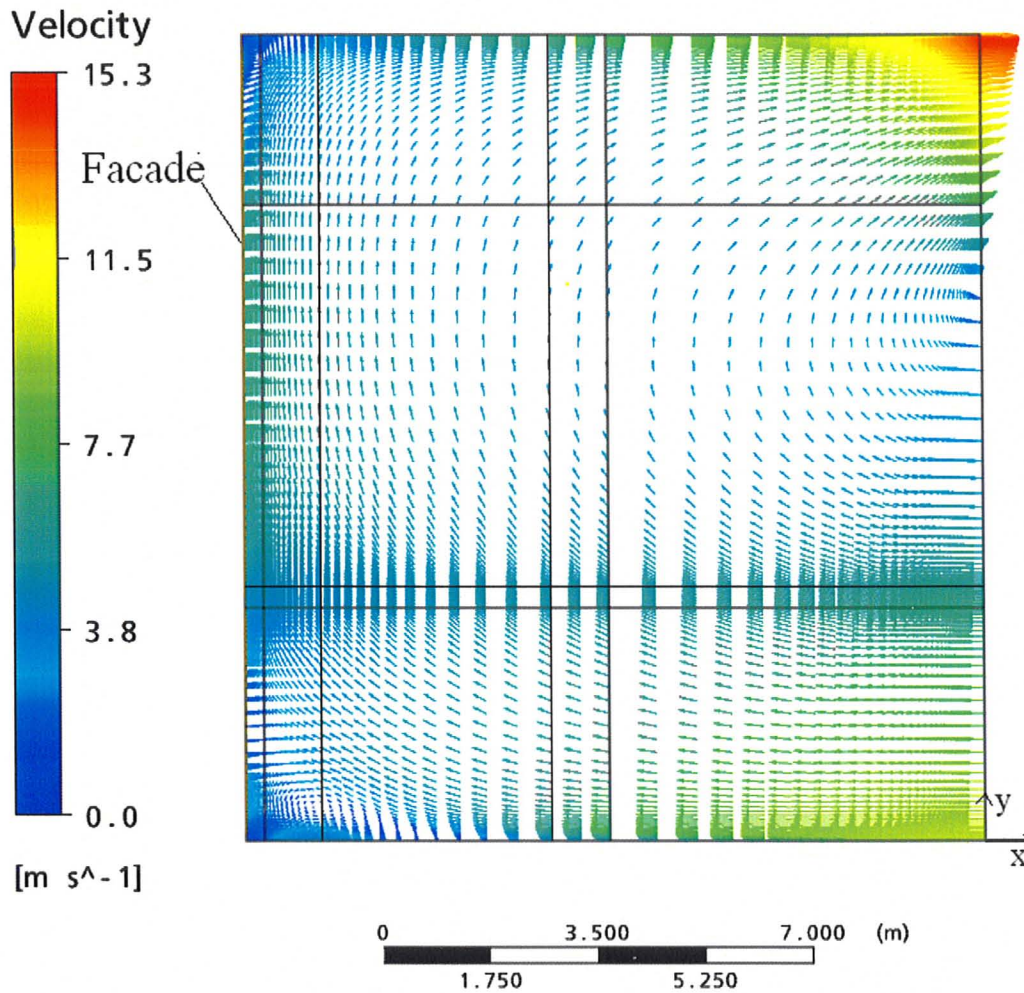


Figure H.1 Velocity in Atrium with an Opening on the North End

The velocity magnitudes are clearly too high to be realistic and dominate the flow. This is further seen with the simulation where the temperature along the opening was given a linear profile. Figure H.2 shows the temperature in the atrium when this occurs.

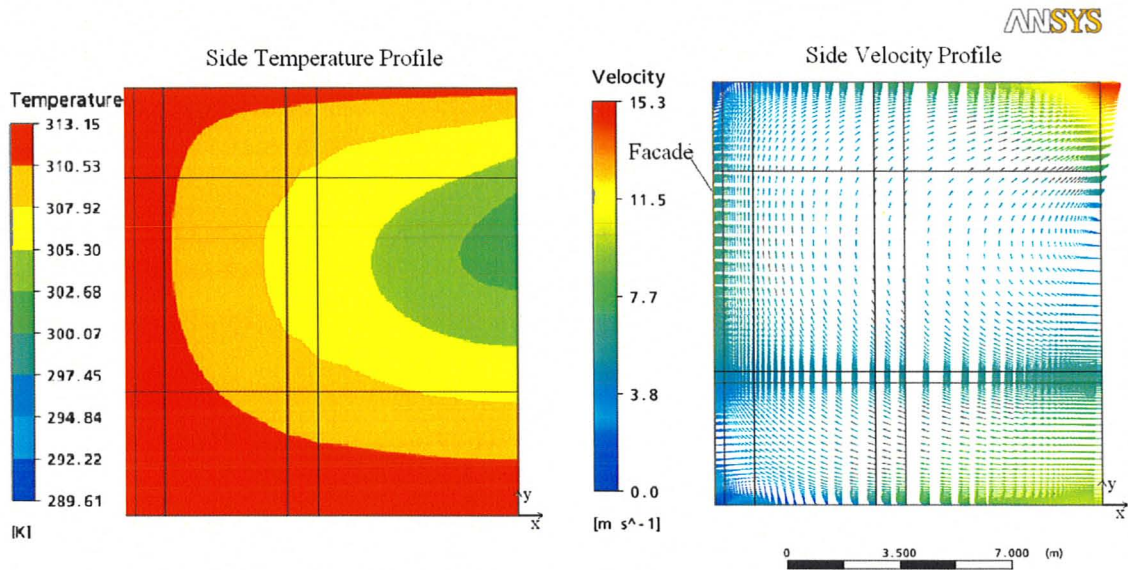


Figure H.2 Temperature and Velocity Field for Atrium with Opening.

The temperature is entirely dependent on the temperature of the air that enters from the opening boundary condition. Essentially advection over powers the other sources of heat transfer. Therefore, the opening boundary condition is unusable. If the velocity boundary condition was used with the opening then it may work. At this point, there is insufficient data to construct such a boundary condition.